

TECHNISCHE UNIVERSITÄT MÜNCHEN

DISSERTATION

**Small Animal X-ray
Phase-Contrast Imaging**

Arne Tapfer

Fakultät für Physik
Technische Universität München

Supervisors:
Dr. Martin Bech
Prof. Dr. Franz Pfeiffer

July 2013



Lehrstuhl für
Biomedizinische Physik



Technische Universität München

TECHNISCHE UNIVERSITÄT MÜNCHEN
Physik Department
Lehrstuhl für Biomedizinische Physik

Small Animal X-ray Phase-Contrast Imaging

Arne Tapfer

Vollständiger Abdruck der von der Fakultät für Physik der Technischen Universität München zur Erlangung des akademischen Grades eines

Doktors der Naturwissenschaften (Dr. rer. nat.)

genehmigten Dissertation.

Vorsitzender: Univ.-Prof. Dr. M. Zacharias

Prüfer der Dissertation: 1. Univ.-Prof. Dr. F. Pfeiffer

2. Univ.-Prof. Dr. A. Haase

Die Dissertation wurde am 22.05.2013 bei der Technischen Universität München eingereicht und durch die Fakultät für Physik am 16.07.2013 angenommen.

Abstract

In the field of biomedical X-ray imaging, grating-based phase contrast is a novel imaging technique that has the potential to improve medical diagnosis due to increased soft-tissue contrast. In this context, the present work investigates two different aspects in the translation of the technique from bench to bedside. On the one hand, potential applications that might benefit from X-ray phase-contrast imaging are investigated on the basis of mouse disease models. On the other hand, the development of a first small-animal phase-contrast CT scanner is pursued.

With regard to potential imaging applications and disease models, three different mouse models of cancer are investigated in detail. The imaging data for all specimen is analyzed with respect to the visibility of cancer lesions, both visually and quantitatively (using signal-to-noise and contrast-to-noise ratios). The main scientific results of this work have been published in Tapfer et al., X-ray Phase-Contrast CT of a Pancreatic Ductal Adenocarcinoma Mouse Model, PLoS One (2013).

In terms of small-animal CT scanner development, the process from design considerations via commissioning experiments with a first prototype to the final rotating-gantry CT scanner is covered. In particular, rotation stability, the correction of related image artifacts, and CT reconstruction accuracy are analyzed in depth. The potential for preclinical imaging is assessed with CT scans of fixated biological tissue. The main scientific results of this part have been published in Tapfer et al., Development of a prototype gantry system for preclinical X-ray phase-contrast computed tomography, Med. Phys. (2011), and Tapfer et al., Experimental results from a preclinical X-ray phase-contrast CT scanner, PNAS (2012).

As a result of the present work, phase-contrast CT is identified as a promising method for the study of mouse disease models, and the scanner development process yields a fully-functioning CT scanner that is available for future pre-clinical research.

Zusammenfassung

Die gitterbasierte Röntgen-Phasenkontrast-Bildgebung stellt eine neuartige Modalität im Bereich der biomedizinischen Bildgebung dar, die aufgrund des erhöhten Weichteilkontrasts das Potenzial hat, die medizinische Diagnostik zu verbessern. Vor diesem Hintergrund befaßt sich die vorliegende Arbeit mit zwei Aspekten der Überführung dieser Technologie aus dem Labor in den klinischen Betrieb. Auf der einen Seite werden klinische Fragestellungen, welche von der neuartigen Bildgebung profitieren könnten, im Mausmodell untersucht. Auf der anderen Seite wird die Entwicklung eines ersten Kleintier-Röntgen-Phasenkontrast CT Scanners vorangetrieben.

Im Hinblick auf mögliche klinische Anwendungen werden drei verschiedene Maus-Tumormodelle ausführlich betrachtet. Die aufgenommenen Bilddaten werden hinsichtlich der Sichtbarkeit von krebsartigen Gewebsveränderungen analysiert - sowohl visuell als auch quantitativ mit Hilfe von Signal-Rausch-Verhältnissen. Die wissenschaftlichen Erkenntnisse dieser Untersuchungen wurden in der folgenden Studie veröffentlicht: Tapfer et al., X-ray Phase-Contrast CT of a Pancreatic Ductal Adenocarcinoma Mouse Model, PLoS One (2013).

Bei der Entwicklung des Kleintier-CT Scanners wird der komplette Entwicklungsprozess beschrieben: vom theoretischen Konzept, über erste Testläufe mit einem Prototypen, bis hin zum funktionsfähigen CT Scanner mit drehbarer Gantry. Insbesondere werden die Stabilität beim Drehen der Gantry, die Korrektur damit verbundener Bildartefakte und die quantitative Genauigkeit von CT Rekonstruktionen näher untersucht. Das Potenzial für die präklinische Bildgebung wird anhand von CT Aufnahmen von fixiertem biologischem Gewebe beurteilt. Die zentralen wissenschaftlichen Ergebnisse dieses Entwicklungsprozesses wurden in den beiden folgenden Studien veröffentlicht: Tapfer et al., Development of a prototype gantry system for preclinical X-ray phase-contrast computed tomography, Med. Phys. (2011) und Tapfer et al., Experimental results from a preclinical X-ray phase-contrast CT scanner, PNAS (2012).

Die beiden Kernergebnisse der vorliegenden Arbeit sind folgende: Die Röntgen-Phasenkontrast-Bildgebung wird als vielversprechende Methode zur Untersuchung von Mausmodellen identifiziert, und der CT Scanner Entwicklungsprozess bringt ein voll funktionsfähiges Gerät hervor, welches für zukünftige präklinische Untersuchungen zur Verfügung steht.

Contents

1	Introduction	1
1.1	Motivation	1
1.2	Outline	3
1.3	General remarks	4
2	Theoretical background	5
2.1	X-rays and their interaction with matter	5
2.1.1	Refractive index	6
2.1.2	Coherence	9
2.1.3	Free-space propagation	11
2.2	X-ray sources	13
2.2.1	X-ray tube	13
2.2.2	Synchrotron radiation	14
2.3	Grating-based phase-contrast imaging	15
2.3.1	Introduction	15
2.3.2	Talbot effect	16
2.3.3	Grating interferometer	18
2.3.4	Use of incoherent radiation	24
2.3.5	Geometrical magnification: fan-beam geometry	27
2.4	Computed tomography	28
2.4.1	General principle	28
2.4.2	Reconstruction of trimodal tomographic slices	31
2.5	Effective energy of polychromatic X-ray spectrum	33
2.6	Production of gratings	35
3	Imaging of mouse models of cancer	39
3.1	Motivation	39
3.2	Outline	41
3.3	Description of X-ray phase-contrast imaging setups	42
3.3.1	Synchrotron radiation source	43
3.3.2	Tube source	45

3.4	Imaging of a healthy mouse	45
3.4.1	Introduction	45
3.4.2	Description of cryo-imaging setup	47
3.4.3	Imaging parameters and data analysis	47
3.4.4	Imaging results	49
3.4.5	Discussion	51
3.5	Imaging of a mouse model of pancreatic cancer	53
3.5.1	Introduction	53
3.5.2	Tumor model and imaging parameters	54
3.5.3	Measurement of X-ray dose	55
3.5.4	Imaging results	57
3.5.5	Discussion	65
3.5.6	Summary	65
3.6	Imaging of a colon carcinoma-bearing mouse	67
3.6.1	Introduction	67
3.6.2	Tumor model and imaging parameters	67
3.6.3	Imaging results	68
3.6.4	Summary	72
3.7	Imaging of mouse models of cancer: Summary	72
4	Development of a small-animal phase-contrast CT scanner	73
4.1	Motivation	73
4.2	Outline	74
4.3	Technical development	74
4.3.1	General design considerations	74
4.3.2	Stationary-gantry prototype	78
4.3.3	Rotating-gantry CT scanner	80
4.4	Results from the stationary-gantry prototype	82
4.4.1	Quantitative phantom study	83
4.4.2	Color coding of image contrasts	87
4.4.3	Summary	89
4.5	Results from the rotating-gantry CT scanner	90
4.5.1	Stability	90
4.5.2	Adaptive differential phase recovery	91
4.5.3	Quantitative CT imaging results	95
4.5.4	CT scan of excised mouse liver	99
4.5.5	Summary	101
4.6	Further development and technical issues	101
4.6.1	Improvement of rotational stability	102
4.6.2	Adjustment of interferometer design energy	103
4.6.3	Reduction of silicon wafer thickness	104

4.6.4	Data acquisition and CT reconstruction	105
4.6.5	Deterioration of source grating	105
4.7	Summary and Outlook	106
5	Summary, conclusions and outlook	109
	Bibliography	120
	Publications and scientific presentations	121
	Acknowledgments	125

Chapter 1

Introduction

In this chapter, the topic of the present PhD thesis is introduced and the specific research focus is described. Moreover, an outline of the structure of the thesis is given. Finally, some general remarks concerning the framework of the PhD work are made.

1.1 Motivation

Ever since the discovery of X-rays by W. C. Röntgen more than 100 years ago (1895), their ability to penetrate matter has been explored for imaging of objects, which are opaque for visible light. Nowadays, the most important applications are medical diagnostics, non-destructive testing, and scientific research. Conventional X-ray imaging is based on illuminating the object of interest from one side and recording the transmitted intensity on the other side with an imaging detector. Image formation, in other words, the generation of contrast, is based on differences in density and elemental composition of the irradiated material. In general, good contrast is available for objects that exhibit high density differences as these translate into pronounced changes of transmitted intensity. In medical imaging, bones for example, can be very clearly distinguished from their surrounding tissue. In the case of different types of soft tissue (such as cartilage, muscles, and tumors), which exhibit a very similar extent of X-ray absorption, only limited contrast is available. With respect to medical diagnosis, this implies that the perceptibility of pathological changes within soft tissue is poor. This is, for example, the case for certain types of breast cancer.

Over the past years, several phase-sensitive X-ray imaging techniques have been developed. For the formation of contrast, these rely on the phase shift that X-rays undergo when passing through the object. Due to the fact that

for soft tissues, the difference in phase shift is more pronounced than the difference in attenuation, image contrast can be greatly enhanced. As all imaging detectors can only record X-ray intensity, the undergone shift in phase has to be transferred into a change of intensity. There are different mechanisms for achieving this conversion and the corresponding imaging methods differ in this respect. In general, there are free-space propagation-based techniques, crystal analyzer-based techniques, and interferometer-based techniques. The technique under investigation in this PhD thesis, grating-based phase-contrast, is an interferometric technique that uses diffraction gratings to measure the derivative of the phase. Mostly due to its outstanding compatibility with conventional X-ray tube sources, grating-based phase-contrast imaging has emerged as a very promising candidate for medical imaging.

In order to position and delimit grating-based phase contrast in the context of other anatomical medical imaging technologies, these are discussed briefly. Among those, X-ray computed tomography (CT) is the most prevalent technique. It features very high spatial resolution (submillimeter), and image acquisition is very fast (on the order of seconds). Disadvantages are low soft-tissue contrast and the involvement of radiation dose. Magnetic resonance imaging (MRI) benefits from very high soft-tissue contrast and the absence of radiation dose. Spatial resolution, however, is fundamentally limited and typically inferior to X-ray CT. Moreover, acquisition time is longer (on the order of minutes) and MR technology is distinctly more expensive. In this context, X-ray phase-contrast imaging combines high spatial resolution with high soft-tissue contrast at the same time, rendering it a promising tool for medical diagnosis.

Towards medical application of grating-based phase-contrast imaging, huge research efforts were made in the last years and are increasingly being continued. In the early 2000s, mostly benchmarking experiments were performed at large-scale synchrotron facilities using highly-brilliant radiation. Recently, experiments are more oriented towards clinical applications, using conventional X-ray tube sources and bench-top imaging setups. Increased soft-tissue contrast has been demonstrated numerously in both configurations, mostly for excised fixated tissue. However, up until now, all tomographic imaging experiments were based on a rotation of the sample, which is obviously not applicable for routine medical imaging.

A key effort of the present work hence is to develop a first phase-contrast CT scanner with a rotating gantry and stationary object accordingly. As modern human CT scanners are highly complex and highly optimized devices, the development of a small-sized scanner for imaging of rats and mice was pursued. Since the operating principle is identical, the gained experience may be very helpful for developing an upscaled version for human size.

The other part of the present work aims at identifying potential applications for biomedical phase-contrast imaging. Technologically, at the present state, the field-of-view is limited to approximately 10 cm in diameter, which is why CT imaging of larger samples is tedious. This is why in many research studies small pieces of excised tissue are used for imaging. In contrast, the focus of the present work is on whole-body ex-vivo studies of mouse models of disease. The emphasis in this context is on tumor detection and characterization for the case of spontaneous tumor models.

Both parts, the development of a first preclinical CT scanner and the investigation of disease models, together, serve two main purposes: firstly, to make a novel imaging tool available to small-animal biomedical research and, more importantly, to help translating grating-based phase-contrast imaging from bench to bedside, which is the ultimate goal.

1.2 Outline

This thesis is structured as follows. After this introduction, **Chapter 2** outlines the theoretical background. It covers basic properties of X-rays and reviews their interaction with matter. Furthermore, the generation of X-rays and the operating principle of grating-based phase-contrast imaging are elaborated on. Afterwards, the determination of the effective energy of a polychromatic X-ray spectrum and the production of X-ray optical components (gratings), which are required for the imaging technique, are introduced. **Chapter 3** is the first of the two results chapters and is concerned with the application of X-ray phase-contrast CT to ex-vivo imaging of mouse disease models. The imaging results of several specimens are shown, covering one healthy, one colon carcinoma and one pancreas tumor model mouse. Moreover, for comparison, the imaging results of magnetic resonance imaging and cryotome-based optical imaging (cryo-imaging) are shown for two of the mice. **Chapter 4** is devoted to the development of a first phase-contrast CT scanner and represents the main scientific contribution of this PhD work. The entire development process is presented—it covers the technical design, the development of a first prototype and finally the development of a rotating-gantry CT scanner. Moreover, commissioning experiments, an elaborate study assessing stability and imaging results of biological tissue are presented. At the end, further technical developments of the CT scanner are shown. In **Chapter 5**, the main scientific results are summarized and future perspectives conclude the thesis.

1.3 General remarks

Framework for the development of the micro-CT scanner: The engineering and assembly of a micro-CT scanner is a very expensive, complex and elaborate task. For this reason, the head of the *Chair of Biomedical Physics of Technische Universität München*, Prof. Dr. Franz Pfeiffer, applied for a *Starting Grant* with the *European Research Council*, which was granted in 2009 (ERC, FP7, StG 240142). Moreover, a very close collaboration with an industrial partner that has a long-standing experience in engineering state-of-the-art micro-CT scanners was initiated: Bruker microCT (Kontich, Belgium, formerly known as Skyscan). This collaboration joins the phase-contrast imaging expertise with the technical know-how of engineering a high-end micro-CT scanner.

Animal handling: In the course of the present work, several mice were used as specimens for ex-vivo imaging. Animal handling and preparation—such as tumor induction—were solely performed by medical professionals. Animal care and experimental protocols were conducted in accordance with German animal protection laws and were approved by local institutional animal care and use committees.

Chapter 2

Theoretical background

This chapter covers the theoretical background, which serves as a basis for the understanding of the experimental results, which are presented in this thesis. At first, a description is given of how X-rays interact with matter, and how X-rays are generated. Thereafter, the imaging technique itself—grating-based phase contrast—is introduced. After that, a description of quantitative computed tomography and the determination of effective energy is given. Finally, the production process of the required X-ray optical components (gratings) is described.

2.1 X-rays and their interaction with matter

When X-rays pass through matter, they interact in several ways, resulting in either absorption or scattering processes. In the classical description of scattering, the electric field of the incoming X-rays interacts with the electrons of the atoms, which leads to acceleration of the electrons, in turn resulting in the emission of a scattered wave. In this description, the wavelength of the scattered wave is identical to the one of the incoming wave, which means that the process is elastic. This type of scattering is described by *Rayleigh scattering*, which is a coherent process, meaning that the phase of the X-ray wave is left unchanged in the interaction. Rayleigh scattering does however not describe a different inelastic and incoherent scattering process that also occurs. Here, energy is transferred from the X-ray to the electron, which results in scattered X-rays of lower energy. For the understanding of this effect, a quantum mechanical description and the particle aspect of X-rays are required. The associated physical effect is *Compton scattering*. Yet another interaction process of relevance, which results in total absorption of the incoming X-rays, is the *photoelectric effect*. In general, there are further

interaction processes (e.g. pair production), but these are not of concern for the X-ray energies that are used for imaging in this work.

For the formation of phase contrast, the physical basis is Rayleigh scattering, and for the formation of attenuation contrast, the main contribution arises from the photoelectric effect. At higher X-ray energies and with increasing atomic number, Compton scattering becomes an additional attenuating mechanism.

To describe the formation of image contrast quantitatively, a phenomenological approach is sufficient. This approach is based on the *complex index of refraction*, and is introduced in the following.

2.1.1 Refractive index

The complex refractive index is given as:

$$n = 1 - \delta + i\beta. \quad (2.1)$$

Far from absorption edges, δ and μ for one element are given by (Als-Nielsen and McMorow, 2011):

$$\delta = \frac{\lambda}{2\pi} \rho_A (\lambda r_0 Z) = \frac{\lambda}{2\pi} \rho_A \sigma_p, \quad (2.2)$$

$$\beta = \frac{\lambda}{4\pi} \rho_A \sigma_a, \quad (2.3)$$

with wavelength λ , Thomson scattering length $r_0 = 2.82 \cdot 10^{-15}$ m, atomic number Z , and atomic number density ρ_A . σ_p and σ_a are the phase-shift and absorption cross section respectively.

The absorption process is described by the real part β , and the phase shift is described by the decrement of the refractive index, δ . This can be easily understood when considering the propagation of a plane electromagnetic wave (with wave number \mathbf{k}) through a medium of refractive index n :

$$\Psi(\mathbf{r}) = \Psi_0 e^{i\mathbf{n}\mathbf{k}\cdot\mathbf{r}} = \Psi_0 \underbrace{e^{i(1-\delta)\mathbf{k}\cdot\mathbf{r}}}_{\text{phase shift}} \underbrace{e^{-\beta\mathbf{k}\cdot\mathbf{r}}}_{\text{absorption}}. \quad (2.4)$$

Schematically, both effects are presented in Fig. 2.1. The phase is shifted by $\Delta\phi$ and the amplitude is reduced by ΔA .

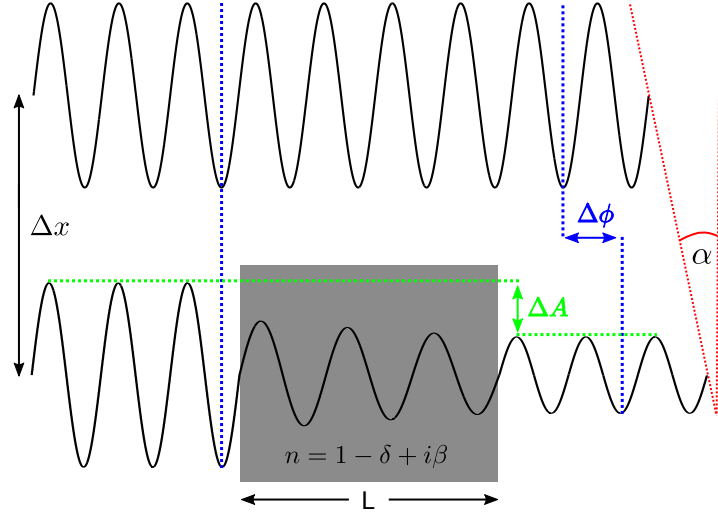


Figure 2.1: Phase shift and attenuation of a wave passing through matter of refractive index n . Inside the medium, the wave is shifted in phase with respect to the wave propagating in free space by $\Delta\phi$. The amplitude is reduced (attenuated) by ΔA .

Absorption: The change in amplitude of the wave is given by $\Delta A = \Psi_0(1 - e^{-\beta kL})$, with L denoting the path length in the material. Transmission is then correspondingly given by:

$$T = \frac{I}{I_0} = \frac{|\Psi|^2}{|\Psi_0|^2} = e^{-2k\beta L}. \quad (2.5)$$

With the absorption coefficient $\mu = 2k\beta$, the intensity I is given by:

$$I = I_0 e^{-\mu L}. \quad (2.6)$$

which is known as *Beer-Lambert* law.

Phase shift: The phase shift of the wave, which traveled through the medium, relative to the one that traveled in vacuum, is given by (Paganin, 2006):

$$\Delta\phi = \delta \mathbf{k} \cdot \mathbf{r}. \quad (2.7)$$

In the general case of X-rays traveling in y -direction, this can be rewritten to (Paganin, 2006):

$$\Delta\phi = k \int \delta(x, y) dy. \quad (2.8)$$

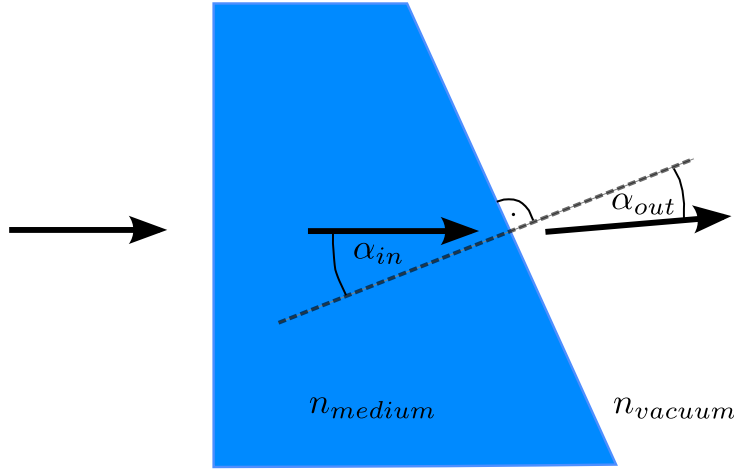


Figure 2.2: Refraction of X-rays at a wedge in vacuum. The incident angle of the X-rays is orthogonal to the first surface and refraction only occurs at the second surface.

The associated change in direction of propagation is given by $\alpha = \frac{\Delta\phi/k}{\Delta x}$ (see Fig. 2.1), and in general terms by (Paganin, 2006):

$$\alpha(x) = \frac{\partial\phi(x, y)/k}{\partial x} = \frac{\partial}{\partial x} \int \delta(x, y) dy. \quad (2.9)$$

Refraction: In order to illustrate the magnitude of typical refraction angles for X-rays, the case of a well defined wedge is considered. For the wedge shown in Fig. 2.2, we apply Snell's law. The incidence of X-rays is orthogonal to the first surface and hence no refraction occurs. For the second surface (medium/vacuum), it is:

$$\frac{\sin(\alpha_{in})}{\sin(\alpha_{out})} = \frac{n_{vacuum}}{n_{medium}}. \quad (2.10)$$

For small angles with $\sin(\alpha) \approx \alpha$, and $n_{vacuum} = 1$, this results in:

$$\alpha_{out} = \alpha_{in} n_{medium}. \quad (2.11)$$

With the real part of the refractive index being $\Re(n) = 1 - \delta$ (see Eq. 2.1), and the fact that $\delta > 0$, this means that n is smaller than 1 and α_{out} is consequently smaller than α_{in} . When comparing this with the optical light regime, it becomes apparent that the direction of refraction of X-rays is

opposite to the one of visible light.

The change in direction of propagation, in other words the refraction angle α_r , is given by:

$$\begin{aligned}\alpha_r &= \alpha_{out} - \alpha_{in}, \\ &= \alpha_{in}(n_{medium} - 1).\end{aligned}\tag{2.12}$$

for the real part of n , it is $n = 1 - \delta$ and it hence follows that:

$$\alpha_r = -\delta\alpha_{in}.\tag{2.13}$$

For typical X-ray wavelengths (10 – 100 keV), δ is of the order $10^{-8} \leq \delta \leq 10^{-6}$ (Chantler, 1995), which means that typical refraction angles are on the order of micro degrees and smaller.

The employed phase-sensitive imaging technique in this thesis relies on the accurate detection of this refraction angle and its small magnitude makes the use of sophisticated instrumentation necessary. Section 2.3 introduces a grating-based interferometric technique, which permits measuring this refraction angle and which is the instrument of use in this thesis.

2.1.2 Coherence

Coherent waves are waves, which are ‘in phase’ with one another. This idealization is never completely fulfilled for real X-ray waves and the concept of *coherence length* is introduced. The following considerations and graphical illustration are adapted from the textbook by Als-Nielsen and McMorrow (2011) (Chapter 1.5).

A real X-ray wave can deviate in two aspects from an ideal plane-wave state: it is never perfectly monochromatic and it does never propagate perfectly collinear. Both aspects are illustrated in Fig. 2.3. First, we will consider two plane waves in (a), which travel in exactly the same direction and which feature slightly different wavelengths λ . On the left side of the figure, the two waves are in phase, and they are in phase again after traveling the distance $2L_L$. This implies that the waves have been exactly out of phase in between, and this distance is referred to as the *longitudinal coherence length* L_L . If the full distance $2L_L$ corresponds to N wavelengths of λ (green wave), or to $N+1$ wavelengths of $\lambda - \Delta\lambda$ (blue wave), it is:

$$2L_L = N\lambda = (N + 1)(\lambda - \Delta\lambda),\tag{2.14}$$

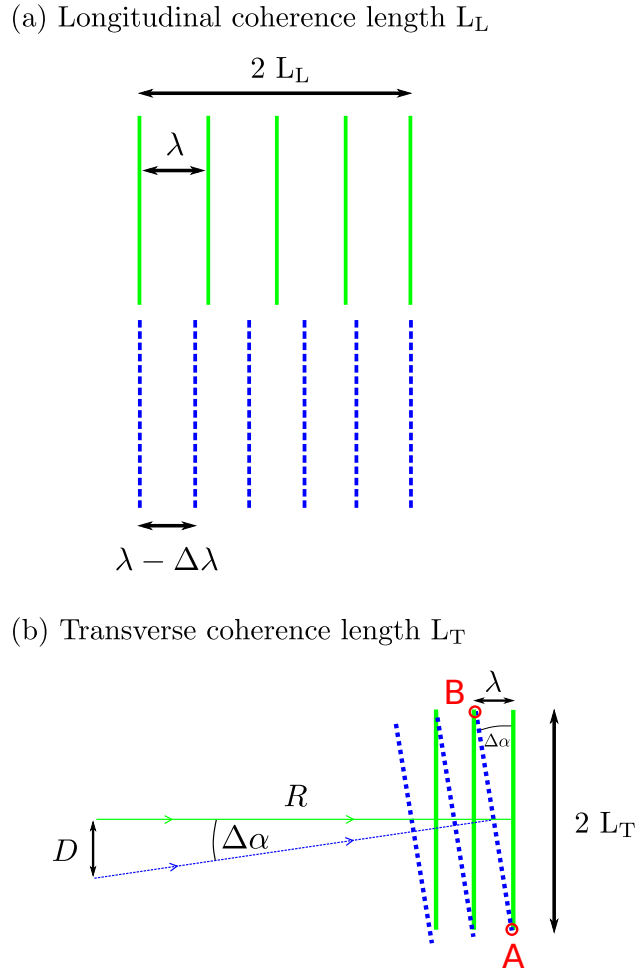


Figure 2.3: Longitudinal and transverse coherence length. (a) Two plane waves travel in the same direction and differ by $\Delta\lambda$ in wavelength. After traveling a distance of L_L they are out of phase. (b) Two plane waves feature the same wavelength and propagate with an inclination of $\Delta\alpha$. This inclination is caused by the emission from two distinct points with a spacing of D . After a distance of L_T both waves are out of phase. This figure was adapted from the textbook by Als-Nielsen and McMorrow (2011).

provided that

$$(N + 1)\Delta\lambda = \lambda. \quad (2.15)$$

Combining both equations, the longitudinal coherence length can be expressed as:

$$L_L = \frac{1}{2} \frac{\lambda^2}{\Delta\lambda}. \quad (2.16)$$

In panel (b), the second deviation from the ideal plane wave is considered: both waves have the same wavelength, but travel in slightly different directions, deviating by $\Delta\alpha$. The wavefronts coincide and hence are in phase at the two points A and B. The *transverse coherence length* L_T is defined as the distance (along the wavefront) after which both waves are out of phase. This out-of-phase condition has necessarily been met in the middle of the points A and B. In the case of small angles, it is: $\Delta\alpha = \lambda/2L_T$. If the difference in direction of propagation arose because the two waves originated from two points of a source, with a spacing of D , at a distance R , then it is further: $\Delta\alpha = D/R$. For the transverse coherence length L_T , this results in:

$$L_T = \frac{\lambda R}{2 D} \quad (2.17)$$

This means that the transverse coherence length, which is of relevance for the imaging technique employed in this thesis, is directly correlated to the angle under which the source appears.

2.1.3 Free-space propagation

As we have seen before, the wavefront of X-rays, which propagate through matter, changes due to interactions with matter. The wavefront however also changes during propagation in free space and this is considered in the following.

The *Huygens-Fresnel principle* states that the wavefront at any moment may be considered as the sum of spherical wavelets distributed on that wavefront. Based on this principle, the wavefront at a later point can be calculated by integrating over all individual contributions of these wavelets. Analytically, this is formulated in the *Fresnel-Kirchhoff diffraction integral* (Born and Wolf, 1998):

$$\Psi(x, y, z) = \frac{1}{i\lambda} \iint \Psi(x', y', 0) \frac{e^{i\mathbf{k}\cdot\mathbf{r}}}{r} \cos(\mathbf{n}, \mathbf{r}) dx' dy'. \quad (2.18)$$

Every point of the incoming wavefront $\Psi(x', y')$ (in the plane $z' = 0$) acts as the source of a spherical wave $e^{i\mathbf{k}\cdot\mathbf{r}}/r$. The wavefront at the image plane $\Psi(x, y, z)$ is then described by the superposition of all these point sources. The unit vector \mathbf{n} points into the direction of propagation, while \mathbf{r} reaches from the origin to the considered point in the image plane. The factor $\cos(\mathbf{n}, \mathbf{r})$ takes this inclination into account.

In order to solve this integral, several approximations can be made. In the case of small deflection angles (*paraxial approximation*), which are present in the case of hard X-rays, the following assumptions are made: $\cos(\mathbf{n}, \mathbf{r}) \approx 1$ and $r \approx z$.

In e^{ikr} , however, r cannot be approximated by z . Here, a Taylor expansion can be applied to r , which results in:

$$\begin{aligned} r &= \sqrt{z^2 + (x - x_0)^2 + (y - y_0)^2}, \\ &= z \sqrt{1 + \frac{(x - x_0)^2}{z^2} + \frac{(y - y_0)^2}{z^2}}, \\ &= z \left[1 + \frac{1}{2} \frac{(x - x_0)^2}{z^2} + \frac{1}{2} \frac{(y - y_0)^2}{z^2} + \mathcal{O}(x^4, y^4, z^{-4}) \right]. \end{aligned} \quad (2.19)$$

If we only consider terms of the second degree, this simplifies the diffraction integral and we reach the so-called *Fresnel approximation*:

$$\Psi(x, y, z) = \frac{e^{ikz}}{i\lambda z} \iint \Psi(x', y', 0) e^{\frac{ik}{2z}[(x-x')^2 + (y-y')^2]} dx' dy'. \quad (2.20)$$

Here the wave originates in $(x', y', z = 0)$ and moves along z -direction.

This integral can also be seen as a convolution of the wave function $\Psi(x', y', z = 0)$ with a *propagator function* $h(x, y, z)$:

$$h(x, y, z) = \frac{e^{ikz}}{i\lambda z} e^{i\frac{k}{2z}(x^2 + y^2)}. \quad (2.21)$$

The convolution then reads:

$$\Psi(x, y, z) = \Psi(x', y', 0) * h(x, y, z), \quad (2.22)$$

with $*$ denoting the convolution operator. When combining this equation with the convolution theorem, which states:

$$\mathcal{FT}\{f(x, y) * g(x, y)\} = \mathcal{FT}\{f(x, y)\} \cdot \mathcal{FT}\{g(x, y)\}, \quad (2.23)$$

the equation can be rearranged further to read:

$$\Psi(x, y, z) = \mathcal{FT}^{-1} \left[\mathcal{FT}\{\Psi(x', y', 0)\} \cdot \mathcal{FT}\{h(x, y, z)\} \right]. \quad (2.24)$$

This means that the wavefront at any given point $\Psi(x, y, z)$ is accessible by a multiplication (in Fourier space) of the current wavefront and the propagator function. This circumstance is of practical interest for numerical calculations of wavefront propagation, which will be performed at a later stage in section 2.3.2.

2.2 X-ray sources

So far, we considered fundamental properties of X-rays and their interaction with matter. In this section, the generation of X-rays is reviewed briefly. In general, nowadays, there are different ways of generating X-rays and here the two types of sources that are used later-on in this work are considered: X-ray tubes and synchrotron radiation. The main characteristics of the generated X-rays and corresponding implications for imaging are also considered briefly.

2.2.1 X-ray tube

In an X-ray tube, electrons are emitted from a cathode and are accelerated towards an anode by a high voltage in the kV-range. When striking the anode, the electrons are strongly decelerated and stopped eventually. This deceleration process gives rise to the formation of X-rays with a broad energy spectrum, which is called *Bremsstrahlung*. The maximum X-ray energy in this spectrum is given by the maximum kinetic energy of the electrons. In the collision with an atom, the incident electron may also remove an atomic electron from its shell. The subsequent relaxation of an electron from an outer shell produces fluorescence radiation of a characteristic energy. Target-material-specific *fluorescence lines* are hence superimposed on the continuous Bremsstrahlung spectrum. A tube source and a typical spectrum are sketched in Fig. 2.4.

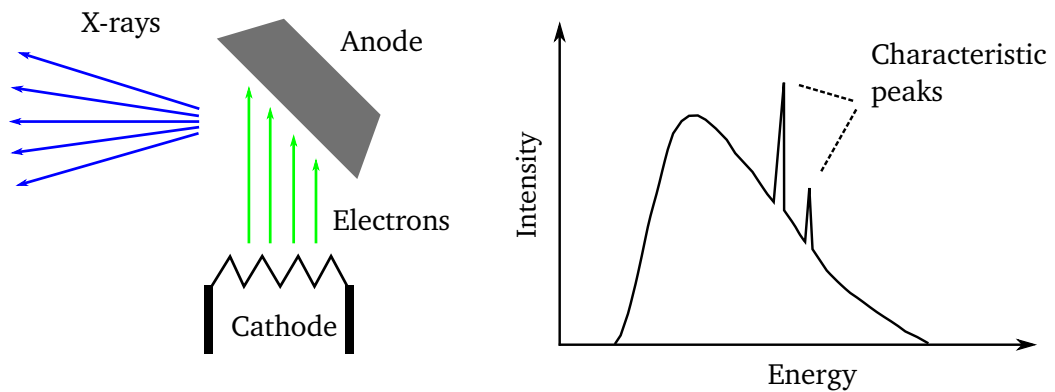


Figure 2.4: X-ray tube source. (Left) X-rays are generated by the deceleration and eventual stopping of the electrons in the anode material, giving rise to a broad spectrum of energies (Bremsstrahlung). Additionally, X-rays with a characteristic energy are produced by fluorescence. The resulting spectrum is shown schematically on the right side.

The illustrated working principle also applies to state-of-the art X-ray tube sources. For imaging applications, these are technologically highly optimized with respect to either of the following aspects: i) Reduction of the focal spot size, i.e. the area from which X-rays are emitted, which increases the spatial resolution in imaging. To this end, so-called microfocus tubes are available. ii) Maximizing the flux of X-rays to reduce the acquisition time. The latter is difficult due to the generation of heat at the anode, which obviously should not result in an exceedance of the melting point of the anode material. Besides sophisticated cooling, tubes with a *rotating anode* were developed, in which the generated heat is dissipated over a larger area.

2.2.2 Synchrotron radiation

In general, when charged particles are accelerated, they emit electromagnetic radiation. When emission of this kind occurs in a charged particle storage ring, where the particles are permanently accelerated towards the center, it is referred to as *synchrotron radiation*. In such a storage ring, the particles, usually electrons, are kept at constant kinetic energy and are guided along a circular path by strong magnetic fields. Originally, storage rings were built for particle-physics experiments and were not optimized for the generation of synchrotron radiation. A synchrotron light source on the other hand is solely designed for this purpose and consists of a combination of different electron accelerators, and a storage ring. X-rays are either generated at *bending magnets* or at dedicated *insertion devices*, and the radiation is then available in imaging stations, which are located on different beamlines. The insertion devices are periodic magnetic structures of several meters in length that induce the emission of highly brilliant, forward-directed synchrotron radiation. This is achieved by forcing the charged particles, via strong magnets exerting a Lorentz force, onto a sine-shaped trajectory—the particle beam performs ‘wiggles’ or ‘undulations’. The corresponding devices are hence referred to as *wiggler* and *undulator*. A detailed treatment of the physics of the generation of synchrotron radiation would exceed the scope of this thesis and can be found, for example, in the textbook by Als-Nielsen and McMorrow (2011). Here, only the relevant parameters for imaging shall be mentioned. The radiation is emitted in an extremely forward-directed cone due to a relativistic effect. The flux of X-rays, when compared to tube sources, is several orders of magnitude higher. Undulators emit spatially partially coherent radiation with a narrow energy spectrum, and wigglers produce spatially incoherent radiation with a broad energy spectrum.

Schematically, a wiggler and a corresponding energy spectrum are shown in Fig. 2.5. As an example for illustration, the storage ring at the European

Synchrotron Radiation Facility (ESRF) in Grenoble, France, has a circumference of 844 m and the electrons have an energy of 6 GeV. At beamline ID 19, where all synchrotron-based experiments in this work were performed, a combination of wigglers and undulators is installed, delivering X-rays with an energy range of 7 to 100 keV (Weitkamp et al., 2010).

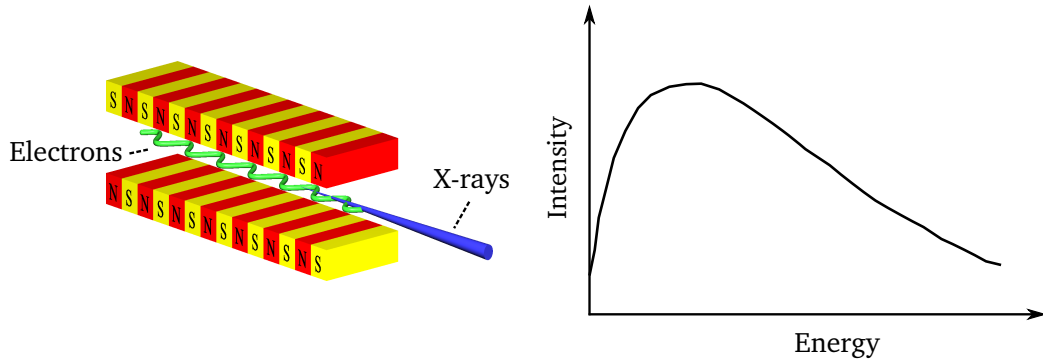


Figure 2.5: Synchrotron radiation. (Left) A beam of charged particles, typically electrons, is deflected periodically by an array of magnets. This periodic movement implies an acceleration, which in turn results in the emission of synchrotron radiation. (Right) In the case of a wiggler, a continuous spectrum of X-rays is produced.

2.3 Grating-based phase-contrast imaging

2.3.1 Introduction

Grating-based phase-contrast imaging yields three images that are referred to as attenuation-contrast image, phase-contrast image and dark-field image. The attenuation image is based on measuring the attenuation of X-ray intensity and the phase-contrast image is based on measuring the refraction angle of the X-rays. Dark-field contrast is also based on the refraction of X-rays, but the refraction angles, which generate contrast in the dark-field image, are significantly smaller and are referred to as scattering. The reason for this discrimination will become apparent when the technical details of the technique are presented (section 2.3.3).

As we have seen before, typical refraction angles for X-rays are extremely small—on the order of micro degree. This is why refraction is not visible in conventional radiography or computed tomography. The basic idea for

measuring the X-ray refraction angles is based on the use of a spatial reference, relative to which the refraction can be determined. As the technique shall image extended objects, an area reference pattern has to be used. The local refraction of X-rays in the object then translates into a local lateral shift of this reference pattern. The instrument that can measure this local lateral displacement is the *grating interferometer*. As the name suggests, an interference effect is used to generate the reference pattern, i.e. the pattern is produced by spatially coherent illumination of a periodic grating structure. If the spatial frequency of the reference pattern is sufficiently small, then these small lateral displacements, which are caused by refraction, can be measured accurately.

When illuminating a grating with coherent X-rays, the so-called *Talbot self-imaging effect* occurs (Talbot, 1836), which is based on the Huygens-Fresnel principle and wave propagation in free space. Essentially, the Talbot effect is used to generate the spatial reference pattern. To spatially resolve the refraction-induced local changes in the reference pattern, a second grating is employed. Together with the X-ray source, the sample, and a conventional imaging detector, these two gratings make up the imaging setup. In case incoherent radiation—as originating from conventional tube sources—is employed, a third grating has to be used and the setup is then referred to as *Talbot-Lau interferometer*. Depending on the relative distance of source, sample, grating and imaging detector, geometrical magnification can occur resulting in either a *parallel-beam* or a *cone-beam geometry* setup.

2.3.2 Talbot effect

The Talbot effect is a self-imaging phenomenon that was first reported for visible light in 1836 by Henry Fox Talbot (Talbot, 1836). Self-imaging in this context means that an image is formed without any lens or optical component between the object and the image. Talbot observed that an absorbing periodic object, illuminated by coherent light, produces self images at certain distances along the optical path. This effect can be explained by the Huygens-Fresnel principle applied to the propagation of a periodically modulated wave front. This self image occurs at a certain distance, referred to as *Talbot distance* d_T , and depends on the periodicity of the object p and the wavelength λ :

$$d_T = \frac{2p^2}{\lambda}. \quad (2.25)$$

Later it was found that the Talbot effect is a special case in a larger class of self-imaging effects, namely it was found by Montgomery in 1967 that also quasi-periodic structures exhibit self-imaging (Montgomery, 1967). In

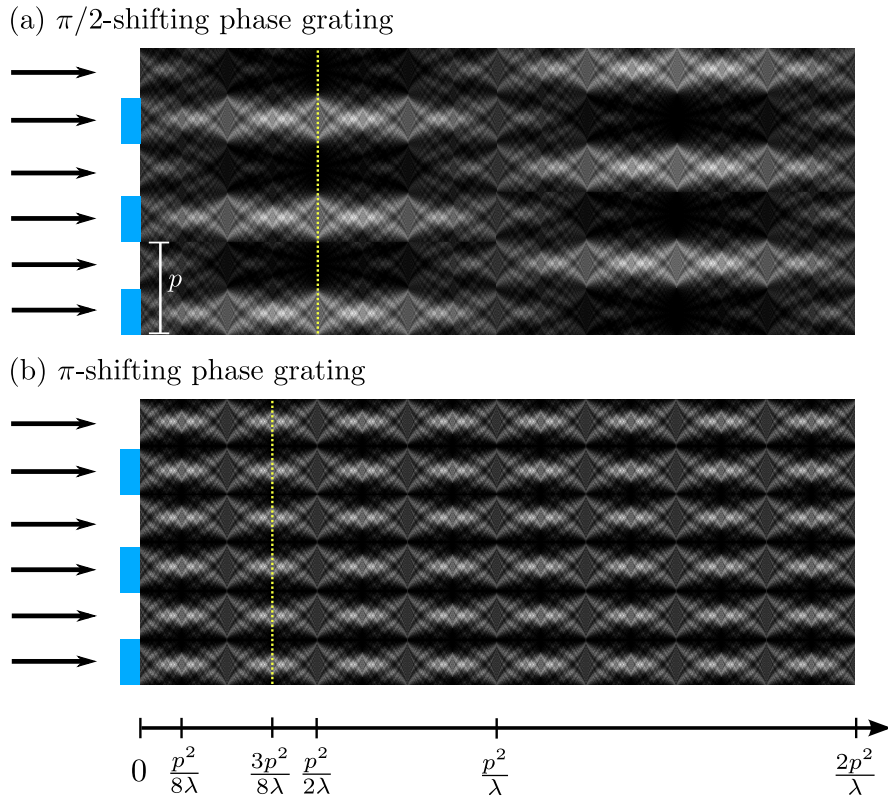


Figure 2.6: X-ray intensity pattern behind a phase grating with a pitch of p , which is illuminated by a plane monochromatic wave with full transverse coherence: (a) grating with a phase shift of $\pi/2$, (b) grating with a phase shift of π . At certain distances (fractional Talbot distances) downstream of the grating, a binary intensity pattern is formed. For both phase gratings, one exemplary fractional Talbot distance is highlighted by a dashed line.

a consecutive work of Lohmann et al. (2005), it was then shown that the mentioned Talbot images represent a subset of the so-called Montgomery images.

Of relevance for the imaging technique is the fact that self images can be observed at integer multiples of the Talbot distance $d = md_T$ (with $m = 1, 2, 3, \dots$) and at certain fractions $d = (m/n)d_T$ (with m and n as integer), for example: $d = (1/2)d_T$, $d = (3/8)d_T$, $d = (5/16)d_T$. These distances are referred to as full Talbot distance and as fractional Talbot distance respectively.

For illustration, Fig. 2.6 displays the X-ray intensity behind a binary phase grating structure with a duty cycle of 0.5, i.e. half of the grating introduces

a phase shift and half of the grating does not. The X-ray intensity pattern is plotted for a phase grating inducing a phase shift of $\pi/2$ (a) and for a phase grating with a shift of π (b). The intensity pattern was generated using free-space wave propagation (compare section 2.1.3) with full transverse coherence. Dashed lines indicate fractional Talbot distances and the intensity pattern is plotted up until one full Talbot distance ($2p^2/\lambda$). The particular feature of interest at the fractional Talbot distance is that the intensity pattern is box-shaped and periodical. The periodicity of this pattern is the same as the one of the phase grating for the $\pi/2$ -grating and is halved for the π -grating.

At closer inspection we can see the following regularity for fractional Talbot distances $d_{T,f}$ using the notation introduced by Weitkamp et al. (2006):

$$d_{T,f} = \frac{1}{\eta^2} \frac{np^2}{2\lambda} \quad (n = 1, 3, 5, \dots). \quad (2.26)$$

with η distinguishing the phase shift ϕ of the grating and period of the interference pattern p/η as follows:

$$\eta = \begin{cases} 1, & \text{for } \phi = \pi/2. \\ 2, & \text{for } \phi = \pi. \end{cases} \quad (2.27)$$

Maximum intensity modulations only occur at odd numbers for the integer n . This number is also called the order of the fractional Talbot distance. Following this notation, in Fig. 2.6, the 1st fractional Talbot order is highlighted in (a) and the 3rd order in (b).

Of relevance for the imaging technique are these fractional Talbot distances as they represent a regular intensity pattern, which serves as spatial reference for determining the refraction angle.

2.3.3 Grating interferometer

The fundamental idea behind a grating interferometer is the following: spatially coherent X-rays illuminate a phase-shifting grating, resulting in a periodic intensity pattern at a certain distance downstream according to the Talbot effect. A sample in the beam modifies the X-ray wave and the resultant change in the interference pattern is detected with a second grating, which is referred to as analyzer grating. According to the described interactions of X-rays with matter, potential wave front modifications are:

- (a) Decrease in overall intensity due to attenuation.
- (b) Lateral shift of the interference pattern due to refraction.
- (c) Decrease of interference pattern amplitude due to scattering.

All three effects are sketched in Fig. 2.7. A plane X-ray wave gives rise to an interference pattern at a certain distance downstream, corresponding to a full or fractional Talbot distance. The alteration of the wave front—caused by a purely attenuating (a), refracting (b) and scattering (c) object—are displayed. Attenuation results in an overall decrease of intensity, refraction results in a lateral shift of the interference pattern, and scattering results in a decrease of oscillation amplitude. In order to understand how the analyzer grating measures these changes in the interference pattern, the so-called phase-stepping scan has to be considered.

Phase-stepping scan: In this procedure either of the gratings is moved in the direction orthogonal to X-ray wave propagation and at each grating position an image is taken. This movement is indicated by arrows in Fig. 2.7, for the case that the phase grating is stepped. The grating bars of the analyzer grating are highly absorbing and are typically made of gold. This means that, ideally, they do not transmit any intensity at the position of the bars and transmit the full intensity in between. The movement of the interference pattern relative to the absorbing grating bars, with intermediate image acquisition, samples the shape of the interference pattern. The period of the analyzer grating is deliberately chosen to match the period of the interference pattern, hence avoiding the occurrence of Moiré fringes. Moiré fringes are periodic intensity modulations due to the Moiré effect that arises when two nearly identical periodic structures are superimposed. For further details, the reader is referred to a study by Weitkamp et al. (2004). The result of the phase-stepping scan is a periodic intensity curve for each pixel of the detector. The shape of the measured curve is determined by the shape of the interference pattern, the transmission of the analyzer grating, and the detector response. It can be shown that, in the case of moderate coherence, this curve is sine-shaped (Bech, 2009). Please note that, as the size of the pixels is typically several times as large as the grating pitch, the average intensity of the transmission for several grating bars is recorded. For illustration, schematic phase-stepping curves for one detector pixel are shown in Fig. 2.8. The recorded intensity is plotted versus the position of the grating x_n in fractions of one full interference pattern period p_2 . Black dots represent the measured intensity. The blue curve shows a stepping curve for

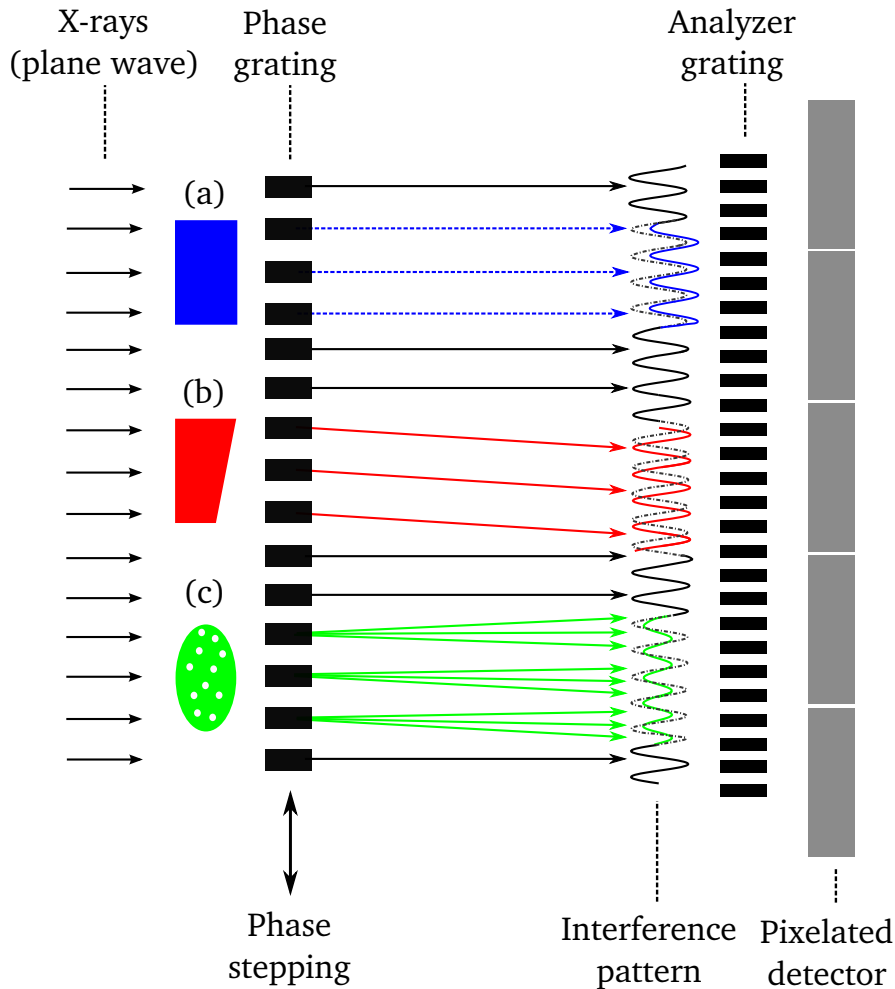


Figure 2.7: Sketch of the working principle of a Talbot interferometer: (a) Attenuation resulting in a reduced average intensity of the interference pattern. (b) Refraction resulting in a lateral shift of the interference pattern. (c) Scattering resulting in a reduced amplitude of the interference pattern.

the case with no object in the beam, and it hence purely maps the interference pattern. The red curve shows the case with an object in the beam with the following modifications of the wave front: (a) attenuation, (b) refraction, and (c) scattering.

This curve is the basis for the extraction of the three image-contrast mechanisms that are available with a grating interferometer. In the following, the required intermediate data processing step for obtaining the three contrast images is explained.

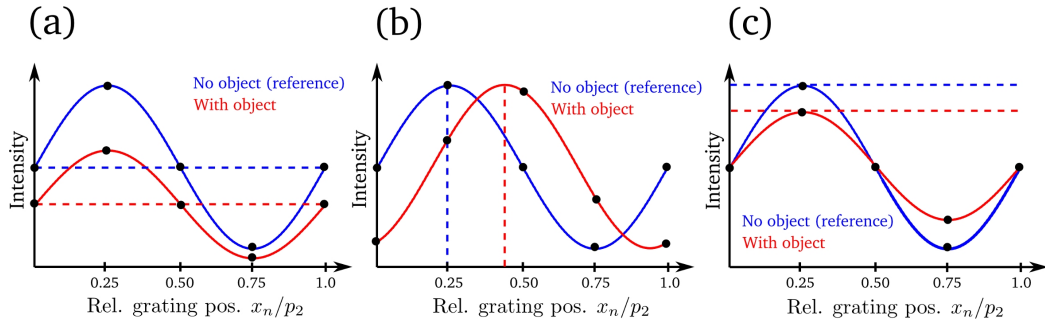


Figure 2.8: Phase-stepping scan. The black dots represent the recorded intensity at different grating positions x_n in fractions of one full interference pattern period. The blue curve shows the case with no object in the beam, and it purely maps the interference pattern. The red curve shows the case with an object in the beam for: (a) attenuation, (b) refraction, and (c) scattering.

Fourier processing of the phase-stepping curve: The recorded intensity in each pixel, I , during a phase-stepping scan at different grating positions, x_n , can be described by a Fourier series:

$$I(x_n) = \sum_{m=0}^{\infty} a_m \cos\left(m \frac{2\pi}{p_2} x_n + \phi_m\right), \quad (2.28)$$

with the amplitude coefficients a_m , the phase coefficients ϕ_m , the period of the analyzer grating p_2 , and x_n denoting the grating position during the phase-stepping scan. When only considering the first order—which is a sufficient approximation for moderate coherence—the intensity can be described by (Bech, 2009):

$$I(x_n) = a_0 + a_1 \cos\left(\frac{2\pi}{p_2} x_g + \phi_1\right), \quad (2.29)$$

with the average value (offset) a_0 , phase ϕ_1 , and oscillation amplitude a_1 .

The phase-stepping curve is recorded once without the object in the beam and once with the object in the beam. The curve without the object in the beam accounts for the fact that under experimental conditions, the interference pattern is never absolutely regular and can change over time. It hence represents a reference, relative to which the modulation of the wave front is determined. The curve with the object in the beam then records the modulations of the wave front.

With this description of the intensity curve, we regard the phase-stepping

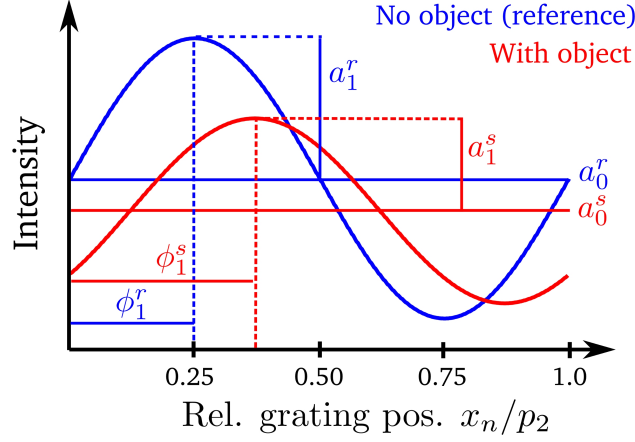


Figure 2.9: Fourier analysis of the phase-stepping curve. The intensity measured in one pixel during a phase stepping scan with and without the object in the beam is plotted. The Fourier components a_0 , a_1 , and ϕ_1 are indicated. Superscript r indicates the reference scan and superscript s indicates the scan with sample in the beam.

curve again, in this case with all three modulations present at once—as for a real object—with the corresponding Fourier components a_0 , a_1 , and ϕ_1 labeled. Superscript r indicates the reference scan (without sample) and superscript s indicates the scan with sample in the beam. The corresponding plot is shown in Fig. 2.9. The amplitude of the oscillation is an important performance parameter of the interferometer as it is a direct measure for the degree of the interference. Usually, the ratio of $(I_{\max} - I_{\min}) / (I_{\max} + I_{\min})$ is quoted in this context and this value is referred to as interferometer *visibility*. In terms of the introduced Fourier components, interferometer visibility V_r can be expressed as:

$$V_r = \frac{a_1}{a_0}. \quad (2.30)$$

Transmission is contained in the ratio of the offset of both phase-stepping curves:

$$T = \frac{a_0^s}{a_0^r}. \quad (2.31)$$

The physical transverse shift of the interference pattern is proportional to the difference in phases of both curves:

$$\phi = \phi_1^s - \phi_1^r. \quad (2.32)$$

The change in oscillation amplitude or visibility, when using Eq. 2.30, is described by (Pfeiffer et al., 2008):

$$V = \frac{V^s}{V^r} = \frac{a_0^r a_1^s}{a_0^s a_1^r}. \quad (2.33)$$

Trimodal contrast images: So far, the intensity curve was considered for one single pixel. As the imaging detector records this curve $I(p_x, p_y, x_g)$ for all pixels (p_x, p_y) at each grating position x_g , 2D images in all three contrasts can be obtained. Commonly in radiographic imaging, the attenuation image, rather than the transmission image, is regarded. It is given by: $A(p_x, p_y) = 1 - T(p_x, p_y)$. The three contrast images hence simply are the spatial distribution of $A(p_x, p_y)$, $\phi(p_x, p_y)$, and $V(p_x, p_y)$. In analogy to optical microscopy, the scatter-induced image is called dark-field image (Pfeiffer et al., 2008). Physically, it maps (ultra) small-angle scattering, which is on a length scale that cannot be resolved by the interferometer. The actual transverse shift $S(p_x, p_y)$ of the interference pattern is proportional to the value $\phi(p_x, p_y)$ and is given by:

$$S(p_x, p_y) = \frac{p_2}{2\pi} \phi(p_x, p_y). \quad (2.34)$$

When the distance between the two gratings is termed d , then this transverse shift corresponds to a refraction angle of:

$$\alpha(p_x, p_y) = \frac{p_2}{2\pi d} \phi(p_x, p_y). \quad (2.35)$$

By use of the equation that relates refraction angle and the phase of the wavefront (Eq. 2.9), the differential phase shift of the wave-front behind the sample reads:

$$\frac{\partial \Phi(p_x, p_y)}{\partial x} = \frac{2\pi}{\lambda} \alpha(p_x, p_y) = \frac{p_2}{\lambda d} \phi(p_x, p_y). \quad (2.36)$$

This means that the refraction-induced image maps the differential phase, which is why the image is referred to as *differential phase-contrast image*.

In conclusion, the three images that are recorded with a grating interferometer are:

- Attenuation: $A(p_x, p_y) = 1 - T(p_x, p_y)$.
- Differential phase contrast: $DPC(p_x, p_y) = \phi(p_x, p_y) \cdot (p_2/\lambda d)$.
- Dark field: $DF(p_x, p_y) = V(p_x, p_y)$.

Please note that all three images are intrinsically perfectly registered as they originate from one common dataset.

2.3.4 Use of incoherent radiation

Transverse coherence: As shown in the previous section, the operating principle of the grating interferometer relies on interference. This requires transverse coherence to an extent that the interference pattern exhibits sufficient visibility. The coherence requirement only has to be met in the direction perpendicular to the grating bars, in the direction along the grating bars, interference is not required. As illustrated in section 2.1.2, spatial coherence is directly related to the size and distance of the source. The impact of an extended source on the interference pattern can be understood by considering each point in the extended source as an independent point source. Each of these points creates an interference pattern behind the phase grating. The effect of the multitude of these laterally displaced points, in other words the extended source size, is a blurring of the interference pattern. This circumstance can be illustrated by the projected source size, which is shown schematically in Fig. 2.10. Geometrically, the projected source size s' can be calculated by:

$$s' = \frac{d}{L}s, \quad (2.37)$$

with source size s , inter-grating distance d and source to phase grating distance L . Analytically, the influence of an extended source can be described by a convolution of the interference pattern profile with the source profile at the plane of the analyzer grating. It can be shown that the visibility decreases exponentially with increasing source size, and it almost reaches zero for projected source sizes, which are larger than half the period of the interference pattern (Bech, 2009).

In order to overcome this effect, a third, so-called *source grating*, can be used. Such a grating consists of absorbing bars (typically made of gold as in the case of the analyzer grating) and essentially splits the large focal spot of high-power sources into an array of sources, for which the coherence requirement is met for each individual source. Neighboring slits are mutually incoherent and the *intensity* of each slit's interference pattern superimposes

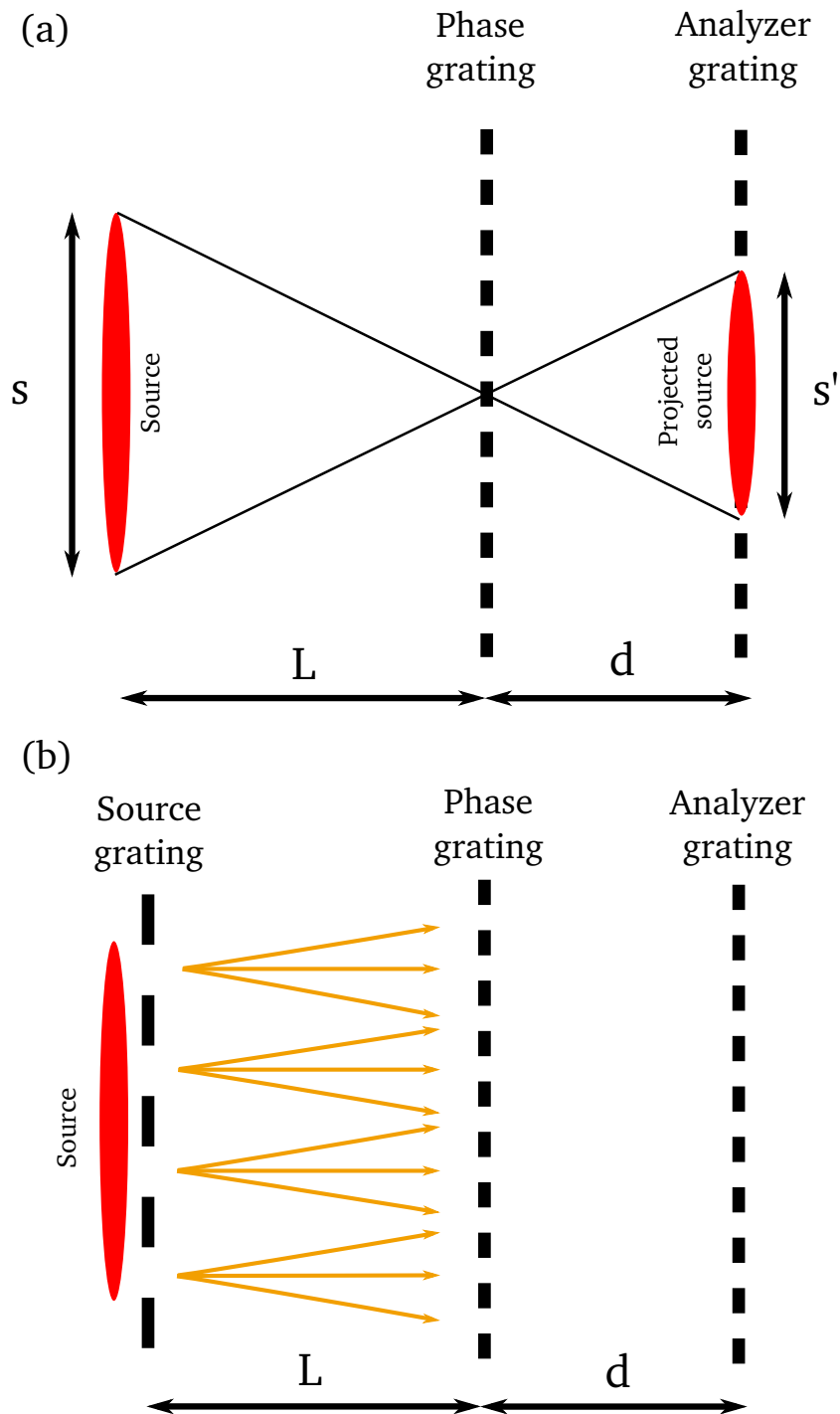


Figure 2.10: Transverse coherence. (a) A source of size s results in a projected source size s' at the plane of the analyzer grating, effectively blurring the interference pattern. (b) Use of a source grating that creates an array of individually coherent, but mutually incoherent sources. With an adequate choice of grating periods (see Eq. 2.38), the interference patterns of each slit add up.

in the plane of the analyzer grating. For this superposition to happen in an amplifying manner, the space between the interference patterns from two neighboring slits has to be exactly one, or an integer multiple of one period of the pattern. This geometric constraint is fulfilled for:

$$p_0 = \frac{L}{d}p_2, \quad (2.38)$$

with the period of the source grating p_0 and period of the interference pattern p_2 . This principle is known as the *Lau effect* and the corresponding three-grating interferometer is called *Talbot-Lau interferometer*.

As shown by Pfeiffer et al. (2006) and Weitkamp et al. (2006), the use of a source grating decouples the size of the X-ray source from the transverse coherence properties. The spatial resolution, however, remains unaffected and is influenced by the projected source size as it would be if no interferometer was used.

When these considerations are put in relation with X-ray tube and synchrotron radiation sources, we can conclude the following:

- For a two-grating Talbot interferometer, transverse coherence, or, in other words, a small projected source size is required. In practice, this can be achieved by either placing the interferometer at a large distance from the source, or by using small-sized sources, on the order of few micrometers. The main drawback of both options for imaging of macroscopic samples is the limit in X-ray flux, which translates into long detector exposure times. Alternatively, synchrotron radiation sources with very large flux can be used.
- For the three-grating Talbot-Lau interferometer, there are no requirements on source coherence. In practice, such an interferometer is typically operated with large flux—and correspondingly large focal spot—tube sources or synchrotron radiation sources of insufficient transverse coherence.

Longitudinal coherence: As we have seen, the Talbot distances depend on the wavelength of the incoming X-rays. The effect of polychromatic radiation is hence a superposition of laterally displaced interference patterns, blurring the final interference pattern to some extent. In the end, this results in a reduced interferometer visibility. Nevertheless, a grating interferometer can be—and routinely is—used efficiently with polychromatic X-ray sources. A thorough analysis of the use of polychromatic X-ray tube sources can be found in Engelhardt et al. (2008).

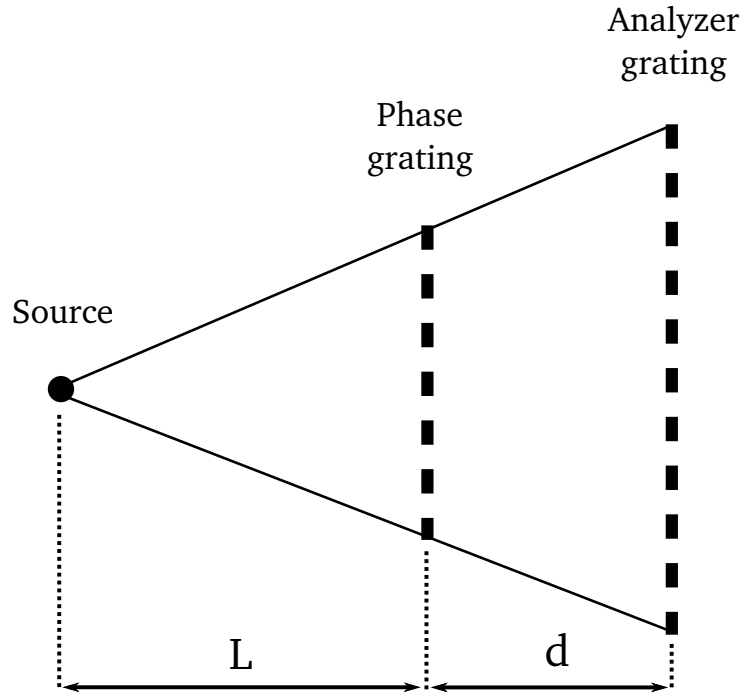


Figure 2.11: Sketch of the geometrical magnification effect in fan-beam geometry.

2.3.5 Geometrical magnification: fan-beam geometry

So far, the parallel-beam case was considered. Especially in a compact setup with divergent X-ray beam, geometrical magnification has to be taken into account. Magnification can be described by a magnification factor M :

$$M = \frac{L + d}{L}, \quad (2.39)$$

with inter-grating distance d and source to phase-grating distance L . Fig. 2.11 sketches such a setup geometry. Due to the magnification of the interference pattern, also the Talbot distances d_T are affected by magnification. The scaled Talbot distances d_T' are given by:

$$d_T' = M d_T. \quad (2.40)$$

If we recall that the period of the analyzer grating should match the period of the interference pattern, it follows that also the analyzer grating period p_2

has to be scaled accordingly:

$$p_2' = Mp_2 = M\frac{p_1}{\eta}, \quad (2.41)$$

with the period of the phase grating p_1 and η distinguishing the phase shift of the phase grating as introduced in section 2.3.2. It should be mentioned that in this consideration, the effect of the local curvature of the wave front is neglected as only a global scaling of the wave is considered. However, this approach is sufficient in practice.

2.4 Computed tomography

2.4.1 General principle

Conventional X-ray computed tomography is a technique that allows for the reconstruction of the 3D distribution of the sample's attenuation properties. The reconstruction of this distribution is based on a series of radiographic projection images at different angles from all around the object. The technique of computed tomography is quantitative, meaning that the reconstructed values represent an absolute physical quantity. For the case of conventional, attenuation-based CT, the reconstructed quantity is the linear attenuation coefficient. For the case of phase-contrast CT, this quantity is the decrement of the refractive index δ (see section 2.1.1). There are many textbooks describing the principle and the mathematical considerations of computed tomography in depth. One of them is 'Principles of Computerized Tomographic Imaging' (Kak and Slaney, 1987). The following explanations are based on this book and describe the case of parallel-beam illumination, for which the reconstruction of adjacent slices (in the direction of the tomography axis) are independent. The special case of cone-beam illumination is briefly mentioned towards the end of the section.

Please note that the field of tomographic reconstruction in general is subject of active research and a huge number of advanced tomographic reconstruction schemes have been developed. These are, however, not discussed in this thesis.

The experimentally acquired projection images are a map of X-ray intensity behind the sample. Mathematically, such a projection is described by the *Radon transform* of the object function $f(x, y)$, which represents the distribution of some physical quantity in the sample (for example the distribution of the linear attenuation coefficient). The projection $\mathcal{P}_\theta(t)$ of the function

$f(x, y)$ for a certain projection angle θ is described by (see Fig. 2.12):

$$\mathcal{P}_\theta(t) = \iint f(x, y) \delta(x \cos \theta + y \sin \theta - t) \, dx dy, \quad (2.42)$$

with the Dirac delta function δ , and $t = x \cos \theta + y \sin \theta$.

In Fourier space, the object function $f(x, y)$ is described by its Fourier transform $\tilde{f}(u, v)$ with:

$$\mathcal{FT} \{f(x, y)\} = \tilde{f}(u, v) = \iint f(x, y) e^{-i2\pi(ux+vy)} \, dx dy. \quad (2.43)$$

The projection of the object function $\mathcal{P}_\theta(t)$ at an angle θ —in Fourier space—is given by $\tilde{P}_\theta(\omega)$:

$$\mathcal{FT} \{\mathcal{P}_\theta(t)\} = \tilde{P}_\theta(\omega) = \int P_\theta(t) e^{-i2\pi\omega t} \, dt, \quad (2.44)$$

with (θ, ω) representing the coordinates (u, v) after the transform in polar coordinates: $(u, v) = (\omega \cos \theta, \omega \sin \theta)$. The *Fourier slice theorem* establishes the link between the last two equations (Eq. 2.43 and Eq. 2.44) and states that the Fourier transform of the projection and the line through the origin, tilted by θ , of the object function in Fourier space are identical. Mathematically, this means:

$$\tilde{P}_\theta(\omega) = \tilde{f}(\omega \cos \theta, \omega \sin \theta). \quad (2.45)$$

The theorem is presented schematically in Fig. 2.12. A function is generally available from its Fourier counterpart by an inverse Fourier transform. In this context, the object function $f(x, y)$ can hence be determined from the inverse Fourier transform of $\tilde{f}(u, v)$:

$$f(x, y) = \iint \tilde{f}(u, v) e^{i2\pi(ux+vy)} \, du dv. \quad (2.46)$$

Keeping in mind that the Fourier transform $\tilde{f}(u, v)$ is related to the projections of the object function $\mathcal{P}_\theta(t)$ —via the Fourier slice theorem—the object function $f(x, y)$ can be determined from projections over the angles θ covering a range of π . This operation of reconstructing a function from its projections is called an inverse Radon transform. In reality however, only a finite set of projection angles and a finite set of ray paths, due to the finite size of the imaging detector pixels, is available. This translates into a discrete representation of the Fourier transform in polar coordinates. The task of image reconstruction is then to transform the set of discrete Fourier components, which are given in polar coordinates, into a real space representation in cartesian coordinates. There are several ways to do this and here only the backprojection of filtered projections, usually referred to as *filtered backprojection (FBP)*, shall be described.

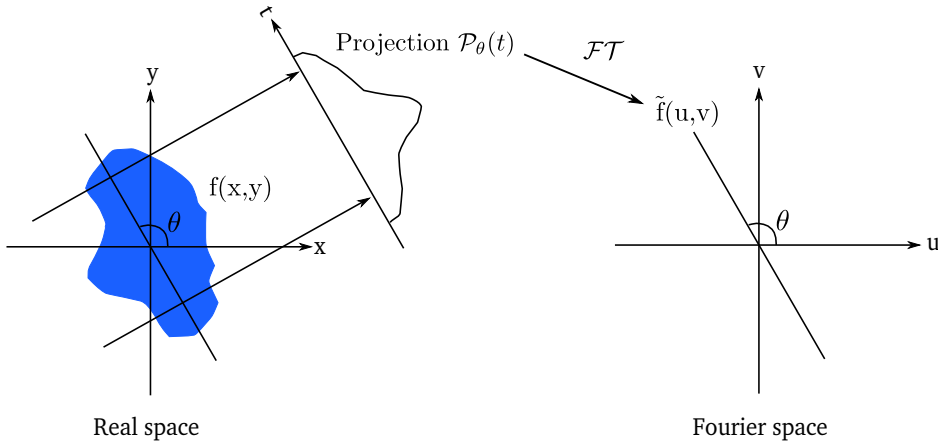


Figure 2.12: Fourier slice theorem. The projection of a distribution $f(x, y)$ onto a line, tilted by an angle θ , yields $\mathcal{P}_\theta(t)$. The Fourier transform of this projection is equal to a line, at angle θ , through the object function in Fourier space. This figure was adapted from Kak and Slaney (1987).

Filtered backprojection: The inverse Fourier transform (Eq. 2.46) can be reformulated in polar coordinates, using $t = x \cos \theta + y \sin \theta$, to read:

$$f(x, y) = \int_0^\pi \int_{-\infty}^{\infty} |\omega| P_\theta(\omega) e^{i2\pi\omega t} d\omega d\theta, \quad (2.47)$$

with $|\omega|$ mathematically being the Jacobian for the change of coordinate systems. Usually, this term is referred to as filter as it accounts for the fact that pixels near the rotation axis are much closer sampled than those at the edge. The Fourier filter compensates for this by the normalization with $|\omega|$. To distinguish between the backprojection and the filtering part, the formulation of Eq. 2.47 can be rearranged to read:

$$f(x, y) = \int_0^\pi \mathcal{FT}^{-1} \{F(\omega) P_\theta(\omega)\} d\theta, \quad (2.48)$$

with $F(\omega)$ denoting the filter function.

Cone-beam geometry: In the case of a divergent X-ray beam, the opening angles along and orthogonal to the tomography axis have to be taken into account in the reconstruction routine to avoid the occurrence of artifacts. A treatment of cone-beam reconstruction would, however, extend the scope of this thesis and here only the algorithm that is used within this work, the Feldkamp algorithm (Feldkamp et al., 1984), shall be mentioned. This

algorithm accounts for the different geometric dependencies of voxels in the reconstructed volume to pixels in the measured projections. Due to the beam divergence, this implies that several rows of detector pixels have to be considered for the reconstruction of a single volume slice.

To reconstruct the data that was acquired with the developed small-animal CT scanner, opening angles of up to 8 degree were present, and the Feldkamp algorithm was used. For the synchrotron-radiation-based experiments, parallel-beam reconstruction was applied.

The following considerations about quantitative CT reconstruction of the trimodal contrast projections apply to both the Feldkamp and the standard parallel-beam filtered backprojection.

2.4.2 Reconstruction of trimodal tomographic slices

Transmission projections: As introduced in section 2.3.3, the transmission projection is extracted from the phase-stepping curve by $T(p_x, p_y) = \frac{a_0^s(p_x, p_y)}{a_0^r(p_x, p_y)}$. In a rotated coordinate system (x', y') , with rotation angle θ , the transmission projection can be written as:

$$T_\theta(x') = \exp \left[- \int_0^d \mu(x', y') dy' \right], \quad (2.49)$$

with d denoting the thickness of the sample in X-ray propagation direction y' . This geometry is sketched in Fig. 2.13. Eq. 2.49 means in words, that the line integral—along the X-ray propagation direction y' —of the linear attenuation coefficient is contained in the transmission projection. In order to apply the backprojection formalism of Eq. 2.48, and to access $\mu(x', y')$, the Fourier transform of the negative logarithm needs to be taken first:

$$\tilde{\tau}_\theta(\omega) = \mathcal{FT} \{ -\ln [T_\theta(x')] \}. \quad (2.50)$$

The spatial distribution of the linear attenuation coefficient can then be reconstructed by:

$$\mu(x, y) = \int_0^\pi \mathcal{FT}^{-1} \{ F(\omega) \tilde{\tau}_\theta(\omega) \} d\theta, \quad (2.51)$$

with the filter function $F(\omega) = |\omega|$.

Differential phase projections: The refraction angle is determined from the phase-stepping curve by:

$$\alpha(p_x, p_y) = \frac{p_2}{2\pi d} \phi(p_x, p_y), \quad (2.52)$$

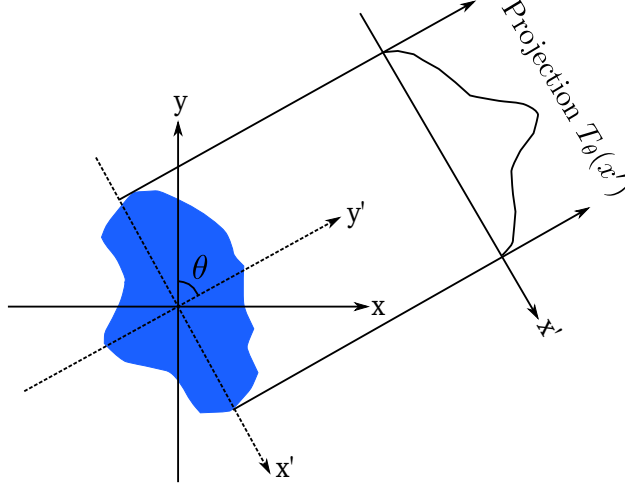


Figure 2.13: Rotated coordinate system for CT reconstruction. (x', y') is rotated by an angle θ with respect to (x, y) .

as introduced in Eq. 2.32. Using Eq. 2.9 and rearranging it for a rotated coordinate system, with tilt angle θ and coordinates (x', y') , we obtain:

$$\alpha_{\theta}(x') = \frac{\lambda}{2\pi} \frac{\partial \Phi_{\theta}(x')}{\partial x'} = \int_0^d \frac{\partial \delta(x', y')}{\partial x'} dy'. \quad (2.53)$$

Please note that $\Phi_{\theta}(x')$ denotes the total relative phase shift of the X-ray wave front acquired during the propagation in direction y' through the sample of thickness d :

$$\Phi_{\theta}(x') = \frac{2\pi}{\lambda} \int_0^d \delta(x', y') dy'. \quad (2.54)$$

$\phi(x, y)$ on the other hand denotes the phase of the phase-stepping curve as introduced in Eq. 2.32.

For the tomographic reconstruction, the Fourier transform of the refraction angles needs to be taken: $\tilde{\alpha}_{\theta}(\omega) = \mathcal{FT} \{ \alpha_{\theta}(x') \}$. Applying the backprojection formalism results in:

$$\delta(x, y) = \int_0^{\pi} \mathcal{FT}^{-1} \{ H(\omega) \tilde{\alpha}_{\theta}(\omega) \} d\theta. \quad (2.55)$$

The filter function for the case of differential phase projections is the so-called imaginary *Hilbert filter* with $H(\omega) = i \cdot \text{sgn}(\omega) / 2\pi$ (Pfeiffer et al., 2007b), with sgn being the sign function. The imaginary Hilbert filter essentially performs an integration in Fourier space to account for the differential nature of the phase projections.

Angular sensitivity in fan-beam geometry: In a fan-beam geometry setup, the angular sensitivity depends on the relative position of sample and phase grating due to a geometrical effect. This sensitivity dependence has to be accounted for by re-normalizing the reconstructed δ values with a factor of r_1/l , with r_1 being the source-to-sample and l the source-to-G1 distance. For further details, the reader is referred to the study by Engelhardt et al. (2007) and by Donath et al. (2009).

Dark-field projections: The scatter-induced dark-field image is determined on the basis of the ratio of the visibility of the phase-stepping curve with and without the sample: $DF(p_x, p_y) = \frac{\tilde{V}^s(p_x, p_y)}{V^r(p_x, p_y)}$. As before, if we consider a tilted coordinate system with tilt angle θ and coordinates (x', y') , the dark-field projection image can be denoted as $V_\theta(x')$.

Following the derivation by Bech et al. (2010), this visibility-based contrast can be described by (ultra) small-angle scattering, which results in a beam spread that is not resolved by the interferometer. This spread can be associated with a material specific *linear diffusion coefficient* ϵ in analogy to the linear attenuation coefficient μ . The measured projection is then given by (Bech et al., 2010):

$$V_\theta(x') = \exp \left[-\frac{2\pi^2 d^2}{p_2^2} \int_0^d \epsilon(x', y') dy' \right], \quad (2.56)$$

with p_2 denoting the period of the analyzer grating and d being the inter-grating distance of the phase- and analyzer grating.

For the tomographic reconstruction of $\epsilon(x, y)$, the same filter function $F(\omega) = |\omega|$ and Fourier transform of the negative logarithm $\tilde{\mathcal{V}}_\theta(\omega) = \mathcal{FT} \{-\ln V_\theta(x')\}$ is required:

$$\epsilon(x, y) = \frac{p_2^2}{2\pi^2 d^2} \int_0^\pi \mathcal{FT}^{-1} \left\{ F(\omega) \tilde{\mathcal{V}}_\theta(\omega) \right\} d\theta. \quad (2.57)$$

2.5 Effective energy of polychromatic X-ray spectrum

As we have seen in the previous section, CT reconstructions are quantitative in the sense that the sample's linear attenuation coefficient μ , decrement of the refractive index δ , and linear diffusion coefficient ϵ can be determined. This circumstance can be exploited to determine the effective energy in a grating-based interferometer, which is operated with a polychromatic X-ray

source. In general, there are several effects, which determine the effective energy of one particular experimental setup, these are:

- Emitted spectrum of the X-ray source.
- This spectrum is filtered (hardened) by the sample, by support structures (wafers) on which the grating structures are grown, and by the grating bars themselves.
- The efficiency of the gratings depend on energy, which additionally weights the filtered X-ray spectrum.

A determination of the effective energy is hence not straightforward, and—because of the energy-dependent grating efficiency—the effective energy can be different for different contrast modes. The knowledge of the effective energy is of significance as it considerably determines the imaging performance of the interferometer, i.e. the performance is optimal when the effective energy coincides with the design energy of the interferometer.

The principle idea for the determination of the effective energy is based on a comparison of the measured and calculated complex refractive index of a well-defined sample. The theoretical data can be calculated for the case that the sample is well-defined, and its exact elemental composition is known. The corresponding quantitative values for μ and δ can be calculated on the basis of tabulated data and the following equations for substances, that are made up of several elements.

Linear attenuation coefficient: For compounds or mixtures, the total attenuation coefficient of a substance s with density ρ_s is given by:

$$\mu_s = (\mu/\rho)_s \cdot \rho_s. \quad (2.58)$$

The mass attenuation coefficient of a substance consisting of several chemical elements i is given by

$$\left(\frac{\mu}{\rho}\right)_s = \sum_i \left(\frac{\mu}{\rho}\right)_i \cdot w_i, \quad (2.59)$$

where w_i is the weight fraction of the i -th element. The elemental mass attenuation coefficients in Eq. 2.59 can be obtained from tabulated data, for example from the online program XCOM operated by the National Institute of Standards and Technology (NIST, Gaithersburg, USA)¹.

¹<http://physics.nist.gov/PhysRefData/Xcom/Text/intro.html>

Refractive index decrement: For substances of density ρ_s consisting of several elemental constituents i , the total refractive index decrement can be determined according to (James, 1962; Herzen et al., 2009):

$$\delta_s = \frac{r_e \lambda^2}{2\pi} \cdot \rho_s \sum_i \frac{w_i N_A}{A_i} \cdot Z_i, \quad (2.60)$$

with the elemental weight fraction w_i , classical electron radius r_e , Avogadro's Number N_A , atomic mass A_i and total number of electrons Z_i . Please note that here the assumption was made, that the X-ray energies are considerably far from absorption edges as the real part of the atomic scattering factor is approximated by the total number of electrons in the atom.

To determine the effective energy, the following procedure is performed—measured (calculated) quantities are indicated by subscript m (c).

- A phantom with well defined and known elemental composition, for example water, is CT scanned and reconstructed quantitatively.
- To increase accuracy, μ_m and δ_m are determined from the mean value in a region-of-interest.
- Theoretical values for μ_c and δ_c are calculated on the basis of Eq. 2.59, Eq. 2.60, and the substance's density.
- The energy, for which μ_m and μ_c agree, is identified. This is the effective energy E_μ .
- The energy, for which δ_m and δ_c agree, is identified. This is the effective energy E_δ .

This energy calibration routine is used to determine the effective energy for the developed stationary-gantry prototype and for the rotating-gantry CT scanner in sections 4.4.1 and 4.5.3.

2.6 Production of gratings

The exact technical requirements on the x-ray optical gratings depend on the characteristics of the corresponding imaging setup. Typically, grating bars with a spacing of few micrometer and height of many tens of micrometer are required. The fact that the area of the gratings limit the available field-of-view (FOV), translates into requirements on the grating area. Any

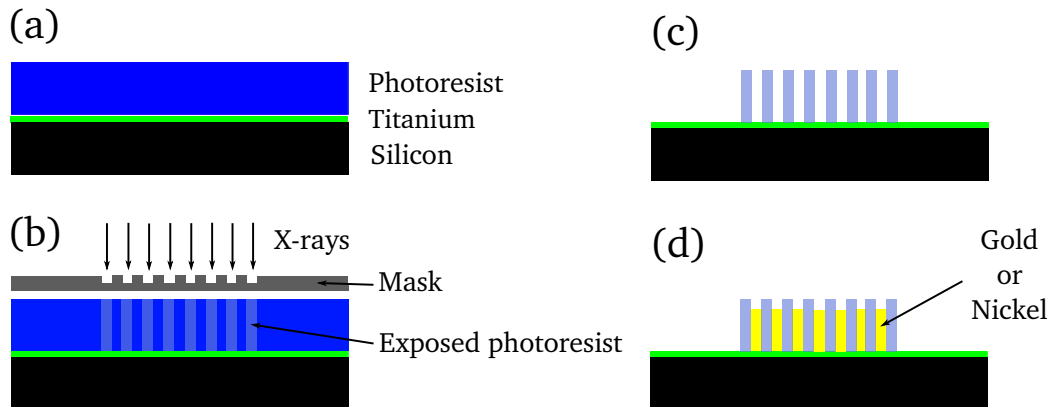


Figure 2.14: Production of gratings with the LIGA process. (a) A silicon wafer is sputtered with titanium and then spin-coated with a negative photoresist. (b) Using a mask, the photoresist is exposed with X-rays in the shown pattern. (c) The unexposed areas are removed in the development step. (d) The grating bars are grown from the titanium layer using electroplating of gold or nickel.

deviation from the ideally required box-shape of the grating bars and any irregularity of bar alignment over the entire grating area, causes distortions in the final X-ray image and grating production accuracy needs to meet very high standards for these reasons.

Nowadays, there are different technological processes for the production of the grating structures. Most of these include one or several of the following steps: photolithography, anisotropic wet etching, and electroplating. The majority of gratings that were utilized in the imaging setups within this thesis, were produced with the so-called *LIGA process* (Reznikova et al., 2008; Kenntner et al., 2010, 2012; Mohr et al., 2012). This process involves X-ray lithography and electroplating and is described briefly. A sketch of the production steps is shown in Fig. 2.14: (a) First, a silicon wafer is sputtered with an electro-conductive layer of titanium (or gold) and then spin-coated with a negative photoresist. (b) This photoresist is exposed with synchrotron X-rays in combination with an absorbing mask. This mask was generated using electron beam writing. (c) The unexposed photoresist is removed in the development process. (d) Finally, the grating bars are grown from the titanium layer using electroplating of gold (nickel) for an absorption (phase) grating. As an example, an analyzer grating, which was produced employing the LIGA process, is shown in Fig. 2.15: (a) scanning electron microscope image, (b) photograph of the grating structure. This particular grating is

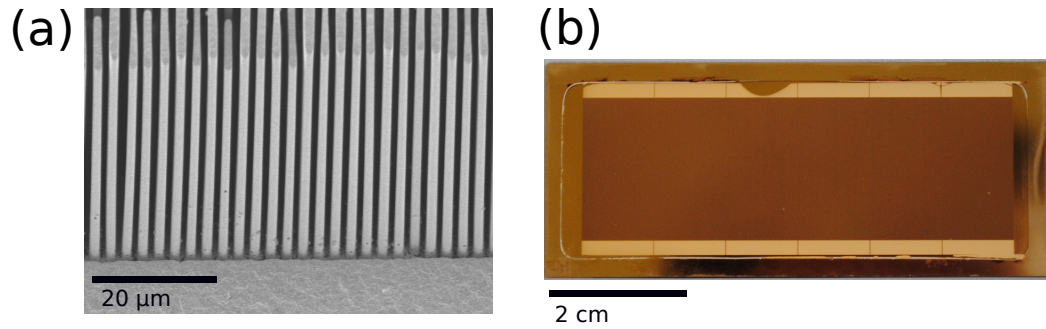


Figure 2.15: Absorption grating produced using the LIGA process. (a) Scanning electron microscope image. (b) Photograph of the entire grating structure that covers an area of $20 \times 60 \text{ mm}^2$. This figure was previously published in Tapfer et al. (2011).

used in the stationary-gantry prototype, which was developed within this thesis. Technologically, grating production is extraordinarily challenging for several reasons. First and foremost, the very high aspect ratio of absorption gratings—of up to 80 in some cases—is extremely demanding. Moreover, it is challenging to fabricate membrane masks, which are required in the lithographic step, with a large area without distortions. Furthermore, the avoidance of mechanical stress, which is very important to avoid bending and other large-scale distortions of the grating bars, requires highly optimized processes. Also the electroplating step needs to be highly fine-tuned to guarantee a certain uniformity of bar height.

The gratings, which were used in this work were predominantly produced by the Institute of Microstructure Technology of the Karlsruhe Institute of Technology (Karlsruhe, Germany) and by the company microworks (Karlsruhe, Germany). For both, grating area is—with the current processes—limited to approximately 10 cm in diameter.

Chapter 3

Imaging of mouse models of cancer

In this chapter, the potential of grating-based phase-contrast CT imaging for the investigation of mouse models of cancer is assessed. Two different phase-contrast imaging setups, one operated with synchrotron radiation and one operated with a conventional tube source, are used in this context. For comparison with the X-ray data, for some of the mice, magnetic resonance imaging, a cryotome-based optical imaging technique and conventional histology were performed additionally. In total, three different models were investigated and the chapter is structured accordingly. The main results of this chapter have been published in Tapfer et al., X-ray Phase-Contrast CT of a Pancreatic Ductal Adenocarcinoma Mouse Model, PLoS One (2013). The research on small-animal disease models was supported by the DFG Cluster of Excellence ‘Munich-Centre for Advanced Photonics’ (MAP).

3.1 Motivation

As we have seen in the previous chapter, grating interferometry can be used with both synchrotron radiation sources and conventional tube sources. In the last years, numerous studies in both setup configurations have shown excellent imaging results with respect to soft-tissue contrast¹. Fundamentally, this observed increased soft-tissue contrast is the driving force for exploring the potential of the technique for the study of mouse models of cancer.

¹(Momose et al., 2006; Pfeiffer et al., 2007a; Weitkamp et al., 2008; Bech et al., 2009; Donath et al., 2010; Schulz et al., 2010; Castelli et al., 2011; Stampanoni et al., 2011; Stutman et al., 2011; Sztrókay et al., 2012; Hoshino et al., 2012; Schleede et al., 2012; Tapfer et al., 2013)

At the present state of technology, the study of small specimen features a few advantages over the study of larger-sized samples. With respect to biomedical whole-body imaging, this renders small-animal preclinical research interesting. The main limitation for specimen size in this context relates to the production of adequate gratings. Presently, the area of the gratings is, without considerable effort for stitching, limited to approximately 10 cm in diameter when using X-ray lithographic processes (see 2.6) for grating production. As this area naturally limits the FOV, imaging of small animals is convenient: the torso of a mouse for example is approximately 3 cm in diameter and 6 cm in length. A second aspect relates to the volume of the specimen. In order to ensure sufficient transmission of X-rays through the body of a small animal, typical X-ray energies are in the range of 20–30 keV, as opposed to typical mean energies of 70–90 keV in human CT scanners. In terms of grating properties, this lower X-ray energy translates to lower requirements on the height of the absorbing grating bars. In practice, this means that gratings for small animal imaging are presently available, unlike gratings for whole-body human imaging. Besides these technological advantages, there is a further aspect that relates to the imaging method itself. It has been reported in the literature that small detector pixel sizes are beneficial for the signal-to-noise ratio (SNR) in phase images (Engel et al., 2011; Köhler et al., 2011; Chen et al., 2011). Essentially, this circumstance is due to the fact that the measured phase projections are of differential nature. Typical detector pixel sizes in small animal imaging are on the order of few tens of micrometer, as opposed to several hundreds of micrometer in typical human CT scanners.

For small-animal research as such, histopathology is—in most cases—still the gold standard technique for examining the tissue of interest. This technique is intrinsically 2D, and can only be extended to 3D by virtually stacking subsequent slices (Weninger et al., 1998). In general, histopathology is a very labour-intensive technique (depending on the needed through-plane resolution) and is not well suited for screening of large volumes as required for example in anatomical phenotyping or therapeutic response monitoring. To this end, for 3D imaging of whole small animals, most commonly micro-computed tomography (micro-CT) and magnetic resonance imaging are used (Tyszka et al., 2005; Cnudde et al., 2008). A technical description of MRI would extend the scope of this thesis and at this point only the key characteristics with respect to imaging are briefly mentioned. MRI is a 3D imaging technique, which makes use of the property of *nuclear magnetic resonance* to image the spatial distribution of atomic nuclei inside the object. As biomedical imaging technique, it exhibits excellent intrinsic soft-tissue contrast due to differing T1 recovery and T2 decay times. However, the technique is

fundamentally limited in spatial resolution due to molecular diffusion, T2 relaxation, and magnetic field inhomogeneities. For further details, the reader is referred to textbooks, for example ‘Principles of Nuclear Magnetic Resonance Microscopy’ by Callaghan (1993).

Micro-CT on the one hand features high spatial resolution (on the order of several micrometers), but has difficulty in distinguishing different types of soft tissues (Holdsworth and Thornton, 2002). This limitation can partly be overcome by the injection of a contrast agent, resulting in soft-tissue contrast based on differences in agent uptake and washout dynamics. As mentioned, MRI on the other hand shows high intrinsic soft-tissue contrast, but is fundamentally limited in spatial resolution (Tyszka et al., 2005). In the field of small-animal research, phase-contrast imaging hence combines the advantages of 3D volume information at high spatial resolution with high soft-tissue contrast.

In summary, small-animal phase-contrast imaging—as a model for human imaging—exploits technological advantages, and—in the field of small-animal research—has the potential to complement available imaging technology.

3.2 Outline

In light of these considerations, the present chapter is devoted to the assessment of the potential of grating-based phase-contrast CT for studying mouse tumor models. For this purpose, different mouse models were studied ex-vivo, using different imaging setups. Phase-contrast imaging was conducted at two distinctly different imaging setups: one using synchrotron radiation and the other using a conventional tube source. In general, two different types of potential applications of phase-contrast CT were investigated using these settings: firstly, high-performance imaging for benchmarking and secondly, dose-reduced imaging to assess the potential for in-vivo imaging. More precisely, in-vivo imaging was not performed, but imaging was performed under dose conditions, which are compatible with in-vivo imaging. In this sense, the obtained data can be analyzed in view of future in-vivo applications. For comparison with the X-ray images, the following imaging modalities were also used for some of the mice: magnetic resonance imaging, cryotome-based pseudo-3D optical imaging, and conventional histology.

The structure of this chapter follows a division by mouse model and specifically, the following mice specimen and imaging settings were studied:

- Healthy mouse (section 3.4): synchrotron-based X-ray imaging and pseudo-3D optical imaging. The data of this mouse was analyzed gen-

erally with respect to the visibility of anatomy in the abdomen and quantitatively (using signal-to-noise ratios) for selected organs.

- Mouse model of pancreatic cancer (section 3.5): synchrotron-based and tube-based X-ray imaging. For comparison: MRI and histology. This data was analyzed with respect to the visibility of lesions and solid tumor mass.
- Colon carcinoma-bearing mouse (section 3.6): synchrotron-based X-ray imaging. Images of two specific organs were analyzed in depth: the liver and the cerebellum.

Before the imaging data of the different mice are presented, first, the two phase-contrast imaging setups are introduced (section 3.3). At the end, the main results are summarized (section 3.7).

3.3 Description of X-ray phase-contrast imaging setups

In section 2.2, X-ray tubes and synchrotron radiation were introduced as sources of X-rays. Due to the differences in X-ray properties, there are, in general, two different types of grating-based phase-contrast imaging setups: the one operated with synchrotron radiation and the one operated with a tube source.

Because of the drastically higher flux of a synchrotron source, the X-rays can be monochromatized and still provide significantly higher flux than conventional (polychromatically operated) tube sources. Monochromaticity increases image quality due to two effects: the performance of the interferometer reaches its maximum, given that X-ray energy and interferometer design energy match, and image contrast is not ‘washed out’ due to the energy dependence of the linear attenuation coefficient μ and decrement of the refractive index δ . Moreover, due to the larger flux, statistical image noise is reduced. Image quality is hence superior at a synchrotron-radiation-based setup and it is ideally suited for benchmarking imaging.

The huge and crucial advantages of tube sources simply are their availability and straightforwardness of use. For synchrotron-based experiments a tremendous technological and organizational effort has to be undergone and routine imaging at a local site is, as a matter of fact, only possible when using tube sources. This is in particular relevant when regarding the intended translation of the technique towards clinical applications.

	Energy	p_0 [μm]	p_1 [μm]	p_2 [μm]	Pixel size [μm]	d [mm]	TO
Synch.	35 keV	–	4.79	2.40	30	408	5
Tube	23 keV	10.0	3.51	5.40	120	527	3

Table 3.1: Interferometer characteristics. The X-ray energy, grating periods (source grating p_0 , phase grating p_1 , analyzer grating p_2), effective pixel size, inter-grating distance d (between G1 and G2) and corresponding fractional Talbot order (TO) are listed. The quoted X-ray energy of 23 keV for the tube source specifies the center of the polychromatic spectrum.

3.3.1 Synchrotron radiation source

The synchrotron-radiation-based setup that was used in this thesis is installed at beamline ID 19 of the European Synchrotron Radiation Facility (ESRF) in Grenoble, France. Fig. 3.1 shows a sketch (a) and photograph (b) of the imaging setup. The distance between the wiggler/undulator source and the imaging station is approximately 150 m, which results in a large beam size with a high degree of transverse coherence, meaning that no source grating has to be used and the interferometer is of Talbot type. The available X-rays energies, which can be monochromatized by a Si (111) double-crystal monochromator, range from 7 to 100 keV.

The maximum available beam size is $40 \times 15 \text{ mm}^2$ (width \times height), with the 15 mm corresponding to the direction along the tomography axis. This size hence also limits the ‘length’ of mouse that can be imaged at once. The 40 mm across are sufficient to cover a mouse in width. In order to cover the full abdomen of a mouse, consecutive CT scans were merged. For all performed imaging experiments, an energy of 35 keV and a π -shifting phase grating were used. Further details about the interferometer, such as periods of the gratings, inter-grating distance and Talbot order are listed in Tab. 3.1 (top row). Due to the large distance between the source and the imaging station, parallel-beam reconstruction can be used. For acquiring the phase-stepping curve, the phase grating was stepped using a commercial piezo translation stage (HERA model series, Physik Instrumente PI, Karlsruhe, Germany). The imaging detector at the beamline is a scintillator/lens-coupled CCD detector (FReLoN), which can be operated with different optics, resulting in different effective pixel sizes. In the performed experiments, a pixel size of $30 \times 30 \mu\text{m}^2$ was used. Further details about the beamline and technical developments of the interferometer can be found in the PhD thesis of Zanette (2011) and in Weitkamp et al. (2010).

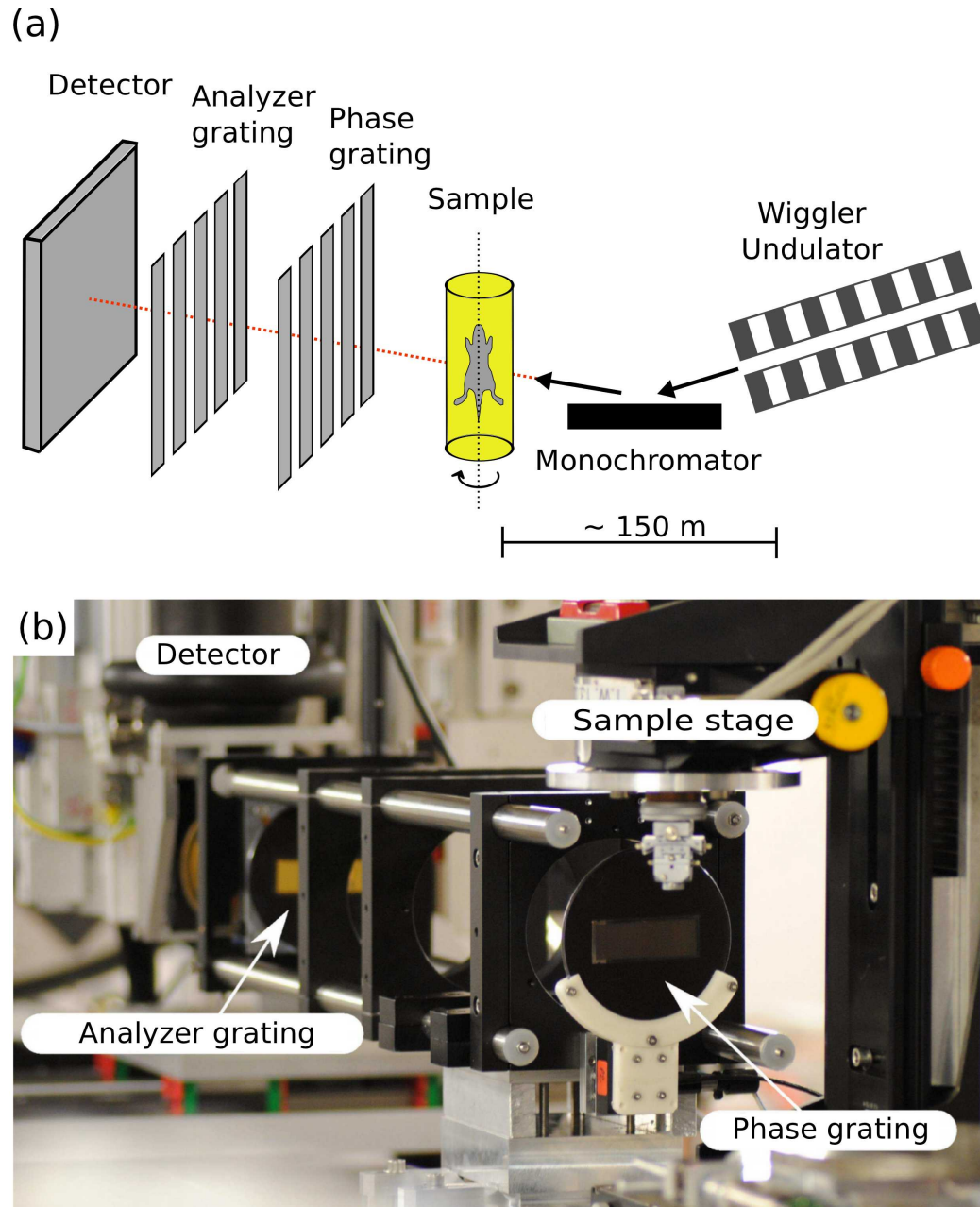


Figure 3.1: Imaging setup at beamline ID 19 of the ESRF. X-rays are produced by a wiggler/undulator source approximately 150 m downstream of the imaging station and are monochromatized by a Si (111) double crystal. (a) Sketch of the beamline with two-grating Talbot interferometer. (b) Photograph of the interferometer with labelled components. This picture was adapted from the PhD thesis of Zanette (2011).

3.3.2 Tube source

The tube-based bench-top imaging setup, which was used in this thesis, is installed at the Physics Department of the Technische Universität München (Munich, Germany). Fig. 3.2 shows a sketch (top) and photograph (bottom) of the imaging setup. The setup length is approximately 2 m and the components are installed on an optical bench. X-rays are generated by a rotating anode tube (Enraf Nonius FR 591, molybdenum target) with an effective focal spot size of $0.3 \times 0.3 \text{ mm}^2$. Transverse coherence is hence not sufficient and a source grating has to be used, meaning that the interferometer is of Talbot-Lau type. The distances between the emission point of the source, source grating (G0), phase grating (G1), and analyzer grating (G2) are the following: $d(\text{source-G0}) = 420 \text{ mm}$, $d(\text{G0-G1}) = 976 \text{ mm}$, $d(\text{G1,G2}) = 527 \text{ mm}$. The silicon wafer of each grating has a thickness of $500 \text{ }\mu\text{m}$, which acts as a filter on the otherwise unfiltered X-ray energy spectrum of the molybdenum target. For the performed experiments, the tube acceleration voltage was set to 35 kVp, which results in an X-ray spectrum that is centered around the interferometer design energy of 23 keV. The phase grating induces a $\pi/2$ shift. As for the synchrotron-based setup, further interferometer characteristics are listed in the bottom row of Tab. 3.1. Due to the small X-ray beam divergence, the half-opening angle is approximately 1 degree, parallel-beam reconstruction can be used. The imaging detector is a *Pilatus II* (Dectris, Baden, Switzerland), silicon-based photon-counting detector. It features a physical pixel size of $172 \times 172 \text{ }\mu\text{m}^2$, which, accounting for geometrical magnification, results in an effective pixel size of $120 \times 120 \text{ }\mu\text{m}^2$.

3.4 Imaging of a healthy mouse

3.4.1 Introduction

As a start and to give a general overview of the potential of phase-contrast CT for small-animal imaging, one healthy mouse specimen was studied. In this context, the abdomen is of most interest as it contains various soft-tissue organs. Imaging thereof was performed using high-performance synchrotron-radiation-based phase-contrast CT and, for comparison, using a pseudo-3D slicing-based optical technique. In order to avoid deformations and to minimize distortions in the longitudinal direction, the latter technique was performed at a cryotome, i.e. an optical camera took images of each cutting surface of the frozen specimen during the sectioning process. Subsequently, these images were aligned and stacked to a pseudo-3D volume. A similar approach was performed in the studies by Wilson et al. (2008) and Steyer

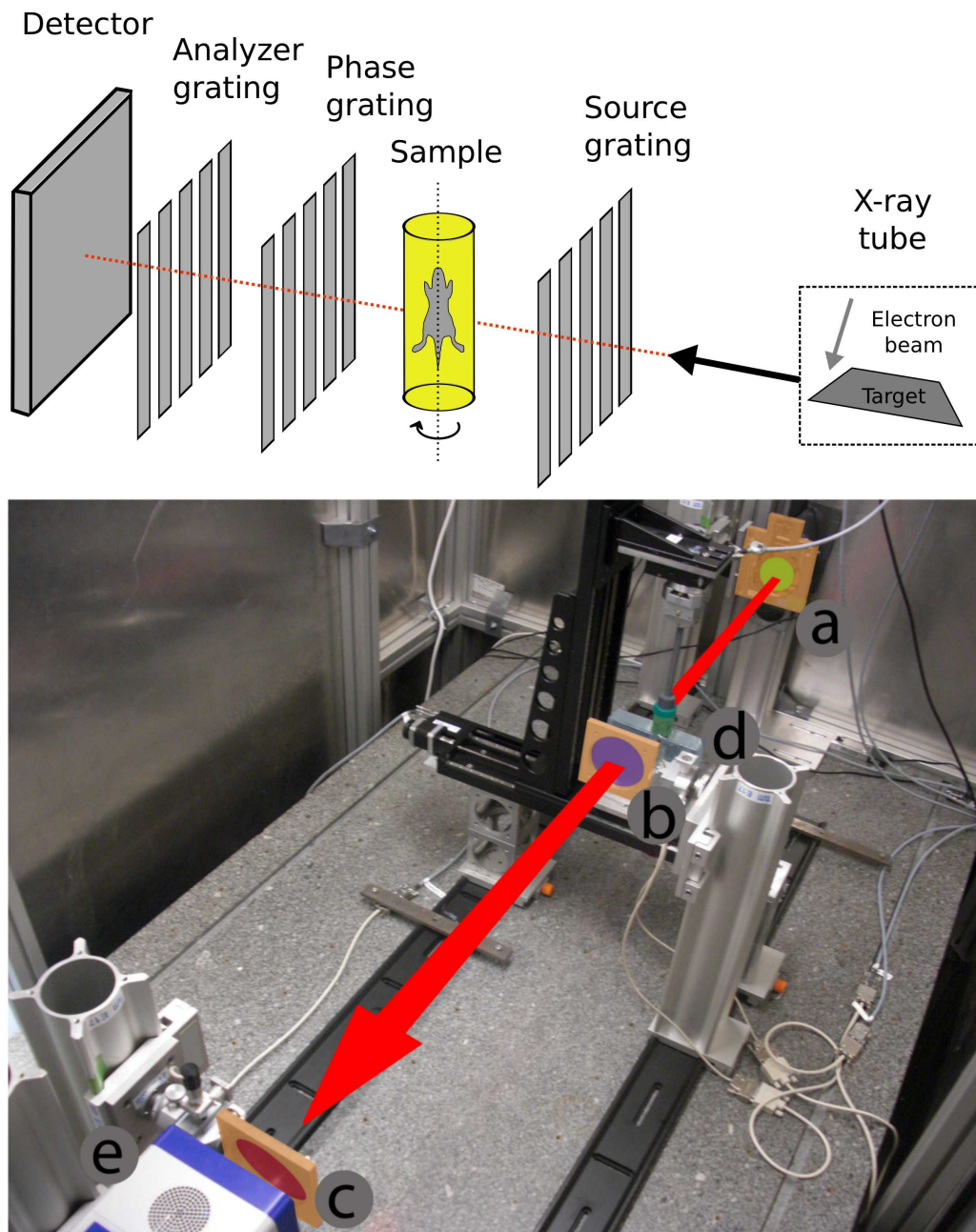


Figure 3.2: Tube-based imaging setup at the Physics Department of the Technische Universität München. (Top) Sketch of the imaging setup and the three-grating Talbot-Lau interferometer. (Bottom) Photograph of the setup, with the following labelled components: (a) source grating, (b) phase grating, (c) analyzer grating, (d) sample, (e) imaging detector. The photograph was kindly provided by A. Hipp (Technische Universität München).

et al. (2009). In the following, this technique is referred to as cryo-imaging.

The phase-contrast CT and cryo-based images are compared visually with respect to the visibility of fine anatomical details. For the attenuation and phase images, additionally, a quantitative assessment (using signal-to-noise ratios) of specific organs was performed. At the end of the section, relevant properties and differences of both techniques are reviewed. Moreover, based on the experimental findings, phase-contrast CT is placed into context with other dedicated small-animal imaging methods.

3.4.2 Description of cryo-imaging setup

The imaging setup consists of a commercially available rotary cryotome (CM 1950, Leica Microsystems GmbH, Wetzlar, Germany), equipped with a near-infrared sensitive camera (Luca R, Andor Technology plc., Belfast, UK). Since the camera itself is monochromatic, in order to reconstruct the color image, a controllable filter-wheel, with an RGB filter-set in front of it, is used. Additional polarizers are used to minimize specular reflections from the ice crystals. Specially developed software controls the sectioning procedure of the cryotome and the image acquisition of the optical system. Essentially, the technique is based on color images taken directly from the cutting surface of the frozen specimen (episcopic images) during the sectioning process. Fig. 3.3 displays the cryo-imaging setup schematically. The generation of a pseudo-3D volume is based on the relative alignment of all images with the help of fiducial makers and subsequent virtual stacking. The sample preparations (embedding and freezing) and data acquisition time (slicing and image capture) for the mouse specimen was approximately 15 hrs in order to achieve whole body, high through-plane resolution. The pixel size in-plane was $25 \times 25 \mu\text{m}^2$, and the slice thickness was approximately $100 \mu\text{m}$. By pausing the slicing procedure, the cryotome can also be used for collecting samples for conventional histopathology. The system is moreover specially designed for multi-spectral imaging the bio-distribution of fluorescent probes. This feature was, however, not used in the present study as the injection of fluorescent markers requires a living animal. A detailed description of this cryo-imaging system can be found in Sarantopoulos et al. (2011).

3.4.3 Imaging parameters and data analysis

The X-ray phase-contrast CT scan was performed at the synchrotron setup, which was introduced earlier. For the tomography, 901 projections were acquired over 360 degrees. In the phase-stepping procedure, four images were

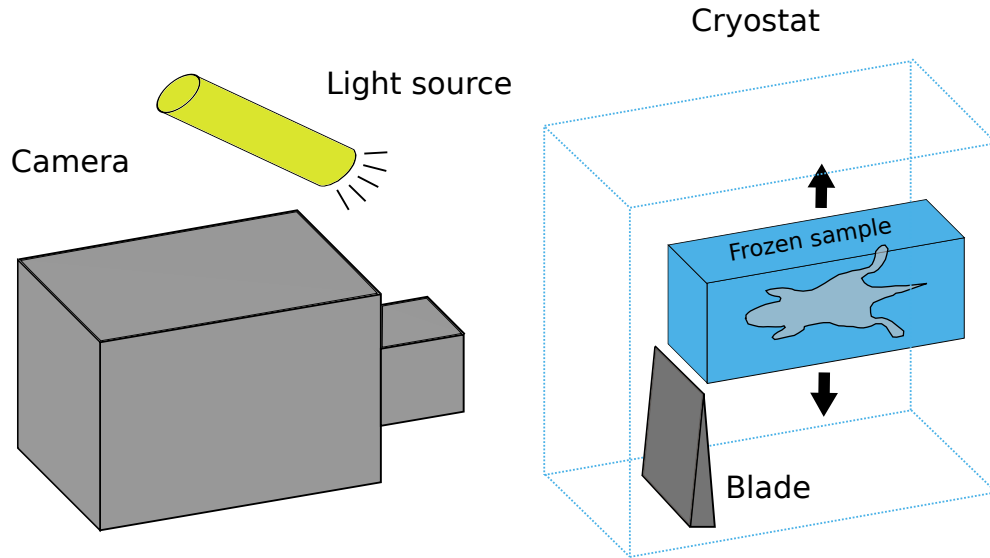


Figure 3.3: Schematic representation of the cryo-imaging setup. A camera takes images of each cutting surface of the frozen specimen during the sectioning process. Subsequently, images are aligned and stacked to a pseudo-3D volume.

acquired with an exposure time of 1 s each. As the FOV is limited in the direction along the tomography axis to 2 cm, 2 consecutive CT scans were merged, resulting in a total acquisition time of approximately 4 hrs. The effective detector pixel size of $30 \times 30 \mu\text{m}^2$ resulted in an isometric CT volume voxel size of $30 \times 30 \times 30 \mu\text{m}^3$. After the CT scan, the mouse was frozen and imaged at the cryo-imaging setup.

The datasets of both techniques were aligned by applying rigid transformations by hand. Due to the nearly identical specimen positioning during X-ray acquisition and subsequent cryo-freezing of the entire mouse, misalignment of both data is minimal and sophisticated software registration as used for example by Müller et al. (2012) was not necessary. The comparison of visibility of different tissues for both methods is done by visual inspection. For the X-ray data, attenuation and phase images were additionally compared quantitatively. For the quantitative comparison of both images, regions of interest (ROI) within several organs were selected and the signal-to-noise ratio was determined. The required noise estimate in this analysis was determined from the standard deviation of a specific ROI that covers a region of homogeneous tissue. In this way, the effect of tissue heterogeneity is avoided and the standard deviation σ only reflects image noise. Based on the mean

value of the ROI of organ i , M_i , and the standard deviation σ , the SNR was calculated according to

$$\text{SNR}_i = \frac{M_i}{\sigma}. \quad (3.1)$$

The uncertainty of the SNR (σ_{SNR}) was determined by applying standard error propagation to the equation of the SNR (Eq. 3.1). The required uncertainties are the standard error (SE) of each mean value ($SE_{\text{mean}} = \frac{\sigma}{\sqrt{N}}$) and the standard error of the noise estimate ($SE_{\sigma} = \frac{\sigma}{\sqrt{2N}}$) (Press et al., 2007). N denotes the number of voxels in the corresponding ROI.

3.4.4 Imaging results

In Fig. 3.4, three transverse views of the abdomen are shown: (a) cryo-images, (b) phase images, (c) attenuation images. The transverse slice in the top row is located inferior to the lung, the middle row's slice covers both kidneys, and the bottom row is superior to the hip. Prominent organs that can clearly be identified are the stomach (s), several lobes of the liver (l), the kidney (k), and intestines (i). All of these are highlighted in the cryo-images. When comparing the cryo- and X-ray images, the good correlation becomes apparent. Only few slight deformations in shape are present. Moreover, please note that the apparent slice thickness of the cryo-images is larger as the light penetrates noticeably the surface. When regarding the cryo-images, all organs can be easily identified as expected. Here, the difference in color significantly improves discernibility of organs. Also in the phase image, all organs can be clearly identified. For the attenuation image, the recognizability of organs is markedly compromised. In particular, soft-tissue contrast is strongly reduced and only bone tissue generates a strong contrast. In order to objectify this visual impression, a signal-to-noise ratio analysis for the indicated ROIs (Fig. 3.4, red circles in column (b) and (c)) covering different organs was performed. Image noise was determined from the standard deviation in the ROIs labeled with an asterisk (blue circles). Tab. 3.2 lists the corresponding SNR values. These confirm the described visual impression, with approximately 7 times larger SNRs in the phase images.

Fig. 3.5 displays coronal slices of the cryo-volume (a), the phase- (b) and attenuation data (c). As before, good correlation between the cryo-image and the X-ray images is given. However, it becomes apparent that the cryo-based technique naturally performs worse in the longitudinal direction: horizontally oriented distortions are visible, which are caused by the virtual stacking. The X-ray data on the other hand is truly 3D and any slice orientation is accessible.

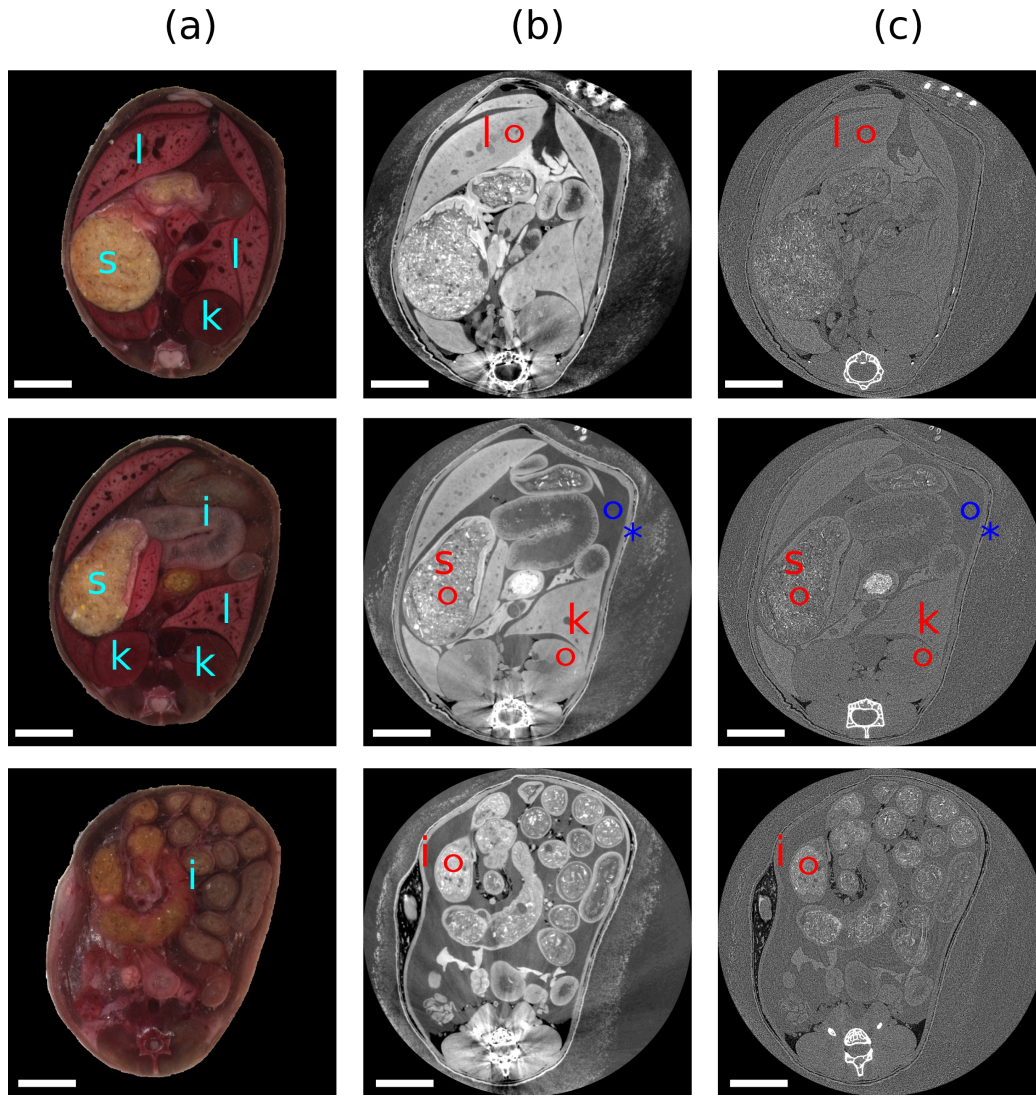


Figure 3.4: Transverse slices of all imaging modalities at three different positions: (a) cryo-images, (b) phase-contrast CT images, (c) attenuation CT images. Prominent organs are labeled: stomach (s), liver (l), kidney (k), intestine (i). The ROIs of the corresponding organs and the noise ROI (asterisk) for the SNR analysis are indicated. All images are displayed on a linear color scale and are windowed for best visual appearance. The scale bar indicates 5 mm.

SNR	Attenuation	Phase
Liver (l)	15.2 ± 0.3	107 ± 2
Stomach (s)	15.2 ± 0.3	108 ± 2
Kidney (k)	15.1 ± 0.3	107 ± 2
Intestine (i)	16.0 ± 0.3	117 ± 2

Table 3.2: Signal-to-noise ratios in attenuation and phase images for selected tissues are listed. The noise level was determined from the ROI labeled with an asterisk.

3.4.5 Discussion

Present preclinical research on small animals aims at fundamentally understanding various pathologies. Moreover, anatomical phenotyping is of great interest, especially due to the ever increasing access to genetically engineered animals. For these and potentially also other applications that require high spatial resolution 3D data with pronounced soft-tissue visibility, phase-contrast CT and cryo-imaging have shown great potential. In the following the advantages and limitations of both techniques are considered briefly.

Cryo-imaging, which is compatible with acquiring conventional histological sections, can be combined with staining for gene and protein expression. The experimental setup does moreover have the capability to image the bio-distribution of fluorescent probes, which allows for functional imaging. The technique is for these reasons very well suited as validation technique for novel non-destructive imaging modalities and has, for example, been used in combination with multispectral optoacoustic tomography and fluorescence

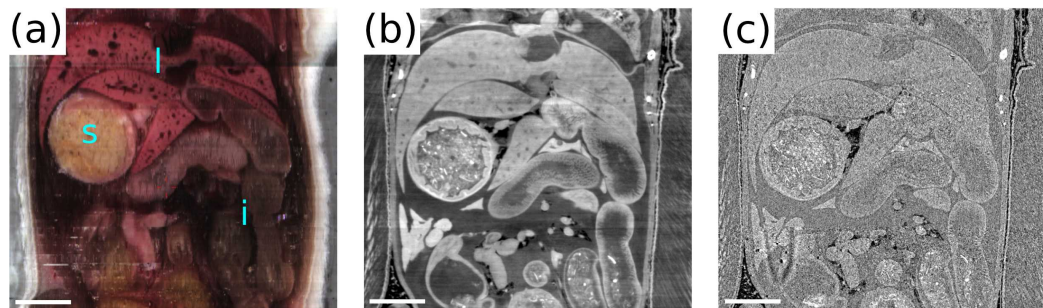


Figure 3.5: Coronal views of all imaging modalities: (a) cryo-image, (b) phase image, (c) attenuation image. The stomach (s), liver (l) and intestines (i) are labeled. All images are displayed on a linear color scale and are windowed for best visual appearance. The scale bar indicates 5 mm.

	Cryo-imaging	Phase-contrast CT
Pixel size [μm]		
in-plane	25	30
through-plane	75 - 125	30
Acquisition time [hrs]	≈ 15	≈ 4
Volume format	pseudo 3D	truly 3D
Sample handling	cryo-sectioning	fixation
Other features	histological staining fluores. bio-markers	2 image contrasts quantitative (μ and δ)

Table 3.3: Overview of properties of both reviewed modalities, cryo-imaging and phase-contrast CT.

molecular tomography (Ale et al., 2012; Herzog et al., 2012; Taruttis et al., 2013). The use of combinations of narrow-band filters can also further increase the contrast of intrinsic tissue chromophores, as hemoglobin. The range of applications is of course limited due to the destructive nature and the expense in labour involving sample preparation, the physical slicing, photographing and post-alignment. In case a 3D volume is generated, additional software post-processing is necessary and slight distortions in the longitudinal direction can hardly be avoided with the used setup. Using a different cryotome, the process can be fully automated, decreasing the workload and the user-dependend acquisition artifacts, like misalignments. The addition of xy-stages to scan the sample with a microscopic lens can further increase the resolution, by binning multiple images for each plane.

Tomographic imaging in general allows for a higher and more user-friendly throughput, is non-destructive and results in truly 3D data volumes, with isotropic spatial resolution in all three orthogonal directions. Also samples that are difficult to slice can be handled and the intrinsic digital nature of tomographic data allows for straightforward software post-processing like for example volume quantification or segmentation. Technically, a higher spatial resolution is easily achievable for both techniques by using different camera optics or a different X-ray detector respectively.

In the context of preclinical imaging, Tab. 3.3 summarizes the discussed properties and technical parameters of phase-contrast CT and cryo-imaging.

Other non-invasive imaging techniques with dedicated instruments for small animals besides magnetic resonance imaging include single-photon emission computed tomography (SPECT), positron emission tomography (PET), and several optical imaging techniques. Spatial resolution is strongly superior in

the emission techniques (SPECT and PET), and also MRI is fundamentally limited in spatial resolution (Callaghan, 1993). For optical techniques, the main limitation is penetration depth (Ntziachristos, 2010).

Here, grating-based phase-contrast CT offers the complementarity of two contrasts, combining high soft-tissue contrast with a good representation of the skeleton at high spatial resolution.

3.5 Imaging of a mouse model of pancreatic cancer

3.5.1 Introduction

After the previous general consideration of phase-contrast CT imaging of mice, the present section now assesses the potential of the technique for a specific pancreas mouse tumor model. The setting for this study is the following:

- On the one hand high-performance, high-dose, and high spatial resolution imaging for ‘virtual histology’ applications is investigated. This part is covered by a synchrotron radiation (SR) based benchmarking experiment at the ESRF. In order to clearly distinguish the different datasets, this dataset is referred to as *Synchrotron (high-performance)*.
- On the other hand, the capability of phase-contrast CT for in-vivo imaging with improved soft-tissue contrast is assessed with dose-reduced measurements of the same mouse specimen using synchrotron radiation and using the described tube source. These settings represent idealized preclinical imaging systems with the limitation that the specimen, rather than the CT gantry, was rotated. These two datasets are referred to as *Synchrotron (low-dose)* and *Tube source*.
- For all X-ray CT scans, radiation dose is measured with a dosimeter.
- Moreover, magnetic resonance imaging is performed on a clinical 1.5 Tesla MRI scanner using a dedicated microscopy coil. The MRI measurement serves as a reference technique with well-established high intrinsic soft-tissue contrast.
- Finally, as the gold standard technique for tissue classification, histology is obtained for a limited section of the mouse specimen.

	# Projections	# Phase steps	Exposure time [s]
Synchrotron			
high-performance	901	4	1
low-dose	301	3	0.04
Tube source	301	10	12

Table 3.4: X-ray CT data acquisition parameters for the different imaging settings.

The potential for both types of applications—high-performance CT for ‘virtual histology’ and dose-reduced phase-contrast CT for in-vivo imaging—is investigated on the basis of a qualitative and quantitative comparison of the visibility of tissue lesions in attenuation and phase images.

3.5.2 Tumor model and imaging parameters

Tumor model and histology: To model a pancreatic ductal adenocarcinoma (PDAC), the mouse was genetically engineered and, at an age of approximately 1.5 years, euthanized, perfusion-fixated and placed in a plastic container for imaging². For histology, the abdomen was cut off, dehydrated in an automated tissue processor and embedded in paraffin. After embedding, the spine was removed and the whole abdomen was cut into 4 μm thick serial sections. Afterwards, sections were stained with hematoxylin and eosin and digitized with a slide scanner (DotSlide, Olympus).

X-ray imaging parameters and data analysis: Tab. 3.4 lists the imaging parameters for the synchrotron- and tube-based acquisition. For the low-dose synchrotron data, the raw detector images were binned 4×4 , resulting in an effective isotropic voxel size of $120 \times 120 \times 120 \mu\text{m}^3$.

²Pancreas specific activation of oncogenic Kras was obtained by breeding *Ptf1a^{+ / Cre}* knock-in mice with *Kras^{+ / LSL-G12D}* animals (Hingorani et al., 2003). Before euthanizing, the *Ptf1a^{+ / Cre} Kras^{+ / LSL-G12D}* mouse was 19 months old and it was kept in isoflurane narcosis when a median laparotomy was performed, followed by a perfusion fixation protocol. In brief, the left ventricle was cannulated with a 22 G needle, followed by clipping of the right atrium. Then, 10 ml of phosphate buffered saline was manually infused to flush out all blood from the vasculature, followed by manual infusion of 20 ml 4% paraformaldehyde (PFA). Thereafter the animal was submerged for 72 hours in 200 ml 4% PFA, briefly washed in 70% ethanol and transferred into a 50 ml Falcon tube in 70% ethanol. Animal care and experimental protocols were conducted in accordance with German animal protection laws and approved by the Institutional Animal Care and Use Committee at the Technische Universität München.

Strongly phase shifting materials, such as bone, produce streaking artifacts. To reduce the magnitude of the streaks, a straightforward method was applied during reconstruction of the phase-contrast data, i.e. the differential phase data was weighted with the squared value of the interferometer visibility. This approach suppresses the bone signal as bone scatters strongly and hence causes a low weighting of the corresponding area in the differential phase data. This method however only reduces the magnitude and streaking artifacts are still present.

All attenuation- and phase-contrast CT slices were post-processed with a sharpening filter. Minor deformations in the overall shape of the mouse and changes in the position of few air bubbles are apparent between the different measurements and image registration was performed manually.

Magnetic resonance imaging: The MR scanner was a clinical 1.5 T device (Philips Achieva), which is installed at the Radiology Department of the university hospital of Technische Universität München (Klinikum rechts der Isar, Munich, Germany). Even though the scanner is designed for humans, it is routinely used for small-animal research. To account for the smaller size of the mouse, i.e. to increase the spatial resolution, a dedicated microscopy coil (diameter of 47 mm) was used. This coil enables an isotropic voxel size of $130 \times 130 \times 130 \mu\text{m}^3$ and a FOV of $55 \times 55 \text{mm}^2$. The MR sequence was a 3D turbo spin echo, with a total acquisition time of approximately 14 hrs and the images were T2-weighted³.

3.5.3 Measurement of X-ray dose

For determining the X-ray dose in each measurement, a clinically approved dosimeter (Patient Skin Dosimeter, Unfors, Sweden) was used. This dosimeter is designed for monitoring the X-ray dose during fluoroscopic CT procedures and is calibrated for entrance skin dose at 90 kVp. According to the manufacturer, the dose in free air can be determined from the displayed entrance skin dose when taking a conversion factor of 1.4 into account. The difference in X-ray energy for the different experimental setups (35 keV - synchrotron; 23 keV - tube) was not considered, and the determined dose value is hence subject to some uncertainty. However, a precise dosimetry of the performed CT measurements was not the objective of this investigation and the dose value rather serves the purpose of evaluating the general compatibility with preclinical in-vivo imaging. In the technical specifications, the

³TR = 1000 ms, TE = 95 ms, turbo factor 15, echo train length 333 ms, 6 NSA. A DRIVE pulse compensated for the short repetition time.

manufacturer quotes an energy dependence of $\pm 15\%$ (40 kVp–150 kVp) and an uncertainty of $\pm 6\%$. The error in the determined dose values, for good measure, is hence assumed to be within 25 %.

Since both the synchrotron and tube source imaging setup are not optimized for dose, two dose values were determined: the actually delivered dose and a feasible dose value. The latter value is calculated from the experimentally measured one and is based on two premises: i) 70 % detective quantum efficiency (DQE), ii) thinner silicon wafer support (100 μm vs. 500 μm) of the gratings. A DQE of 70 % is used as state-of-the art CMOS imaging detectors reach such high DQE at comparable pixel sizes of $75 \times 75 \mu\text{m}^2$ (Dexela 2923) (Konstantinidis et al., 2012). A wafer thickness of 100 μm is technologically feasible and grating wafers would still provide sufficient mechanical support. The procedure for determining the feasible dose value is:

- Measurement of actual dose.
- Determination of the detector DQE and subsequent scaling of the measured dose value according to the ratio of the actual DQE and the assumed DQE of 70 %.
- Additional scaling of the dose value according the ratio of the attenuation in 500 μm wafers and 100 μm wafers. The magnitude of attenuation in this case is calculated mono-energetically for the following energies: 35 keV (synchrotron), 23 keV (tube).

Synchrotron setup: For the synchrotron setup, the detector (FReLoN) sensitivity was determined from the DQE at zero spatial frequency, which is 30 %, according to Coan et al. (2006) (Tab. 3, first column, 33 keV). The scintillator screen thickness of the FReLoN detector in the present study was 30 μm , as opposed to a thickness of 100 μm in Coan et al. (2006). In order to account for the thinner scintillator screen—and related lower DQE—in this study, the reduced attenuation of X-rays in the thinner scintillator screen was considered and the DQE value of 30 % was scaled accordingly. This scaling results in a DQE of 11 % for our measurement.

To account for the reduced attenuation in the thinner wafers, both gratings of the two-grating Talbot interferometer were taken into account.

Tube source setup: For the tube source setup, the DQE was determined from the attenuation of 23 keV photons (interferometer design energy) in the sensitive silicon layer of 450 μm in the Pilatus II detector and amounts to 25%.

	Actual dose [Gy]	Feasible dose [Gy]
Synchrotron		
high-performance	430 ± 110	40 ± 10
low-dose	4.3 ± 1.1	0.4 ± 0.1
Tube source	6.9 ± 1.7	1.1 ± 0.3

Table 3.5: Determination of X-ray air dose. The actually measured air dose and a feasible dose value for an optimized experimental setup are listed.

The effect of thinner silicon wafers was taken into account for all three gratings of the Talbot-Lau interferometer.

Dose values: Both the actual and feasible dose value for the different imaging setups are listed in Tab. 3.5. As expected, the feasible dose value of 40 Gy for the high-performance synchrotron measurement is substantial and by far not compatible with in-vivo imaging. This is different for the low-dose measurement with a feasible dose value of 0.4 Gy. Also for the tube source measurement, the feasible dose value is significantly lower and amounts to 1.1 Gy. For comparison, dose values of up to several hundred mGy for in-vivo micro-CT imaging of mice are reported in the literature (Figueroa et al., 2008). Regarding the CT measurements performed for our studies, there is room for further dose reduction even beyond the feasible dose scenario. For example Zanette et al. (2012) recently reported a data acquisition and processing method that optimizes dose efficiency by a factor of 4, while maintaining image quality. This means that—assuming a dose-optimized setup—the low-dose synchrotron and tube measurement would reach a range that is compatible with in-vivo imaging of small animals. In this sense, both dose-reduced measurements probe image quality for phase-contrast CT in-vivo imaging applications.

3.5.4 Imaging results

Overview of imaging data and analysis: Fig. 3.6 gives an overview over the imaging data (except for the synchrotron low-dose measurement) of the abdominal area of the mouse. It shows coronal X-ray and MR images and exemplary axial histology slices. The high-performance synchrotron measurement with attenuation (left) and phase contrast (right) is shown in panel (a). Panel (b) shows the corresponding tube source measurement, (c) MRI data, and (d) histology slices. In order to distinguish between the different X-ray imaging setups and image contrasts, the following notation will be used: ACI

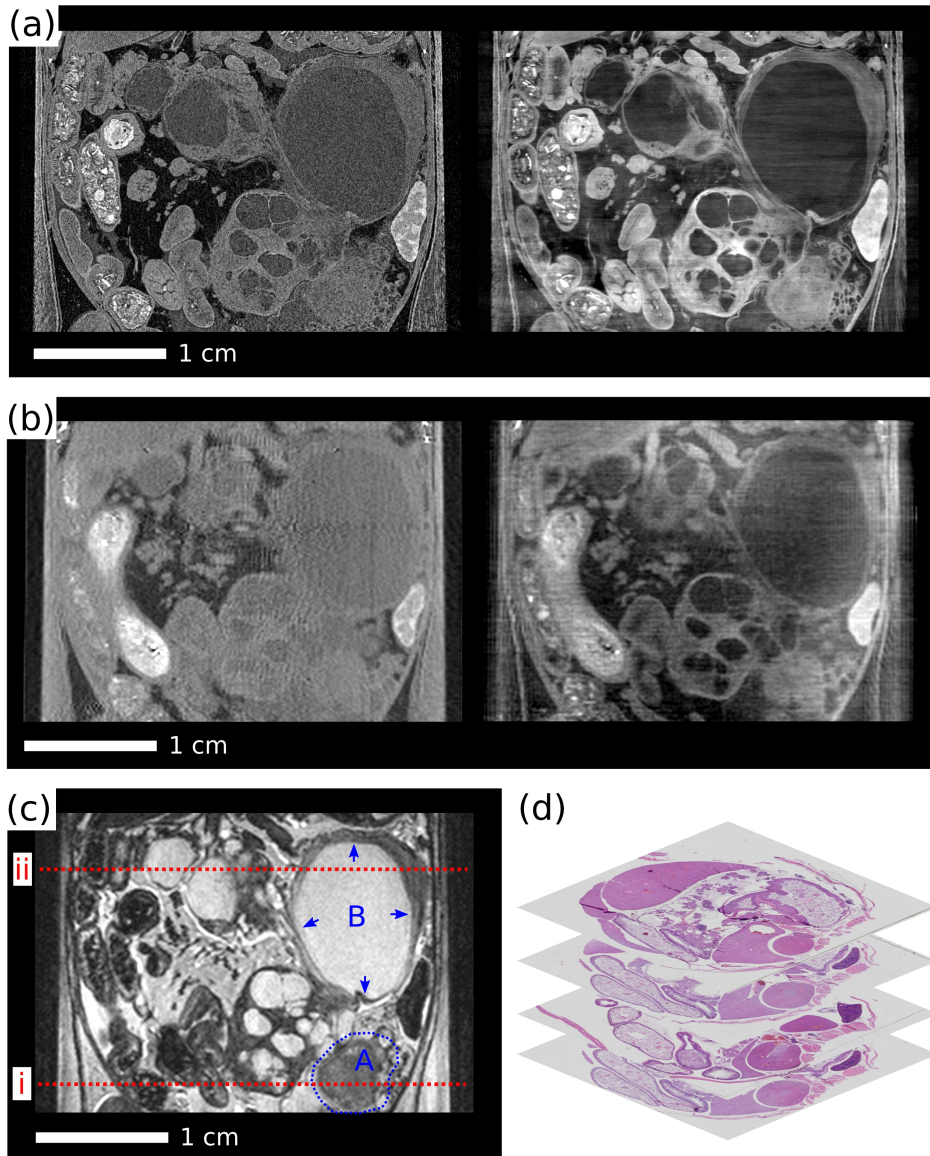


Figure 3.6: Coronal slices of the acquired multi-modal tomographic imaging data of the abdominal area in the mouse, and histology. (a) Synchrotron: Attenuation-contrast image (ACI_S) (left), phase-contrast image (PCI_S) (right). (b) Tube source: Attenuation-contrast image (ACI_T) (left), phase-contrast image (PCI_T) (right). (c) MRI with highlighted solid tumor (A) and cystic lesion (B). (d) Stack of histology slices. All images are displayed on a linear gray scale and are windowed for best visual appearance of the solid tumor and cystic lesion. This figure was previously published in Tapfer et al. (2013).

(attenuation contrast image), PCI (phase contrast image), index S for synchrotron radiation source and index T for tube source. Due to the differences in imaging parameters, there is a difference in effective pixel size between the high-performance synchrotron ($30 \times 30 \mu\text{m}^2$), the tube-based ($120 \times 120 \mu\text{m}^2$) and the MRI data ($130 \times 130 \mu\text{m}^2$). Bone as a strongly phase-shifting tissue causes streaking artifacts in transverse phase slices, similar to metal artifacts in conventional CT. These streaking artifacts appear as horizontally oriented intensity fluctuations in the shown coronal phase images. The pancreatic tumor induction gave rise to the formation of solid tumor tissue and various lesions as previously described (Hingorani et al., 2003; Siveke et al., 2007). These included pancreatic intraepithelial neoplasia (PanIN) lesions progressing to invasive PDAC as well as dilated, cyst-like ducts probably due to regional obstruction. In the MRI image (panel c), this solid tumor tissue (A) and one large cystic lesion (B) are highlighted. The further analysis of the image data is based on transverse slices at the indicated positions (red dashed lines) and is divided into two parts. To examine the potential of X-ray phase-contrast CT for in-vivo applications, the visibility of the solid tumor tissue (A), under dose-reduced conditions, is considered. The potential for virtual histology applications on the other hand is based on the high-performance data of the indicated cystic lesion (B). For both cases, X-ray attenuation and phase images from one experimental setup are compared with one another. This comparison is done both visually and quantitatively using contrast-to-noise-ratios (CNR) of selected regions of interest. Please note that this comparison is only performed for attenuation and phase images from the same imaging setting and not across settings as the experimental parameters and especially the spatial resolution are different.

Potential of phase-contrast CT for in-vivo imaging: Due to the fact that phase-contrast CT increases soft-tissue contrast, potential applications for preclinical imaging include non-invasive tumor detection and characterization. In the present mouse specimen, the solid tumor tissue is regarded for this purpose. Fig. 3.7 shows transverse slices (position indicated by profile i in Fig. 3.6) for all three X-ray imaging settings [(a)-(c)] with attenuation contrast on the left and phase contrast on the right side. As a reference, the MRI image is shown in (d). Panel (a) contains the high-performance and (b) the low-dose SR-based data. Panel (c) depicts the tube-based images. The high-performance SR-based data is shown for completeness, but naturally the dose-reduced imaging data (b and c) is of most interest for evaluating the potential for in-vivo imaging. Tumor detection by means of imaging is mainly based on a detailed knowledge of anatomy and the morphology of

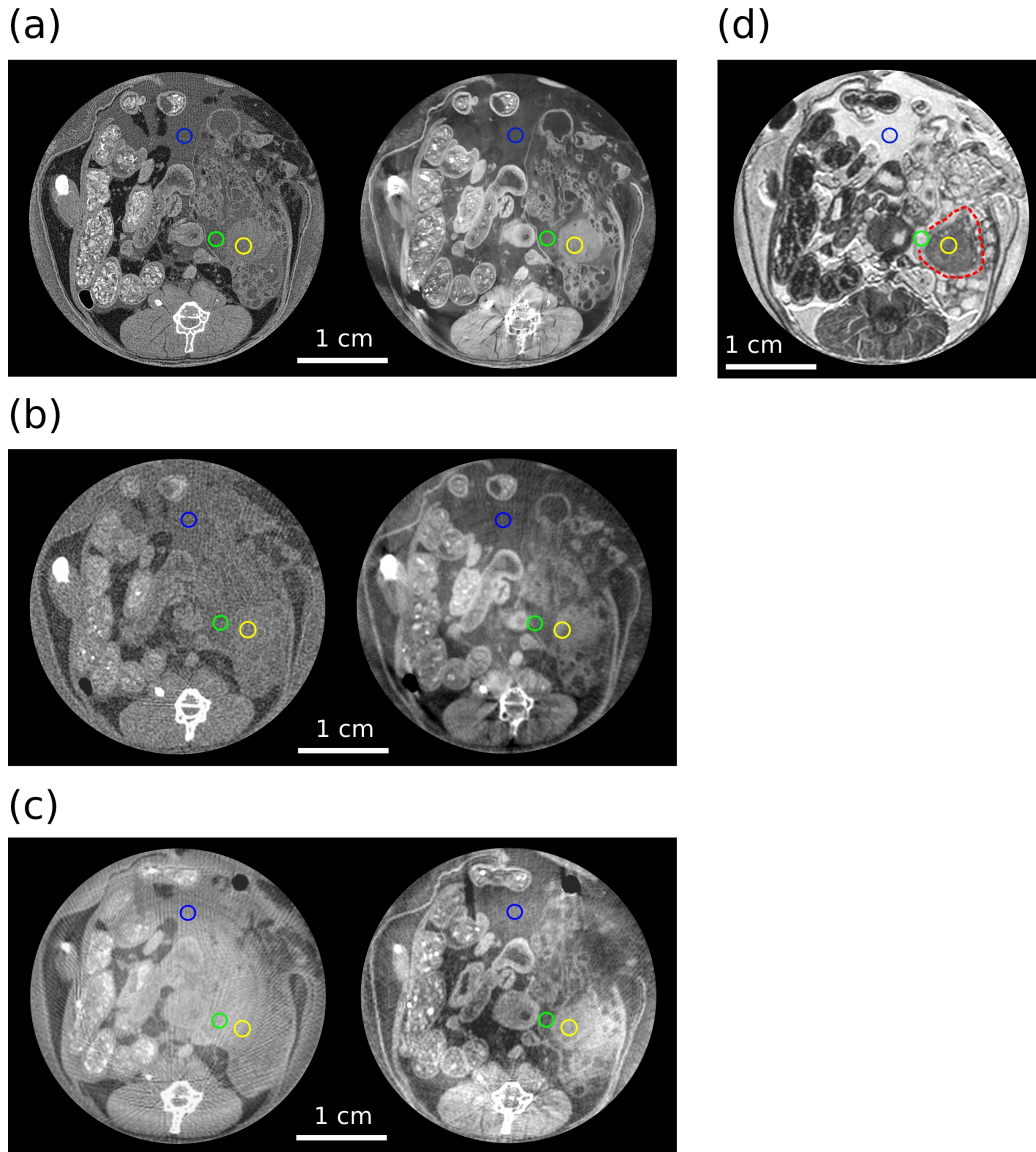


Figure 3.7: Assessment of solid tumor visibility. (a) Synchrotron: ACI_S (left), PCI_S (right). (b) Synchrotron (low dose): ACI_S (left), PCI_S (right). (c) Tube source: ACI_T (left), PCI_T (right). (d) MRI, solid tumor part indicated by red dashed line. Regions of interest for the quantitative contrast-to-noise ratio analysis are indicated by colored circles: noise (blue), surrounding tissue (green), solid tumor tissue (yellow). All images are displayed on a linear gray scale and are windowed for best visual appearance of the solid tumor. This figure was previously published in Tapfer et al. (2013).

abnormal tissue. For the present mouse specimen, solid tumor tissue was identified at the indicated position in the MRI reference image (d). In the high-performance SR-based data (a), this tissue can be identified clearly in both images, however recognizability is superior in the phase image. Visibility of this tissue is also given in the phase image of the low-dose SR-based data (b), but is very poor in the corresponding attenuation image. The same applies to the tube measurement (c)—also here, identification of the solid tumor mass is clearly possible on the basis of the phase image, but is strongly compromised in the attenuation image. This means that, for the imaging settings that assess preclinical in-vivo imaging applications, tumor visibility is strongly superior in the phase images. This observation demonstrates the potential of phase-contrast CT for tumor detection.

In order to objectify and quantify this evaluation of tumor visibility, a CNR analysis of selected ROIs was performed. Three ROIs were selected for each image: 1) covering the solid tumor, 2) covering surrounding tissue, 3) probing image noise. A separate ROI for determining noise was used because the standard deviation in a ROI reflects two opposing effects: image noise and tissue heterogeneity. Image noise should of course be considered in the CNR, unlike tissue heterogeneity that, if present within the ROI, will also increase the standard deviation and hence falsely appear as additional noise. The third ROI is hence placed within a homogenous region, and the standard deviation only reflects image noise. The CNR, based on the mean values of region 1 and 2 (M_1 and M_2) and the standard deviation of region 3 (σ_3), is then calculated according to:

$$\text{CNR} = \frac{|M_1 - M_2|}{\sigma_3}. \quad (3.2)$$

The size of the ROIs was chosen to cover an area of 1 mm², which is as large as reasonably possible to only cover the specific tissue of interest. In Fig. 3.7, the chosen ROIs are displayed in each image as colored circles: solid tumor tissue (yellow), surrounding tissue (green), homogeneous region to probe noise (blue). Tab. 3.6 lists the individual CNRs as well as their respective ratio that reflects the relative contrast improvement of phase over attenuation contrast, i.e. the relative contrast gain. The uncertainty of the CNR (σ_{CNR}) was determined by applying standard error propagation to the equation of the CNR (Eq. 3.2). The required uncertainties are the standard error (SE) of each mean value ($SE_{\text{mean}} = \frac{\sigma_3}{\sqrt{N}}$) and the standard error of the noise estimate ($SE_{\sigma_3} = \frac{\sigma_3}{\sqrt{2N}}$) (Press et al., 2007). N denotes the number of voxels in the corresponding ROI. Subsequently, error propagation was also applied to the relative contrast gain values, based on the determined uncertainties of each CNR (σ_{CNR}). The uncertainties for all CNRs and relative

	ACI	PCI	Relative contrast gain
Solid Tumor			
Synch. (high-performance)	0.37 ± 0.04	10.4 ± 0.2	28 ± 3
Synch. (low-dose)	0.6 ± 0.2	2.4 ± 0.3	4 ± 1
Tube source	0.8 ± 0.2	7.8 ± 0.6	10 ± 3
Cystic lesion			
Synch. (high-performance)	0.06 ± 0.08	7.2 ± 0.3	–

Table 3.6: Contrast-to-noise ratio analysis for solid tumor visibility and tissue composition discernibility. Based on the indicated ROIs in Fig. 3.7 and Fig. 3.8, the CNRs for attenuation and phase contrast, as well as their ratio (relative contrast gain), are listed. For the cystic lesion, the relative contrast gain is not listed as the error in the attenuation image is of the same order as the CNR itself.

contrast gain values are quoted as errors in Tab. 3.6. The relative contrast gain values range from 4 for the low-dose SR-based images, over 10 for the tube images, up to 28 for the high-performance SR-based images. The tube data are obviously of particular interest for in-vivo applications. The contrast improvement of 10 for the phase images from the tube setup compared to the attenuation images clearly underlines the strong potential of phase-contrast CT for early tumor detection for in-vivo applications. As a reference, the absolute CNR of the magnetic resonance images amounts to 8.0 (not listed in Tab. 3.6). Please note that a comparison of CNRs across different imaging setups is not directly meaningful due to the difference in spatial resolution.

Potential of phase-contrast CT for virtual histology applications:

Increased soft-tissue contrast in combination with the capability of high spatial resolution renders phase-contrast CT attractive for virtual histology applications. This potential area of application was examined on the basis of the high-performance SR-based CT data of the previously indicated cystic lesion. In tumor biology in general, and specifically for tumor characterization and therapy response monitoring, tissue heterogeneity is recognized as a characteristic feature. This is, for example, because differences in tissue composition result in regional differences in therapy response. Such a difference in tissue composition is for example present around the mentioned cystic lesion and is examined in detail in the following. Fig. 3.8 shows transverse slices of the SR-based high-performance attenuation (a) and phase-contrast data (b) and the corresponding histology slice (c). It should be noted that

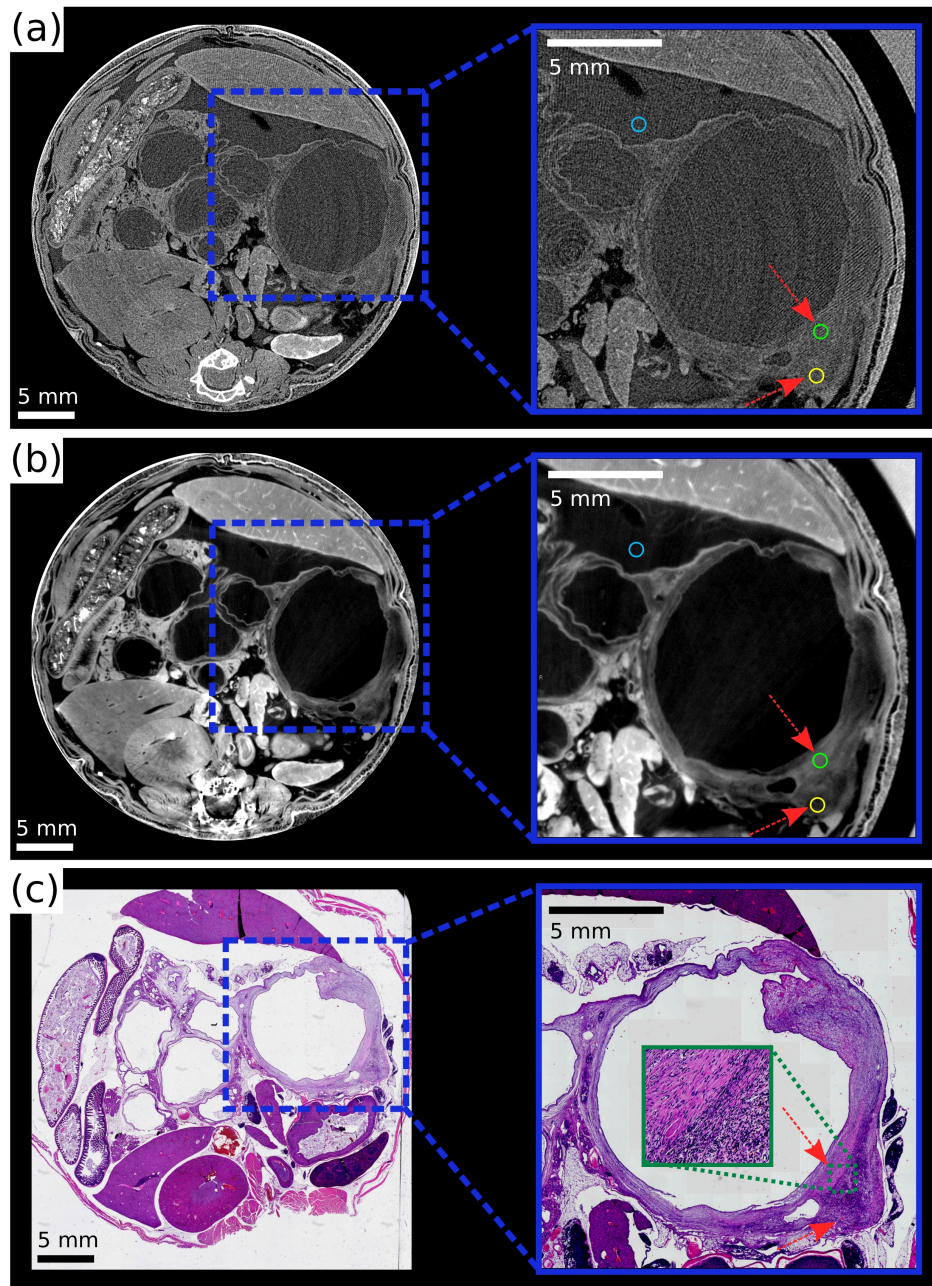


Figure 3.8: Assessment of tissue composition discernibility. (a) ACIS (left), Zoom (right). (b) PCIS (left), Zoom (right). The arrows highlight positions of differences in tissue composition. (c) Histology (left), Zoom (right). Regions of interest for the quantitative contrast-to-noise ratio analysis in the X-ray images are indicated by colored circles. All images are displayed on a linear gray scale and are windowed for best visual appearance of the cystic lesion. This figure was previously published in Tapfer et al. (2013).

the orientation of the X-ray and histology slice are marginally tilted with respect to one another, with best agreement at the lower right part of the cystic lesion, which is investigated. Moreover, in the histologic slice the upper right part of the wall of the lesion is locally deformed due to the cutting procedure. Moreover, strain fields in histological slices can lead to further deformations of the original shape (Germann et al., 2008). Most relevant for this study is the well-known tissue shrinkage caused by dehydration. While the misalignment and deformation were small enough to be tolerable for the analysis in the present case, suitable registration algorithms exist that can be used to align the tomography images with the 2D histology data and remove distortions in the general case (Müller et al., 2012). The mentioned difference in tissue composition, either fibrotic or cell-rich stroma, can be observed in the zoomed area of the histologic slice (c). The arrows indicate these two areas and the border in between is displayed in the extra zoom panel. This difference in tissue composition is also accessible in the phase image (b), i.e. at the indicated positions the cell-rich stroma appears darker and the fibrotic part brighter. In the attenuation image this information is not accessible and the surrounding tissue of the cyst appears homogeneous.

This visual impression was also analyzed quantitatively as before on the basis of the three indicated ROIs in Fig. 3.8 (area of 0.3 mm^2). The corresponding CNRs and associated uncertainties are also listed in Tab. 3.6. The very low CNR of 0.06 in the attenuation image, and the significant CNR of 7.2 in the phase image reflect the described visual impression that the discrimination of tissue composition is practically impossible in the attenuation image, but is well represented in the phase images. The relative contrast gain was not determined for this set of images as, in the attenuation image, the error in the CNR of 0.08 is on the same order as the CNR itself.

Besides the described elaborate multi-modal imaging of this mouse, one further PDAC mouse was investigated. For this second mouse, however, only high-performance synchrotron-based imaging was performed. For this reason, the second mouse was not part of the previous analysis. One interesting finding from this mouse is nevertheless presented at this point, as it also concerns tissue composition.

The second mouse was treated in the same way for pancreatic tumor induction, and the high-performance imaging parameters and histology protocol were identical (see 3.5.2). Also in the second mouse, tumor induction gave rise to the formation of solid tumor tissue. In this case, however, the tumor tissue exhibited some heterogeneity. Fig. 3.9 shows the transverse high-performance attenuation and phase images, along with the corresponding histology slice. In the zoomed area, the phase image (b) reveals a difference

in tissue composition, which is also clearly visible in the histology slice (c). In the attenuation image (a), this heterogeneity of the lesion is not visible. The access to such detailed information about internal tumor composition is of special interest for the characterization and staging of the tumor.

3.5.5 Discussion

For the assessment of the potential of phase-contrast CT for imaging of mouse tumor models, different X-ray phase-contrast imaging settings were investigated. As well-established reference technique with high intrinsic soft-tissue contrast, MRI was used. In this regard, a technical limitation of the MR scanner should be noted. The employed instrumentation of a human MR scanner with microscopy coil is not ideally suited for microscopic imaging and dedicated small animal MR scanners exist. These scanners are optimized for smaller samples and perform superior with respect to spatial resolution and contrast. For the purpose of including a well-established soft-tissue imaging technique as a reference, the performance of the MR scanner was sufficient. For an elaborate comparison of phase-contrast CT and MRI, the reader is referred to a recent study by Schulz et al. (2012), comparing phase-contrast CT, magnetic resonance microscopy and histology of the human cerebellum. When comparing attenuation and phase-contrast images from a grating-based setup in general, one aspect relating to the method should be noted. In a conventional CT setup, there are no gratings present, whereas in the grating-based CT setup, the dose-relevant final analyzer grating absorbs approximately half of the X-rays that would otherwise also contribute to the image signal. This means that attenuation-contrast images from a grating-based setup require approximately twice the dose needed for comparable images from a conventional setup.

3.5.6 Summary

The potential of grating-based phase-contrast CT for preclinical imaging applications was investigated on the basis of multi-modal ex-vivo image data of two pancreatic ductal adenocarcinoma mouse model specimens. Besides reference imaging using an MR scanner and tissue classification on the basis of histology, two different X-ray phase-contrast settings were used: firstly, high-performance benchmarking imaging using synchrotron radiation, and secondly, dose-reduced imaging using synchrotron radiation, and using a conventional X-ray tube source.

To assess the potential of phase-contrast CT for small animal in-vivo imaging, the visibility of solid tumor tissue was compared in attenuation and phase

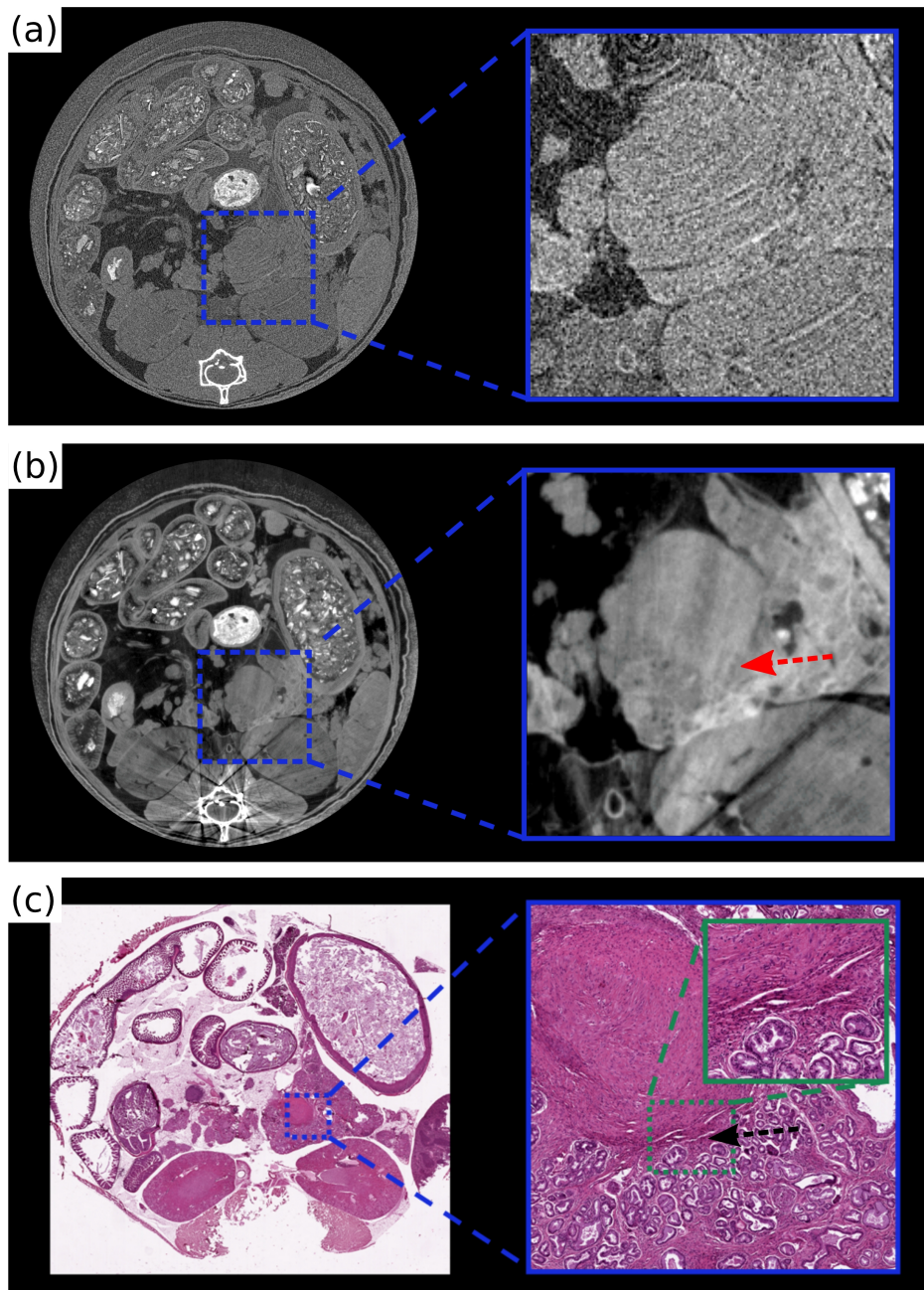


Figure 3.9: Assessment of tumor composition discernibility. (a) ACIS (left), Zoom (right). (b) PCIS (left), Zoom (right). (c) Histology (left), Zoom (right). The arrows mark the location of changes in tissue composition. All X-ray images are displayed on a linear gray scale and are windowed for best visual appearance.

images for both dose-reduced datasets. It was found both visually and quantitatively by means of CNRs that the increased soft-tissue contrast apparent in phase images does allow for tumor identification, unlike in the attenuation images. The evaluation of phase-contrast CT for virtual histology applications was based on the visibility of subtle differences in tissue composition of a cystic lesion in the high-performance SR-based data. Here, it was observed visually and quantitatively on the basis of CNRs that the phase images do display these differences in tissue composition, as opposed to the attenuation images. For the second mouse specimen, the analysis of the heterogeneity of solid tumor tissue also showed that tissue composition discernibility is only given in the phase image.

3.6 Imaging of a colon carcinoma-bearing mouse

3.6.1 Introduction

In this section, another spontaneous tumor model mouse is investigated on the basis of high-performance synchrotron radiation imaging data. Tumor induction was performed via injection of colon carcinoma cells into the tail vein of a living mouse. According to experience, tumor cells typically spread in the lung and subsequently in the liver, following blood circulation. The specific purpose of this investigation is the study of such a spontaneous tumor within the liver of the mouse. However, as it turned out, no tumor grew in the liver and a very severe lung tumor was induced only. This severe lung tumor gave rise to the formation of a secondary tumor-cell unrelated pathologic change in the liver as we shall see in the following.

A second observation was made in the head area of the mouse, more specifically in the cerebellum, which is a certain region of the brain. This observation is not related to the tumor cells either.

The imaging data of the two mentioned soft-tissue organs, the liver and the cerebellum, is analyzed and discussed in the following. Please note that both organs were not excised from the mouse.

3.6.2 Tumor model and imaging parameters

For tumorigenesis, CT-26 colon carcinoma cells (Wang et al., 1995) were injected into the tail vein of a BALB/c mouse. Cells were obtained from the *American Type Culture Collection (ATCC)* (Manassas, USA). 20 days after cell injection, the animal was euthanized and fixated in 4% formaldehyde

solution. Imaging was performed at the described beamline ID 19 of the ESRF. For the phase-contrast CT scan, 901 projections were acquired over 360 degrees. In the phase stepping procedure, 4 images were acquired with an exposure time of 1 s each. Several months after imaging, for validation, histological slices of the lung and the liver were collected.

3.6.3 Imaging results

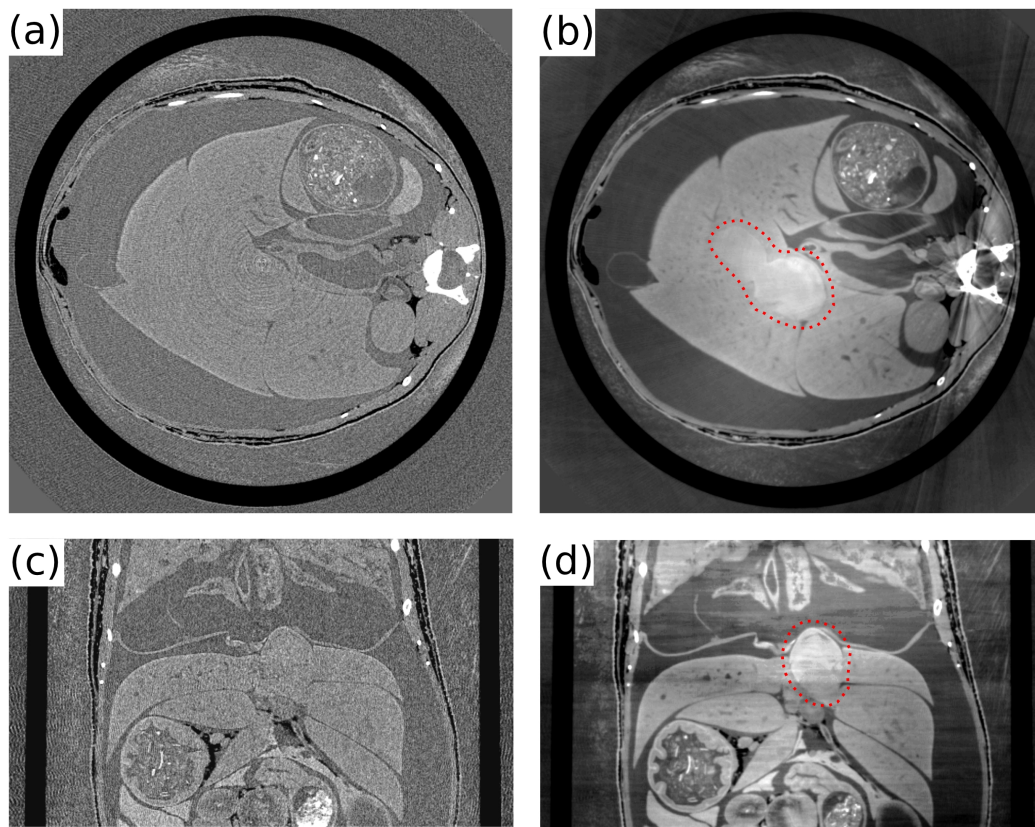


Figure 3.10: Transverse and coronal CT slices in attenuation- and phase contrast: (a) Attenuation contrast (transverse). (b) Phase contrast (transverse). (c) Attenuation contrast (coronal), (d) Phase contrast (coronal). The feature of interest in the liver is highlighted in the phase-contrast images.

Liver: Within the liver tissue, pathological changes were observed and these are displayed in Fig. 3.10. The figure shows the attenuation (left column) and phase (right column) images of a transverse (top) and a coronal CT slice (bottom). The feature of interest is highlighted in both phase im-

ages in panel (b) and (d). The pathologic change in the liver can be clearly identified from the surrounding liver tissue in the phase images. This is not the case for the attenuation images.

In order to identify the mentioned structure, histological slices were collected and the following observations were made. The intravenous injection of CT-26 tumor cells gave rise to the formation of a severe lung tumor, which in turn caused a cardiac insufficiency due to the strongly increased flow resistance in the lung. As a result, this led to a very pronounced accumulation of blood in the descending aorta, which swelled enormously as a consequence. This exceptional pathologic change of the aorta is the feature that is visible within the liver. Due to a time delay of several months between formalin fixation and histopathology, the quality of the histological slices was very poor. They suffered from dehydration and were very fragile during handling. For this reason, identification of the described pathology was solely based on the professional experience of the corresponding pathologist and unfortunately no histological slices are available for display.

It is well-known that attenuation-based CT only shows weak contrast in the liver. This matter of fact could be confirmed with the present investigation and—more importantly—it was shown that phase contrast does provide significantly enhanced contrast within the liver as the described subtle differences in tissue composition could be resolved. This finding identifies phase-contrast CT as an interesting tool for studying diseases of the liver, such as liver cirrhosis.

Cerebellum: The second organ that was investigated is the cerebellum of the mouse. As the brain itself is contained within the skull, strong streaking artifacts are expected to be present in the phase-contrast image. Fig. 3.11 shows a zoom of transverse slices of the cerebellum in attenuation (a) and phase contrast (b). As expected, the inner structure of the cerebellum is not visible in the attenuation image. In the phase image, parts of the cerebellum are visible through the intact skull. The strong streaking artifacts naturally deteriorate image quality, but a closer inspection indicates that presumably white matter and two components of gray matter can be identified. Suspected white matter is labeled with (ii) and the two suspected components of gray matter are stratum moleculare (i) and stratum granulosum (iii). Please note that white matter (ii) is only faintly visible as it appears only slightly darker in gray value than the neighboring stratum granulosum (iii).

To support the proposed tentative classification, a phase-contrast micro-CT scan of excised cerebellum of a different mouse is considered. Imaging of

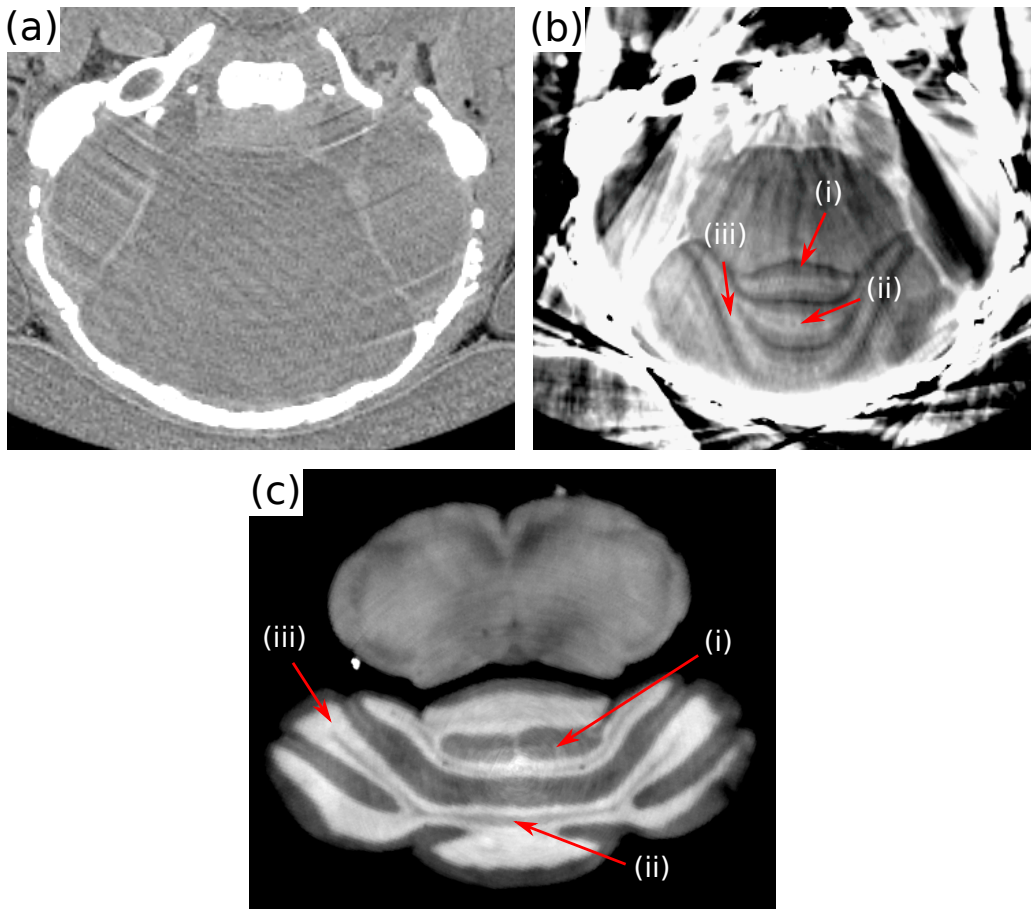


Figure 3.11: Transverse CT slices of two mouse cerebellums. Intact skull: (a) Attenuation contrast. (b) Phase contrast. Excised mouse cerebellum: (c) High-resolution phase-contrast CT slice (courtesy of Dr. Schulz, Biomaterials Science Center (BMC), University of Basel, Basel, Switzerland). Labels of suspected tissue classification: (i) stratum moleculare, (ii) white matter, (iii) stratum granulosum.

the cerebellum was performed at *Deutsches Elektronen-Synchrotron* (DESY, Hamburg, Germany) at beamline W2 (HARWI II) by Dr. G. Schulz (Biomaterials Science Center (BMC), University of Basel, Basel, Switzerland), who kindly provided the imaging data. A detailed description of the imaging setup can be found in Herzen et al. (2011). In short, at beamline W2 (HARWI II) a low coherence wiggler source is installed in the second-generation synchrotron storage ring DORIS. The horizontal source size of the wiggler of approximately 1.7 mm, in combination with a distance of approximately 45 m

to the imaging station, does not provide sufficient transverse coherence and a source grating G0 has to be used. The Talbot-Lau interferometer features the following distances: $d(G0-G1)=3$ m, $d(G1-G2)=0.32$ m. The X-ray energy was monochromatized to 23 keV by a double-crystal monochromator. This energy, in conjunction with the distance of 0.32 m between G1 and G2, corresponds to the 7th fractional Talbot order. The imaging detector, which is a scintillator lens-coupled CCD camera, had an effective pixel size of $14.1 \times 14.1 \mu\text{m}^2$. For the CT scan, 301 projections were acquired over 360 degree, and 4 phase stepping images were taken, with an exposure time ranging between 8 and 12 seconds to compensate for changes in X-ray flux. Panel (c) of Fig. 3.11 shows the phase-contrast CT slice of this measurement and the tissues are labeled correspondingly. Also here, the darkest component is stratum moleculare (i), alongside stratum granulosum (iii). In gray value slightly darker than the latter, white matter can also be discriminated (ii). When reconsidering the previous phase image (b), and keeping the morphology of white matter in panel (c) in mind, the tentative classification of white matter in (b), is underlined. Please note that the classification of tissues for both brains is based on an elaborate analysis of phase-contrast CT images of *human* cerebellum in a study of Schulz et al. (2010) and a recent comparison of X-ray phase images, magnetic resonance microscopy and histology, again of *human* brain tissue by Schulz et al. (2012). The proposed classification of tissues in the present *mouse* cerebellums is hence not definite, but is strongly indicated.

Besides the described analysis of the brain tissue itself, a further conclusion can be drawn from this measurement. Even though the X-rays penetrate a large amount of bone, spatial coherence is not degraded to an extent that phase information is lost as the phase image obviously maps real structure. Nevertheless, bone artifacts are very strong and image quality is strongly compromised. Moreover, spatial resolution limits the discernibility of brain tissue components. With further optimizations of the imaging hardware (in particular with respect to spatial resolution) and reconstruction algorithms to reduce bone artifacts, phase-contrast CT might offer a tool for imaging of non-excised brain. A potential application might be the study of trauma-induced skull fractures: attenuation images would indicate damaged bone structures and phase images would display morphological changes of brain tissue in this scenario. The principle advantage with respect to magnetic resonance imaging lies in the better spatial resolution that is available with the X-ray-based technique.

3.6.4 Summary

Even though for both cases not directly related to the injected tumor cells, two organs were identified for which soft-tissue contrast is particularly increased in phase images: the liver and the cerebellum. Both might be of interest for future investigation, for example for the study of liver cirrhosis and high-resolution imaging of brain tissue.

3.7 Imaging of mouse models of cancer: Summary

In this chapter, the results of multi-modal imaging of several mouse specimen were presented. Besides synchrotron-based and tube-based X-ray phase contrast, also magnetic resonance imaging, cryo-imaging, and histological slicing were performed. The obtained data was analyzed to assess the potential of phase-contrast CT for studying mouse tumor models.

It was found that the improved soft-tissue contrast—that has been reported numerously in the literature—has proven very helpful for the study of mice. For a formalin-fixated healthy mouse, it was found that the gain in phase image contrast excels in a, on average, 7 times larger signal-to-noise ratio for prominent organs (for an X-ray energy of 35 keV). The analysis of the pancreas tumor model resulted in two key findings. Firstly, in the dose-compatible imaging scenario, solid tumor tissue could only be identified in the phase image, but was concealed in the attenuation-based counterpart. Secondly, in the high-performance scenario, differences in tissue composition of a cystic lesion and of solid tumor tissue were only accessible in the phase images. In the CT-26 colon carcinoma model mouse two distinct organs, for which phase contrast is particularly beneficial, were identified independently of the tumor cells: the liver and the cerebellum.

Chapter 4

Development of a small-animal phase-contrast CT scanner

In this chapter, the development of a first small-animal phase-contrast CT scanner is described. The development process was divided into two main steps: first, a compact gantry was equipped with a grating interferometer for operation in rotating-sample mode. In the second step, a slightly remodelled version of this gantry was mounted in a micro-CT housing for operation in rotating-gantry mode. The instrumentation of both devices is presented and experimental imaging and stability results are shown. The chapter concludes with a description of further technical developments of the CT scanner. The main results of this chapter have been published in Tapfer et al., Development of a prototype gantry system for preclinical X-ray phase-contrast computed tomography, Med. Phys. (2011) and Tapfer et al., Experimental results from a preclinical X-ray phase-contrast CT scanner, PNAS (2012).

4.1 Motivation

After the demonstration of X-ray grating interferometry at highly-brilliant synchrotron radiation sources in the early 2000s (David et al., 2002; Momose et al., 2003; Momose, 2005; Weitkamp et al., 2005), the method was soon used for high-performance and high-resolution benchmarking imaging of biological tissue. A huge step towards clinical application of the technique was taken by Pfeiffer et al. (2006) with the extension of the interferometer by a third grating, allowing for the use of conventional tube sources. As a consequence thereof, research in the field of phase-contrast imaging strongly oriented towards potential medical applications and numerous investigations

with excised and mostly fixated tissue were performed¹. All tomographic imaging experiments were, however, based on a rotation of the sample. As this mode of operation is obviously not preferable for routine medical imaging, the leading motive of this PhD work is to take the step from *rotating sample* to *rotating gantry* by developing a first CT scanner.

As state-of-the-art medical CT scanners are highly complex devices and as the grating size, which limits the FOV, is presently limited to approximately 10 cm in diameter (see 3.1), it was a plausible decision to begin this ambitious effort with the development of a small-sized scanner for imaging of small animals. In a very close collaboration with Bruker microCT (formerly Skyscan) as industrial partner, the development of a first rotating-gantry CT scanner began in 2009.

The development process was divided into two main steps: first, a small-animal CT gantry was equipped with a grating interferometer and operated in rotating sample mode, i.e. the gantry was stationary. This gantry was then, in the second step, slightly remodeled and implemented into a standard micro-CT housing to be operated in rotating-gantry mode.

4.2 Outline

This chapter is structured as follows. First, design considerations and technical parameters of the stationary-gantry prototype and the rotating-gantry CT scanner are shown in section 4.3. Afterwards, experimental commissioning and imaging results are shown for both setups separately in sections 4.4 and 4.5. Based on the experimental findings, further technical improvements and modifications of the first CT prototype were initiated, these are described in section 4.6. Finally, the main results are summarized and the chapter concludes with a brief outlook on ongoing research in section 4.7.

4.3 Technical development

4.3.1 General design considerations

For a small-animal phase-contrast CT scanner, there are several requirements that have to be met. In order to allow for the required rotation of the gantry, the system needs to be stable with respect to the alignment of the

¹(Momose et al., 2006; Pfeiffer et al., 2007a; Weitkamp et al., 2008; Bech et al., 2009; Donath et al., 2010; Schulz et al., 2010; Castelli et al., 2011; Stampanoni et al., 2011; Stutman et al., 2011; Sztrókay et al., 2012; Hoshino et al., 2012; Schleede et al., 2012; Tapfer et al., 2013)

gratings. Here, mechanical movements of either grating of only fractions of a micrometer already cause harmful artifacts in the phase-contrast signal. The field-of-view of the system needs to be large enough to cover the specimen in the direction, which is orthogonal to the tomography axis. In the other direction (along the tomography axis), the FOV can be extended by merging consecutive CT scans. For in-vivo applications, the CT scanner should comprise an animal bed, physiological monitoring, and a warming device for the animal (as body temperature decreases during anesthesia). Depending on the application, there should ideally also be the option to trigger the image acquisition according to the heart- and breathing-movement, which of course has to be recorded for this purpose. Furthermore, the gantry should be compact and fit into a typical micro-CT scanner housing.

The general approach for the development of such a scanner was to implement a three grating Talbot-Lau interferometer, sketched in Fig. 4.1, into a modified gantry of a typical small-animal micro-CT scanner. As a starting point for conceiving the design, the total length of the interferometer (distance source grating to analyzer grating) was set to be 45 cm in order to fit into a typical Skyscan micro-CT scanner housing. The design X-ray energy was chosen according to a sample transmission of approximately 14 %,

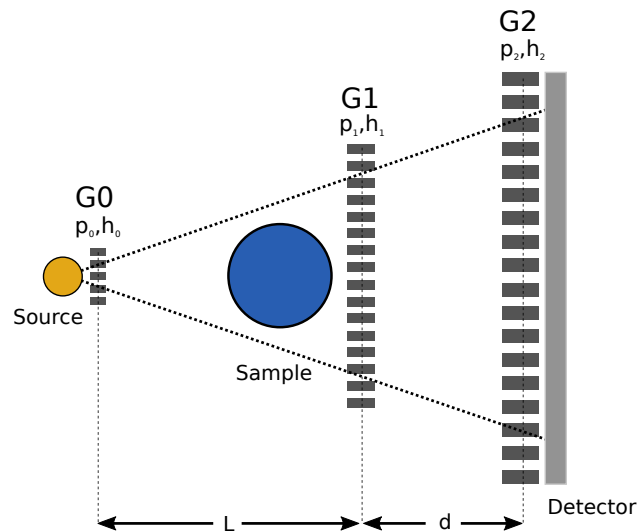


Figure 4.1: Three grating Talbot-Lau interferometer with source grating G0, phase grating G1 and analyzer grating G2. The periods of the gratings are abbreviated by p and the height of the gratings bars by h .

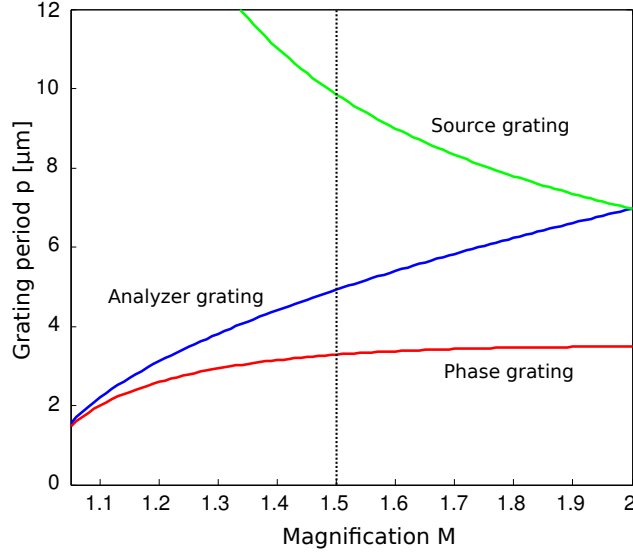


Figure 4.2: Design of the grating interferometer with the following restrictions: total length 45 cm, $\pi/2$ phase shift, design energy 23 keV, 1st fractional Talbot order. The plot shows the available periods of all three gratings as a function of magnification M.

which results in optimal image contrast according to the studies of Grodzins (1983a,b). For this purpose, a typical sample was approximated by 40 mm of water (covering the animal and the animal bed). This setting results in an X-ray design energy of 23 keV, which was also used as effective energy for the design of the interferometer. In order to maximize visibility, the interferometer was designed to be operated in the first fractional Talbot order with a $\pi/2$ -shifting phase grating.

With these constraints—total length, design energy, Talbot order—suitable grating periods can be determined as a function of magnification M, with $M = \frac{L+d}{d}$, based on the interferometer geometry considerations by Weitkamp et al. (2006). Fig. 4.2 shows these suitable grating periods as function of magnification. For a selected magnification of 1.5 and the requirement that transmission through the gold bars of the absorption gratings (at the design energy of 23 keV) is below 10 %, this results in the following specifications:

- Source grating G0 (gold): $p_0 = 10.0 \mu\text{m}$, $h_0 = 25.0 \mu\text{m}$.
- Phase grating G1 (nickel): $p_1 = 3.24 \mu\text{m}$, $h_1 = 4.0 \mu\text{m}$.
- Analyzer grating G2 (gold): $p_2 = 4.80 \mu\text{m}$, $h_2 = 25.0 \mu\text{m}$.

- Distance source grating to phase grating: $L = 300$ mm.
- Distance phase grating to analyzer grating: $d = 150$ mm.

Please note that these considerations apply to the design of both the prototype with a stationary gantry and the rotating-gantry CT scanner.

Compactness of the setup and X-ray beam divergence: In a compact setup, the divergence of the X-ray beam becomes noticeable. When the incident angle of the X-rays (relative to the bars of the grating) increases, which happens from the center towards the edges of the FOV, two effects come into play: i) geometrical shadowing that reduces the X-ray intensity, ii) the phase shift modulation of the phase grating G1 differs from the ideal shape. The two effects are displayed schematically in Fig. 4.3, showing the transmission intensity for different X-ray incident angles. The result of both is a decrease in visibility of the interferometer. Geometrical shadowing of the absorption gratings (G0 and G2) are of most practical relevance as these translate into a limitation of the FOV and/or the aspect ratio of the grat-

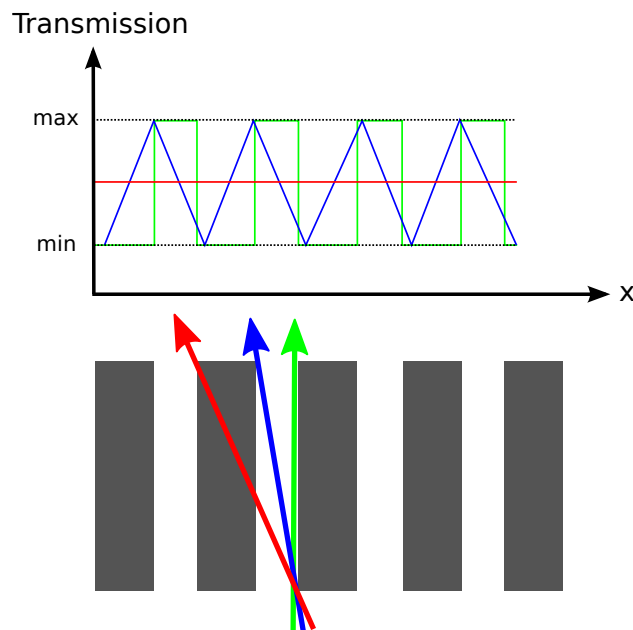


Figure 4.3: Grating transmission function for different X-ray incidence angles. The shape of the transmission function changes from a rectangular shape over a triangular shape to a constant value with increasing incident angle with respect to the grating bars.

ings respectively. For the design of our scanner, as a trade-off, we designed the height of the absorption gratings for 10 % remaining transmission and accept some shadowing. At a tube voltage of 40 kV for example, shadowing reduces the X-ray intensity to approximately 70% (relative to the center) at the very edge of the FOV. The interferometer visibility however remains constant throughout the FOV and the intensity decrease is compensated by the flat-field reference acquisition, which is performed in any case.

A different approach to address these beam divergence effects, is to bend the gratings with a circular shape. Then the orientation of the bars is parallel to the path of the X-rays throughout the FOV and theoretically no shadowing or alteration of phase shift occurs. Such bent gratings have been implemented into a compact *rotating-sample* CT scanner (Thuring et al., 2011). However, in practice, when bending the grating, small deformations can hardly be avoided, giving rise to moire-fringe artifacts. Moreover, handling and mounting of such gratings is significantly more elaborate. For these reasons, we decided to design our CT scanner with planar gratings and accept some shadowing.

4.3.2 Stationary-gantry prototype

Fig. 4.4 shows a technical drawing and several photographs of the stationary-gantry prototype that was built according to the described design. Panel (a): X-ray source (i), sample rotation stage (ii), phase grating assembly with alignment motors (iii), housing of the imaging detector (iv). Panel (b) shows a photograph of the gantry. Panel (c) shows the mounting of the source grating, and (d) shows the unmounted assembly of the phase grating. The total setup length of the gantry is 73 cm. X-rays are generated by a tungsten-target X-ray source (RTW, MCBM 65B-50 W) with a focal spot size of approximately $50\ \mu\text{m} \times 50\ \mu\text{m}$. The imaging detector consists of a scintillator screen and a 1.3 mega-pixel cooled 14-bit CCD camera. The source-to-sample and the sample-to-detector distances are approximately 280 mm and 210 mm respectively. The FOV at the position of the sample is, depending on image cropping, approximately 40 mm (perpendicular to the tomography axis) by 15 mm (along the tomography axis). This translates into a cone-beam angle of approximately 8 degree perpendicular to the tomography axis and 3 degree along the tomography axis.

All gratings were produced by the LIGA process, involving X-ray lithography and electroplating (see 2.6). The source grating G0 is positioned 3 cm from the emission point of the X-ray source, the phase grating G1 is placed 50 mm behind the sample stage and the analyzer grating G2 is positioned in front of the scintillator of the camera assembly. The source grating is $1 \times 1\ \text{cm}^2$ in

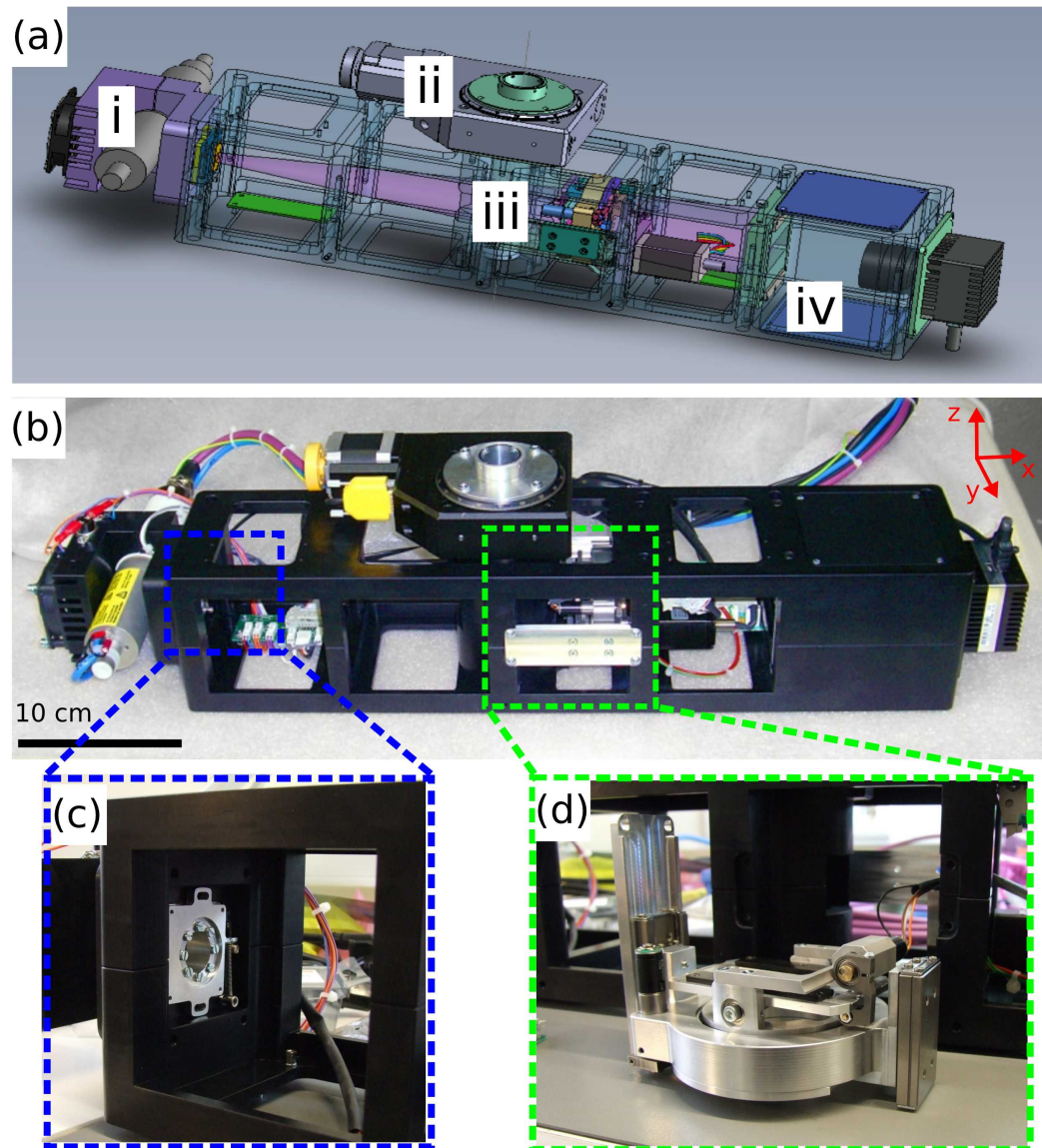


Figure 4.4: Stationary-gantry prototype. (a) Technical drawing with the following components: X-ray source (i), sample rotation stage (ii), phase grating assembly with alignment motors (iii), housing of the imaging detector (iv). (b) Photograph of the gantry. (c) Mounting of the source grating. (d) Unmounted assembly of the phase grating.

size, and the phase and analyzer grating are both $6 \times 3 \text{ cm}^2$ in size. Phase stepping is performed with the source grating (G0) using a piezo scanner (P-712, Physik Instrumente, Karlsruhe, Germany).

The following grating alignment movements are motorized (notation of axes as indicated in Fig. 4.4 (b)): G0 - rotation (around x-axis); G1 - rotation (around x-axis), tilt (around y-axis and around z-axis), and translation along the x-axis. The analyzer grating G2 is stationary.

4.3.3 Rotating-gantry CT scanner

Essentially, the described gantry was slightly redesigned and then mounted in a typical small-animal CT gantry. This redesign relates to the size of the FOV, the height of the grating bars of the source grating and the imaging detector. Moreover, an X-ray shutter was installed. Otherwise, the parameters of the setup are identical. The size of the source grating was kept the same and the size of the phase and analyzer grating was increased to a size of 7 cm round, resulting in a FOV at the position of the sample of approximately 5 cm round. This translates, depending on (rectangular) image cropping, into a cone-beam angle of approximately 7 degrees perpendicular to the tomography axis and 5 degrees along the tomography axis. In order to increase the visibility of the interferometer—at the cost of slightly more shadowing—the height of the source grating was increased by $10 \mu\text{m}$ and amounts to $35 \mu\text{m}$. The new detector features a higher sensitivity and is a flat-panel detector (Hamamatsu, C9312SK-06), which features a GOS scintillator, $50 \times 50 \mu\text{m}^2$ pixel size and an active area of $124.8 \times 115.2 \text{ mm}^2$. Fig. 4.5 shows a technical drawing of the CT gantry (a), a technical drawing of the components of the grating interferometer (b), a photograph of the scanner as installed in the lab (c), and a photograph of the gantry (d). Tab. 4.1 lists the interferometer visibility as a function of tube acceleration voltage. The change of interferometer visibility here is due to two effects: firstly, the effective energy of the

Tube voltage [kVp]	Visibility [%]
50	10
45	13
40	15
35	19
30	25

Table 4.1: Interferometer visibility as a function of X-ray tube acceleration voltage.

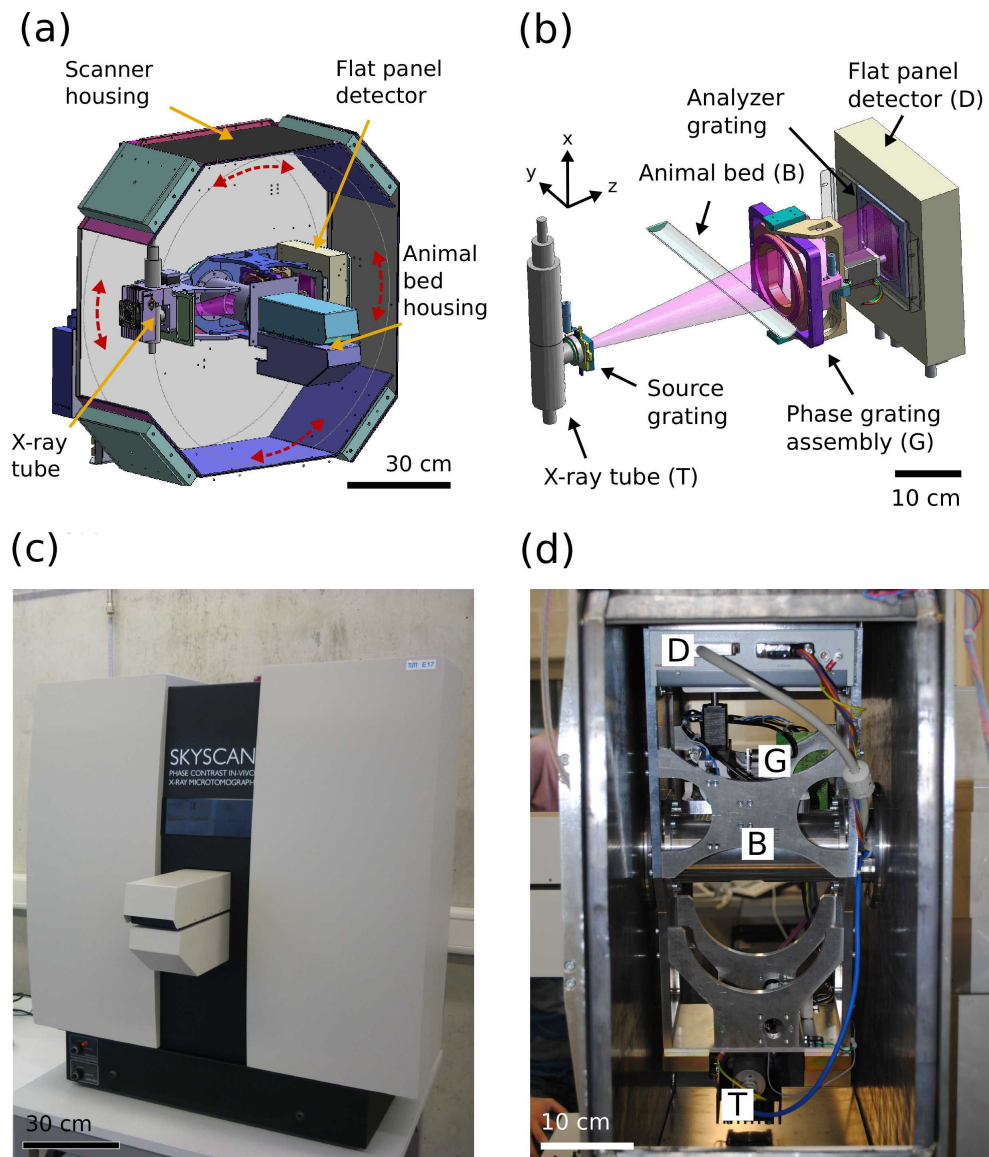


Figure 4.5: Rotating-gantry CT scanner. (a) Scanner housing with rotating gantry (gantry movement indicated by red arrows). The gantry is oriented horizontally in the displayed view. The housing dimensions are approximately 95 cm in width, 100 cm in height, and 85 cm in depth. (b) Grating interferometer, which is contained within the gantry. (c) Photograph of the rotating-gantry CT scanner. (d) Photograph of the gantry showing the detector (D), phase grating assembly (G), animal bed position (B), and tube source (T). Panel (a) and panel (b) of this figure were previously published in Tapfer et al. (2012).

spectrum is changed and secondly, the transmission through the gold bars of the absorption gratings changes. The trend of decreasing visibility with increasing energy is hence due to an increasing mismatch of effective energy and interferometer design energy, and an increasing transmission through the absorption gratings.

For a CT scan, the scanner is operated in ‘step-and-shoot mode’, i.e. at each gantry rotation angle one phase stepping procedure is performed. Then the gantry is rotated to the next angular position and phase stepping is performed again, and so on. After a certain number of image acquisitions of this kind, a certain number of flat-field acquisitions is taken with static gantry. For these reference flat-field acquisitions, the sample is moved out of the FOV. The X-ray tube is powered constantly throughout the acquisition sequence in order to preserve thermal equilibrium and the shutter is opened only during image acquisition.

In order to monitor physiological functions of the animal, an electrocardiogram can be recorded, the animal’s temperature is measured and the animal can be heated by airflow from a heated fan using Bruker microCT’s physiological monitoring system². In addition, the breathing movement of the animal can be recorded. Both the ECG- and breathing-signal can be used as a trigger signal for the image acquisition.

4.4 Results from the stationary-gantry prototype

Before implementing the developed gantry into a micro-CT housing, a commissioning and performance study in rotating-sample mode of the setup was performed. Besides an analysis of overall functionality, in particular the reconstruction accuracy in attenuation- and phase-contrast images was assessed using a chemically well-defined phantom. The experimental results of this phantom study are shown in section 4.4.1. The circumstance that attenuation and phase images are intrinsically registered was explored by color-coding the combined information of both image contrasts of the phantom study in a single image. In section 4.4.2, the results of the color-fused representation are shown.

²<http://www.skyscan.be/products/PM.htm>

4.4.1 Quantitative phantom study

To assess the performance of the rotating-sample prototype, the accuracy of CT reconstructions in phase and attenuation images was investigated. Grating-based phase-contrast CT imaging is a quantitative imaging technique in the sense that the spatial distribution of the linear attenuation coefficient $\mu(x, y, z)$ and the decrement of the refractive index $\delta(x, y, z)$ can be determined (see section 2.4.2). In case of a well-defined phantom with well-known X-ray optical properties, theoretical values for μ and δ can be determined from tabulated data. Reconstruction accuracy was then investigated by comparing the measured and theoretical values of μ and δ in the phantom.

Phantom: The phantom comprised six polypropylene tubes (7 mm diameter, 0.5 ml) mounted on a holder that was embedded in a water filled PMMA container of approximately 3 cm in diameter. The tubes were filled with accurately defined substances of well-known chemical liquids and salts to cover a range of attenuation coefficients and refractive index decrements. Tab. 4.2 lists the fluid substances contained in the phantom and their density.

Determination of theoretical values for μ and δ : As shown in section 2.5, theoretical values for μ and δ can be calculated according to Eq. 2.59 and Eq. 2.60, which are restated here. The linear absorption coefficient of a substance s , with density ρ_s , is given by $\mu_s = (\mu/\rho)_s \cdot \rho_s$. The mass attenuation coefficient of a substance, consisting of several chemical elements i , in turn is given by:

$$\left(\frac{\mu}{\rho}\right)_s = \sum_i \left(\frac{\mu}{\rho}\right)_i \cdot w_i, \quad (4.1)$$

where w_i is the weight fraction of the i -th element. For the decrement of the refractive index, it is:

$$\delta_s = \frac{r_e \lambda^2}{2\pi} \cdot \rho_s \sum_i \frac{w_i N_A}{A_i} \cdot Z_i, \quad (4.2)$$

with the elemental weight fraction w_i , classical electron radius r_e , Avogadro's Number N_A , atomic mass A_i and total number of electrons Z_i .

To compare the experimentally measured linear absorption coefficient and refractive index decrement distributions in the phantom, theoretical values for each liquid were calculated according to these equations (Eq. 4.1 and Eq. 4.2). The density of each fluid was determined using a high precision scale (Sartorius LA 230 S) by measuring the buoyancy of a gauged glass structure of 10 ml volume floating in the liquid.

Substance	Density [g/cm ³]
H2O	0.99
Glycerol	1.26
H2O + NaCl (5%)	1.03
Ethanol (50%) + Glycerol (50%)	0.98
Ethanol (25%) + Glycerol (75%)	1.11
Ethanol + NaI (1.25%)	0.80

Table 4.2: Substances contained in the phantom and their corresponding density. This table was previously published in Tapfer et al. (2011).

Data acquisition parameters and image reconstruction: The X-ray tube was operated at 40 kV and 850 μ A. For the tomography scan, 1200 projections were acquired over 360 degrees, with 4 phase steps per projection and an exposure time of 5 s per phase step. The sensitivity of the cone-beam geometry setup is reduced by a factor of r_1/l with r_1 being the source-to-sample and l the source-to-G1 distance (see 2.4.2). To correct for this, the reconstructed δ data was renormalized by a factor of $l/r_1 = 1.2$.

The cone-beam angle of this compact setup is 7.9 degrees perpendicular and 2.7 degrees along the tomography axis. Reconstruction of the tomographic cone-beam data was performed using Feldkamp’s generalized filtered back-projection algorithm (Feldkamp et al., 1984). For absorption contrast, a Ram-Lak filter and for phase contrast a Hilbert filter was used (Pfeiffer et al., 2007b). Additionally, Gaussian filtering for smoothing and ring artifact reduction were performed in the reconstruction.

Results: Fig. 4.6 shows the central attenuation and phase-contrast tomograms of the fluid phantom. For an increased signal-to-noise ratio, 50 adjacent transverse slices were averaged. Quantitative data of μ and δ for each liquid substance was extracted from these tomographic reconstructions by a region-of-interest analysis, with each region covering approximately 80% of the center of the individual tubes. Following the procedure that was introduced in section 2.5, the effective energy was determined *independently*: $E_\mu = 31.4$ keV and $E_\delta = 31.4$ keV. Tab. 4.3 lists the theoretical values for μ and δ , as well as the measured data. The standard deviation is quoted as error estimate.

From this table it is obvious that calculated and measured data agree well, the maximum relative deviation for any liquid is approximately 4%. The only exception is the Ethanol/NaI solution, the behavior of which is determined

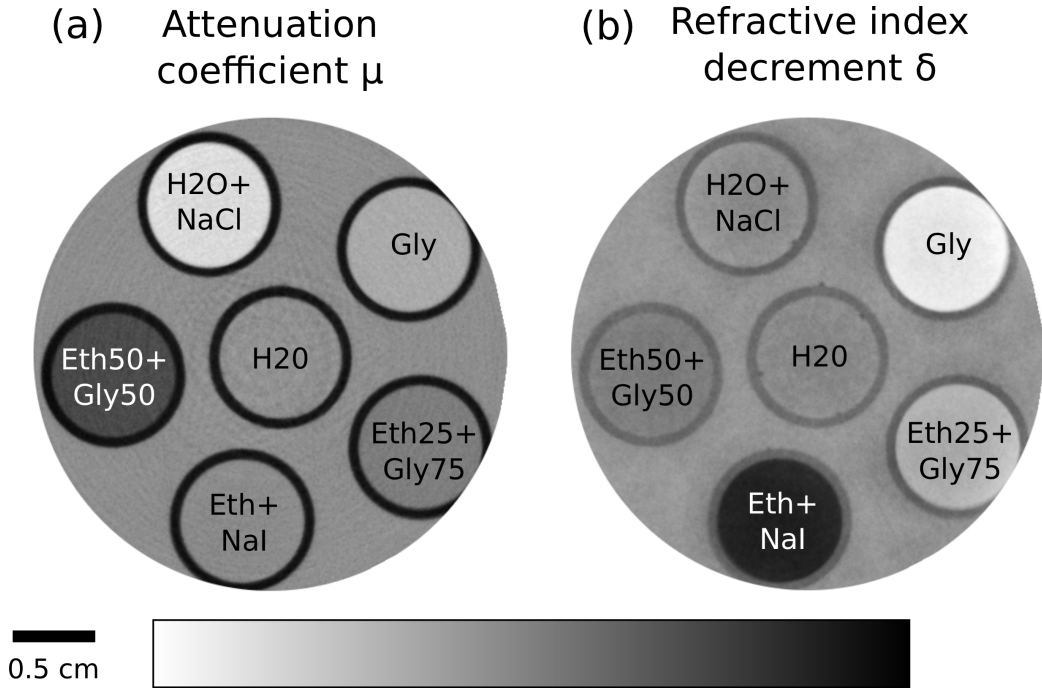


Figure 4.6: Attenuation- and phase-contrast CT scans of the fluid phantom. (a) Attenuation contrast displays the spatial distribution of the attenuation coefficient μ . (b) Phase contrast depicts the spatial distribution of the decrement of the refractive index δ . Displayed gray values are windowed from 0.20 to 0.45 [cm^{-1}] for μ and from 1.5 to 3.0 [10^{-7}] for δ on a linear gray scale. This figure was previously published in Tapfer et al. (2011).

	Substance	$\mu_m[0.1 \text{ cm}^{-1}]$	$\mu_c[0.1 \text{ cm}^{-1}]$	$\delta_m[10^{-7}]$	$\delta_c[10^{-7}]$
i	H2O	3.51 ± 0.03	3.51	2.34 ± 0.01	2.34
ii	Gly	3.76 ± 0.02	3.92	2.86 ± 0.01	2.88
iii	H2O+NaCl(5%)	4.23 ± 0.02	4.27	2.35 ± 0.01	2.40
iv	Eth(50%)+Gly(50%)	2.91 ± 0.02	2.98	2.26 ± 0.01	2.29
v	Eth(25%)+Gly(75%)	3.33 ± 0.02	3.41	2.53 ± 0.02	2.56
vi	Eth+NaI(1.25%)	3.45 ± 0.02	3.03	1.75 ± 0.01	1.90

Table 4.3: Measured (subscript m) and calculated (subscript c) μ and δ values for all substances contained in the phantom. For the measured data the mean value and the standard deviation is quoted. The roman numerals are referred to at a later stage for distinguishing the different substances. The content of this table was previously published in Tapfer et al. (2011).

Substance	CNR $_{\mu}$	CNR $_{\delta}$
H2O	–	–
Gly	4.63	16.8
H2O+NaCl(5%)	13.5	0.64
Eth(50%)+Gly(50%)	11.0	3.12
Eth(25%)+Gly(75%)	3.47	4.99
Eth+NaI(1.25%)	1.20	21.4

Table 4.4: Contrast-to-noise ratio analysis of all substances with respect to water. The content of this table was previously published in Tapfer et al. (2011).

by the absorption K-edge of iodine at 33.17 keV. This energy is very close to the effective energies E_{μ} and E_{δ} of 31.4 keV and due to the polychromatic nature of the X-ray source, a significant proportion of photons carries energies close to this edge and thus influences the measured values for μ and δ . For μ , the measured value is larger than the calculated one due to the increased absorption above the iodine edge. Correspondingly the measured δ value is slightly reduced as a consequence of the drop in the real part of the refractive index close to the iodine absorption edge. This expected behavior is reflected in the measured data and thus qualitatively explains the deviation to the calculated values at 31.4 keV.

The contrast-to-noise ratio was determined using the mean value M and standard deviation σ for each substance s and the central water container according to

$$CNR = \frac{|M_s - M_{water}|}{\sqrt{\sigma_s^2 + \sigma_{water}^2}}. \quad (4.3)$$

Tab. 4.4 contains the contrast-to-noise ratio of each liquid relative to the central water container in both attenuation and phase contrast. From these contrast-to-noise ratios it is obvious that phase and absorption contrast display complementary information and that with the combined information of phase and absorption, different substances can be significantly better distinguished than with each of the methods alone.

Fig. 4.7 displays this circumstance in a 2D scatter plot of the measured and calculated μ and δ values for each substance. This complementarity is due to the intrinsic difference of the two contrast mechanism— μ depends on electron density and the absorption cross section, whereas δ depends on electron density alone. The experimentally observed vanishing contrast in absorption between H2O and the Eth+NaI solution is not reflected in the theoretical μ values which are based on the effective energy E_{μ} . This circumstance is due

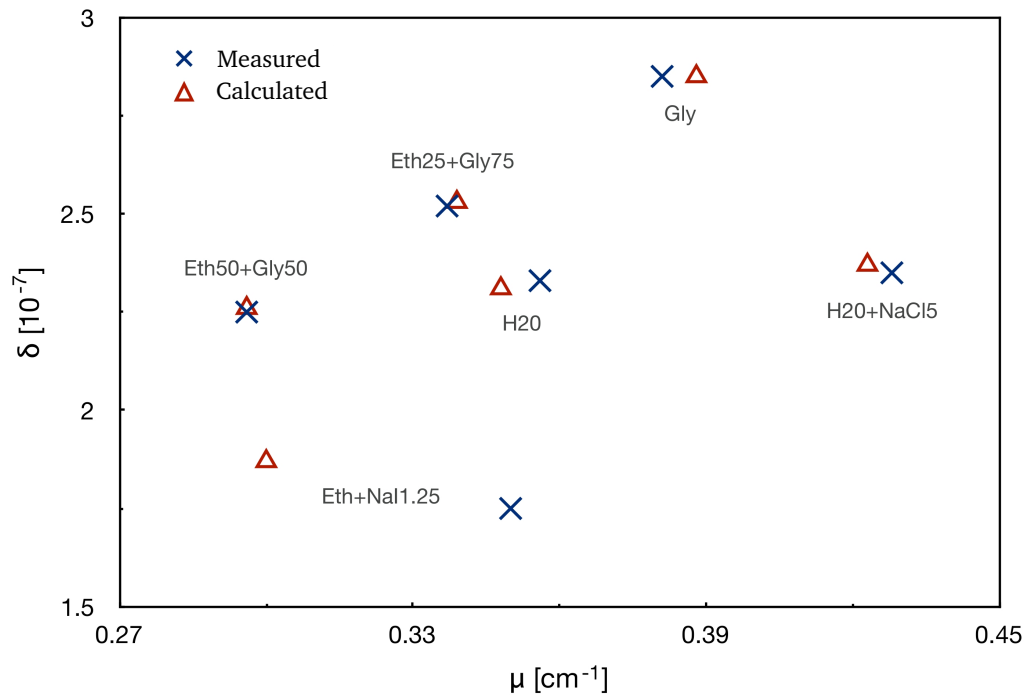


Figure 4.7: Scatter plot of calculated and measured attenuation coefficient and refractive index decrement from the described region-of-interest analysis of all substances in the phantom. The observable deviation for Eth+NaI is expected and explained in the text. This figure was previously published in Tapfer et al. (2011).

to the mentioned K-edge of iodine in combination with the polychromatic spectrum of the X-ray source which increases absorption of the Eth+NaI solution to approximately the same level as H2O and hence reduces contrast. The described experimental findings for μ and δ are in good accordance with a comparable quantitative study using a parallel-beam optical bench lab setup by Herzen et al. (2009).

4.4.2 Color coding of image contrasts

To display the complementary, multimodal absorption and phase information at once, color-fused representations can be used. As the ratio of δ and μ for each substance varies for the different substances, this property can be utilized by assigning different *hue* values of the Hue Saturation Value (HSV) color space to this ratio. Additionally, the *value* can be chosen to scale with

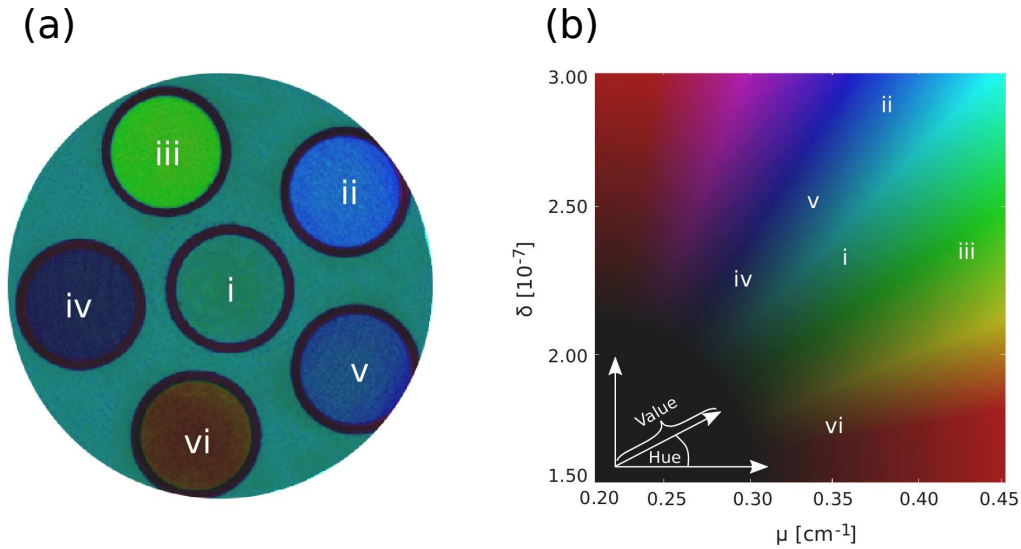


Figure 4.8: HSV color coding of absorption and phase-contrast information. (a) Transverse slice of the CT reconstruction containing both absorption and phase information. (b) The colormap displays the available color-space for a quantitative assignment of each color to its corresponding μ and δ value.

the combined signal of absorption and phase information. As the magnitude of quantitative values differs greatly for μ and δ , both transverse reconstructions were linearly scaled from 0 to 1 and then the described assignment in color space is performed: *hue* is set to the inverse tangent of the ratio δ/μ ; *value* is set to $\sqrt{\mu^2 + \delta^2}$ (scaled); *saturation* is set to 1. Fig. 4.8 (a) displays a slice of the transverse reconstruction with the described color-coding. For a quantitative assignment of each color to the corresponding μ and δ value, Fig. 4.8 (b) depicts the available HSV color-space. Roman numerals (compare Tab. 4.3) mark the mean values of the quantitative ROI analysis for each substance.

Alternatively, the RGB (red, green, blue) color model can be used. For example, assigning the μ value to *blue* and δ to *green* yields the image that is displayed in Fig. 4.9. As before, (a) displays the CT reconstruction with the combined information and (b) displays the color-space.

In summary, it can be stated that all substances can be clearly distinguished from one another using a color-fused representation in a single image, unlike in either absorption or phase contrast alone.

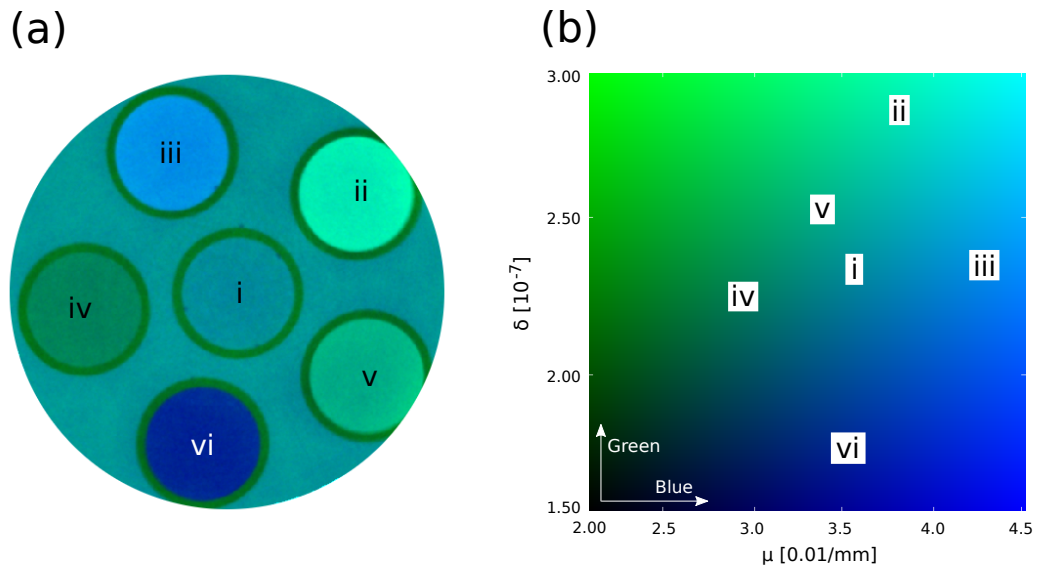


Figure 4.9: RGB color coding of absorption and phase-contrast information. (a) Transverse slice of reconstruction containing both absorption and phase information. (b) The colormap displays the available color-space for a quantitative assignment of each color to its corresponding μ and δ value.

4.4.3 Summary

The results from the stationary-gantry prototype demonstrate that the concept of grating-based phase-contrast CT can be implemented into a compact, cone-beam geometry gantry-based setup. The main conclusion from the performed commissioning experiment hence is that the next step in the development process can be taken—i.e. that the gantry can be implemented into a micro-CT scanner housing.

With respect to technical improvements, we identified that the lens-coupling of scintillator screen and CCD detector results in a rather poor quantum efficiency. For this reason, this detector is replaced by a more sensitivity-optimized flatpanel detector in the rotating-gantry CT scanner. In addition, we observed that the grating-induced shadowing effects were not strongly pronounced and as a result the height of the source grating is increased in the CT scanner.

4.5 Results from the rotating-gantry CT scanner

The main challenge in the transition from the rotating-sample prototype to the rotating-gantry CT scanner is stability. Minimal changes in grating alignment on the order of fractions of a micrometer already cause artifacts in the differential phase projection image that translate into artifacts in the CT reconstruction. For this reason, temperature and rotation stability were investigated thoroughly and the results are presented in section 4.5.1. Based on these findings, an adaptive differential phase recovery procedure was developed, which is presented in section 4.5.2. In order to assess the quantitative accuracy of this correction method, a phantom study (similar to one that was performed with the rotating-sample prototype) was conducted. Additionally, the imaging performance of the newly developed scanner for a fixated biological soft-tissue sample was investigated in a quantitative manner. The quantitative CT reconstructions of both scans are presented in section 4.5.3. Moreover, a CT scan of an excised mouse liver was performed and the imaging results are presented in section 4.5.4.

4.5.1 Stability

The mentioned artifacts in the phase signal are caused by minimal changes in grating alignment. In the present setup of the scanner, there are two different causes of grating movements: a) Thermal expansion of the source grating's mounting due to conducted heat from the X-ray target. This effect is especially relevant in the present setup due to the required compactness of the system and associated proximity of source grating to X-ray source. b) Relative mechanical movement of either grating, due to gravitational and mechanical influences on the rotating gantry system. The consequence of both effects is a drift in the phase signal occurring after power on of the X-ray tube and during gantry rotation. To measure and quantify both drifts, the fringe phases in the phase-contrast images were monitored as a function of time after X-ray tube power up (φ_{temp}) and gantry rotation angle (φ_{rot}). To reduce noise, the average fringe phase value φ of a 10×10 pixel array in the center of the phase-contrast image without sample in the FOV was analyzed in the following way:

$$\Delta\varphi_{temp}(i) = \varphi(i) - \varphi_{ref}, \quad (4.4)$$

$$\Delta\varphi_{rot}(\alpha) = \varphi(\alpha) - \varphi_{ref}, \quad (4.5)$$

with i denoting subsequent exposures with stationary gantry, α denoting the gantry rotation angle and φ_{ref} being the fringe phase value of the first image as reference. To eliminate temperature drift in $\Delta\varphi_{rot}$, that measurement was performed after the system had stabilized for several hours. Fig. 4.10 and Fig. 4.11 display $\Delta\varphi_{temp}$ and $\Delta\varphi_{rot}$. Ideally both quantities should remain zero and a deviation reflects a mechanical grating movement perpendicular to the bars of a grating on the order of the corresponding grating period per drift of 2π . For the temperature curve, one can see that the system stabilizes after approximately three hours. The shown exemplary measurement was performed with 50 kVp and 800 μ A and stabilization time varies with the X-ray tube operating parameters. When temperature stability is observed in the long term, there is a smaller modulation (please note the different axis scaling in (b)) with a periodicity of one day. This modulation is due to the change in the ambient temperature of the lab room. For $\Delta\varphi_{rot}$ (Fig. 4.11), three independent rotation stability measurements are shown in different colors. Each measurement shows a curve with approximately sinusoidal shape and change in sign of slope at approximately 90 degrees and 270 degrees, which corresponds to a horizontally oriented gantry. From this shape, it can be concluded that the force of gravity and associated bending of support structures and play in the gears of the grating alignment motors are the main sources of mechanical movement. The few steeper sections of the curve are presumably caused by mechanical hitch in the gears of the grating alignment motors. However, the behavior of $\Delta\varphi_{rot}$ is very reproducible and, most importantly, the shape of all curves is smooth, thus allowing for software correction of the drift.

4.5.2 Adaptive differential phase recovery

Naturally, a drift in the differential phase-contrast signal, caused by gantry rotation (φ_{rot}), poses a problem in a tomographic scan. To circumvent this, one could straightforwardly acquire a reference image at each angular position, but this is time consuming and not feasible for in-vivo studies. For this reason, a software post-processing method is proposed, which is based on the observation that the result of the described temperature and rotation drifts are an offset and a ramp in the differential phase projection. More precisely, the fringe phase value φ shows a spatially dependent offset in the shape of an inclined plane, which is superimposed on the regular differential phase projection.

The adaptive differential phase recovery (ADPR) works as follows. Firstly, the phase ramp in the shape of an inclined plane is determined in the differential phase projection image. For this purpose, the complex exponential

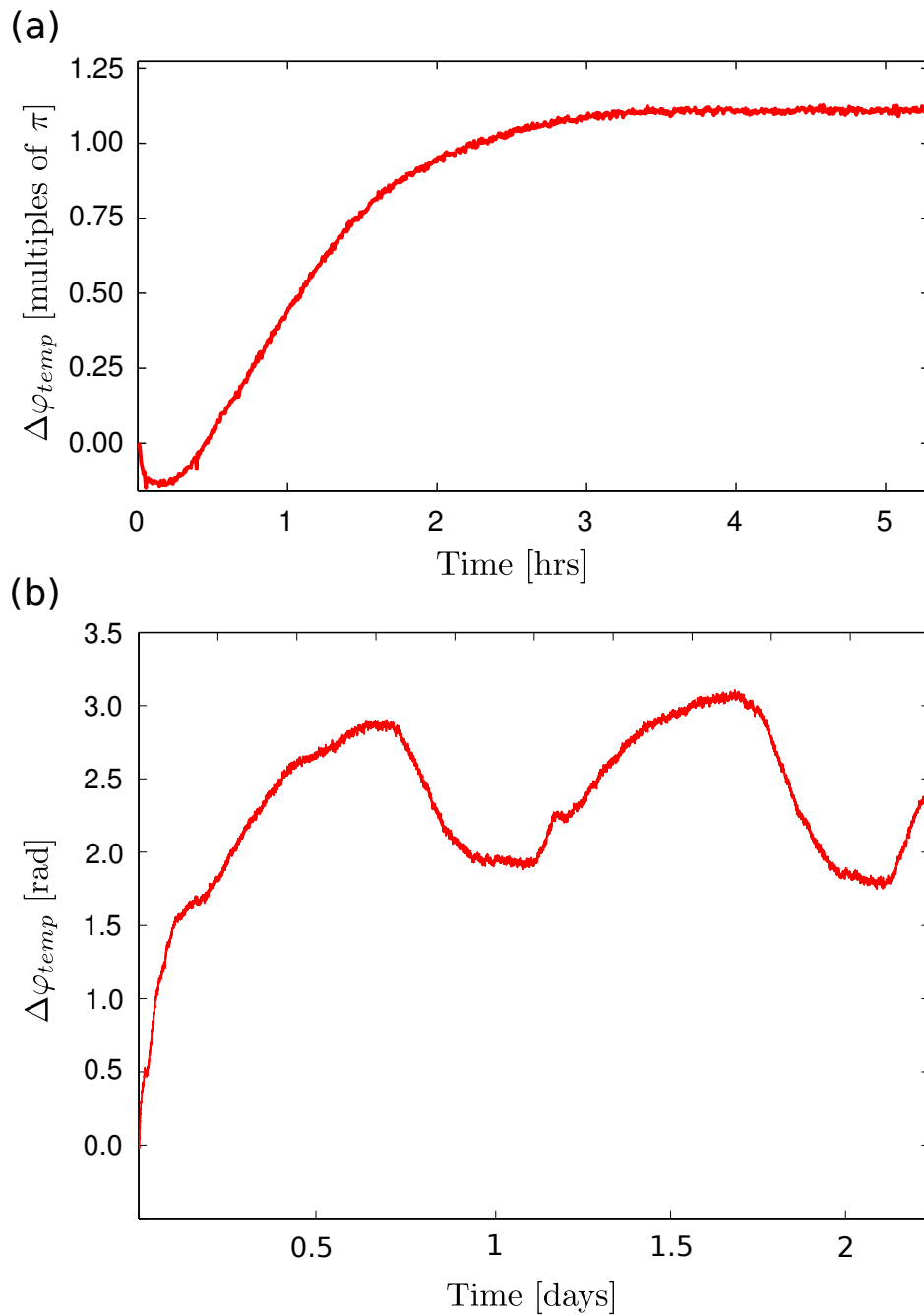


Figure 4.10: Temperature stability. Fringe phase drift $\Delta\varphi_{temp}$ as a function of time after power on of the X-ray tube: (a) short-term, (b) long-term. Panel (a) of this figure was previously published in Tapfer et al. (2012).

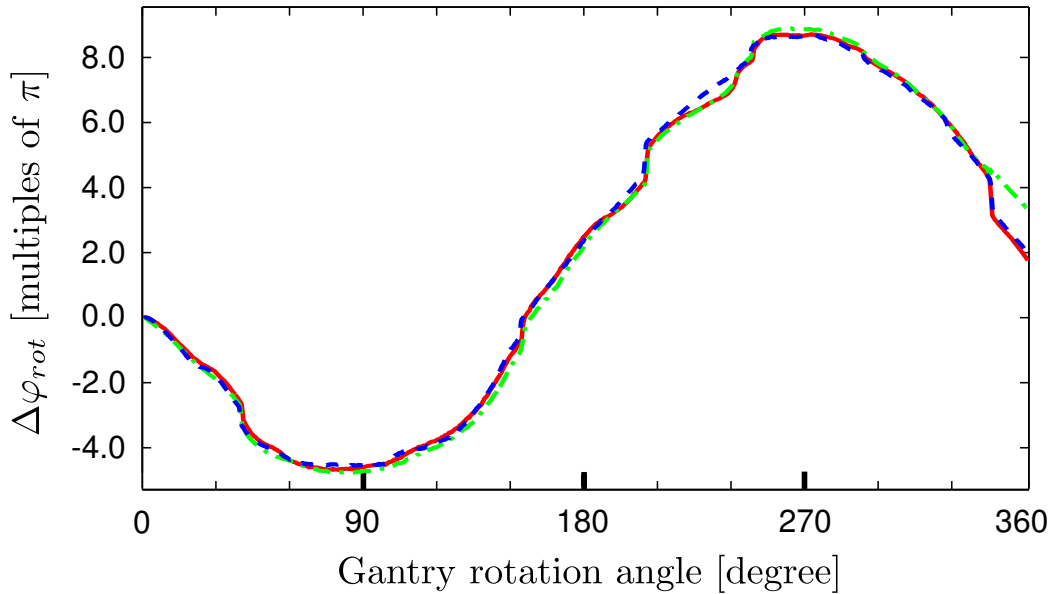


Figure 4.11: Rotation stability. Gravitationally-induced fringe phase drift $\Delta\varphi_{rot}$ of three independent measurements as a function of gantry rotation angle. This figure was previously published in Tapfer et al. (2012).

$\Gamma(x,y)$ of all image values $I(x,y)$ is taken, i.e. $\Gamma(x,y) = e^{iI(x,y)}$. In $\Gamma(x,y)$, the image gradient in x and y direction is determined, by averaging the x- and y-gradient of all pixels in $\Gamma(x,y)$. Taking the complex exponential of the image values has the advantage that phase wrapping can be dealt with due to the periodic nature of the function itself. The extracted differential phase gradients in x- and y-direction are then used to define a mathematical plane, i.e. the phase ramp. This ramp is subtracted from the original differential phase image. The resultant flat differential phase projection image can still exhibit a constant offset value. As the fringe phase value outside the sample is known to be zero, this offset value is determined from a region that does not contain the sample. This constant offset value is subtracted from the differential phase image in the last step of the processing routine. Please note that the described correction routine only removes phase wrapping, which is caused by a phase ramp or phase offset. Phase wrapping that is caused by a strong phase shift of the sample itself is not addressed by the correction procedure, but does also not deteriorate the correction procedure due to the mentioned periodicity of $\Gamma(x,y)$.

An accurate determination of the phase ramp requires an empty narrow strip on both sides of the projection images (in the direction perpendicular to the

tomography axis) that is not covered by the sample. This effectively limits the size of the scanned object in that direction. The FOV in this direction is 3.5 cm, which allows for imaging of objects up to approximately 3 cm and in particular does allow mouse imaging as the sample size is not limited along the tomography axis. Fig. 4.12 shows two exemplary projection images to demonstrate how the ADPR method works. In (a), a differential phase projection with strongly pronounced phase ramp and differential phase wrapping is shown. The existent phase ramp of that projection is determined by the ADPR method and is shown in panel (b). The ADPR-corrected differential

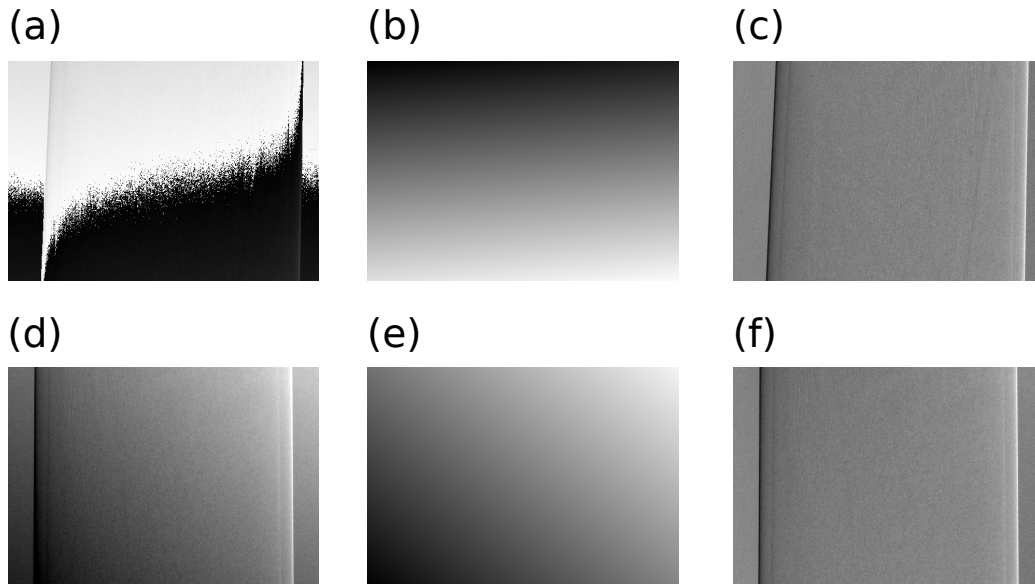


Figure 4.12: Adaptive differential phase recovery (ADPR). In order to be able to appreciate the magnitude of the phase ramp, the shown images are displayed on a linear gray scale with the windowing range indicated in square brackets. Signal saturation in these differential phase projections corresponds to image values of $\pm\pi$. (a) Uncorrected differential phase projection with a strongly pronounced differential phase ramp, which causes differential phase wrapping $[-\pi, \pi]$. (b) Subtracted differential phase plane $[-1.45, 0]$. (c) ADPR-corrected differential phase projection using the described adaptive differential phase recovery method $[-1.1, 1.1]$. (d) Uncorrected differential phase projection with a moderate differential phase ramp $[-0.8, 1.65]$. (e) Subtracted differential phase plane $[-1, 0.8]$. (f) ADPR-corrected differential phase projection $[-1.1, 1.1]$. This figure was previously published in Tapfer et al. (2012).

phase projection is shown in (c). The bottom row of Fig. 4.12 shows the same procedure for a differential phase projection with only moderate phase ramp (d). Again, the differential phase ramp was determined (e), subsequently subtracted and (f) shows the ADPR-corrected projection. The exemplary differential phase recovery of these two projection images illustrates that the phase ramp does vary for different projections, that the method can handle phase wrapping and that the original differential phase information can be recovered. The quantitiveness of this method in CT reconstructions is assessed in the next section.

4.5.3 Quantitative CT imaging results

To assess how the preclinical scanner and adaptive differential phase recovery method perform in CT measurements, two samples were measured. The tomographic reconstructions in absorption and phase contrast were then evaluated in terms of image quality and reconstruction accuracy. The first sample is a well-defined fluid phantom, which was used for the quantitative reconstruction analysis. The second sample was formalin fixated porcine rind, which consists of several layers of soft tissue. This sample was used for the benchmarking of the soft-tissue enhancement capabilities of the presented scanner.

Image acquisition and processing: The X-ray tube was operated at 40 kV and 750 μ A. For the two tomography scans, the following parameters were used for the fluid phantom (porcine rind) scan: 1000 (1500) projections over 360 degrees, 8 (8) phase steps per projection, exposure time of 7 (5) s per phase step. The scanner was operated in step-and-shoot mode, i.e. at each projection angle one phase stepping procedure was performed, then the gantry was rotated to the next angular position and again phase stepping was performed, and so on. After every 15 acquisitions of this kind, 10 flat-field acquisitions were taken with static gantry. For these flat field acquisitions, the sample was moved out of the FOV. This results in a total exposure time of 26 (28) hours for the fluid phantom (pork tissue) CT scan. The X-ray tube was powered constantly throughout the acquisition sequence in order to preserve thermal equilibrium and avoid temperature-induced phase drift. The projection images of both CT scans were 2×2 binned before reconstruction, resulting in reconstructed voxel sizes of $60 \times 60 \times 60 \mu\text{m}^3$. Ring artifact reduction in the reconstruction routine and projection-based filtering (2D symmetric normalized Gaussian function with a variance of 0.5 pixels) for smoothing were applied. Additionally, the fluid phantom reconstruction

was post-processed to reduce the existing cupping artifact caused by beam hardening.

CT reconstructions of the phantom and the soft-tissue sample:

Fig. 4.13 shows the tomographic reconstruction of the two samples: (a) and (d) phase contrast without applying the ADPR method, (b) and (e) phase contrast using the aforementioned ADPR method, (c) and (f) attenuation contrast. From this figure the importance of accurate phase recovery is directly noticeable and one can conclude that the method performs well in the sense that no artifacts remain in the corrected reconstructions [(b) and (e)]. In order to assess whether the tomographic reconstruction also yields quantitatively accurate results regarding the linear attenuation coefficient μ and decrement of the refractive index δ , the mentioned phantom study was evaluated quantitatively. A quantity derived from μ , which is commonly used in clinical CT scanners, is the Hounsfield unit. As suggested by Donath et al. (2010), a corresponding quantity can be defined for phase images. To discriminate between these two Hounsfield units, the conventional attenuation Hounsfield units are referred to as HU-A and the phase Hounsfield units as HU-P. HU-A and HU-P are defined as (Donath et al., 2010)

$$\text{HU-A} = \frac{\mu - \mu_{\text{wat}}}{\mu_{\text{wat}} - \mu_{\text{air}}} \times 1000, \quad (4.6)$$

$$\text{HU-P} = \frac{\delta - \delta_{\text{wat}}}{\delta_{\text{wat}} - \delta_{\text{air}}} \times 1000, \quad (4.7)$$

where δ_{wat} , μ_{wat} and δ_{air} , μ_{air} denote the refractive index decrement and linear attenuation coefficient of water and air. The mentioned phantom comprised seven polyethylene tubes that were embedded in a water-filled plastic container of approximately 3 cm in diameter. The individual tubes were filled with chemically pure liquids and mixtures with salts to span a range of Hounsfield units in absorption and phase contrast. Following the procedure that was introduced in section 2.5, the effective energy was determined ($E_{\mu} = 30$ keV, $E_{\delta} = 27$ keV) and theoretical values for μ and δ were calculated. The corresponding theoretical Hounsfield units, were calculated according Eq. 4.6 and Eq. 4.7. The density of the individual substances, which is required for calculating theoretical values of μ and δ , was determined using a high-precision scale (Sartorius LA 230 S). The results are listed in Tab. 4.5.

Tab. 4.6 contains the measured and calculated HU-A and HU-P for all substances in the phantom. From this table it is obvious that calculated and measured HU data agree well, the maximum deviation is 4 HU for phase and

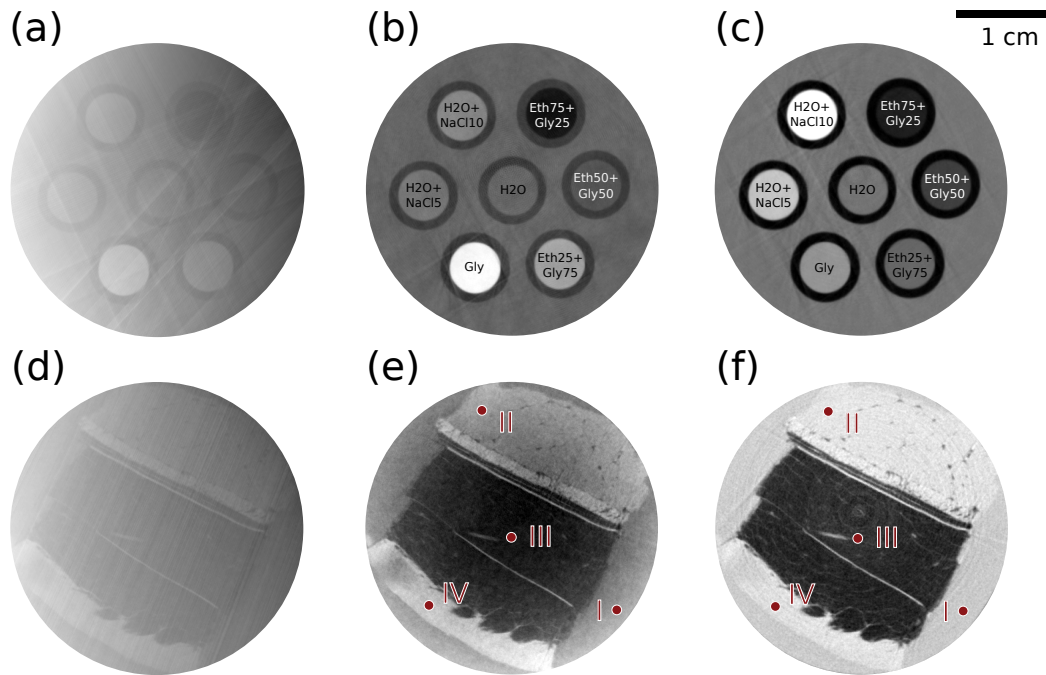


Figure 4.13: Quantitative reconstructions of the fluid phantom (top) and the porcine rind sample (bottom). To reduce image noise, the reconstructions were averaged over 30 adjacent slices for the fluid phantom and over 5 slices for the porcine rind. (a) and (d) Phase contrast without adaptive differential phase recovery. (b) and (e) Phase contrast with adaptive differential phase recovery. (c) and (f) Attenuation contrast. Fluid phantom (top row): Labels - H₂O+NaCl10 (Water and 10% NaCl solution), Eth25Gly75 (25% Ethanol and 75% Glycerol solution); other substances are named accordingly. Image windowing: (b) HU-P [-144,232], (c) HU-A [-335,400]. Porcine rind (bottom row): Labels - (I) formalin background, (II) muscle, (III) two layers of subcutis (divided by connective tissue), (IV) dermis/epidermis. Image windowing: (e) HU-P [-249,91], (f) HU-A [-307,69]. This figure was previously published in Tapfer et al. (2012).

Substance	Density [g/cm ³]
Ethanol (75%)+ Glycerol (25%)	0.877
Ethanol (50%)+ Glycerol (50%)	0.982
Ethanol (25%)+ Glycerol (75%)	1.110
Glycerol	1.260
H2O + NaCl (5%)	1.033
H2O + NaCl (10%)	1.069
H2O	0.997

Table 4.5: Substances contained in the phantom and their measured density.

	HU-A(m)	HU-A(c)	HU-P(m)	HU-P(c)
Fluid Phantom				
Eth.(75%)+Gly.(25%)	-251 ± 9	-260	-112 ± 6	-114
Eth.(50%)+Gly.(50%)	-157 ± 9	-161	-17 ± 6	-18
Eth.(25%)+Gly.(75%)	-41 ± 10	-39	99 ± 7	100
Gly.	94 ± 12	105	236 ± 8	235
H2O+NaCl(5%)	230 ± 14	230	32 ± 7	29
H2O+NaCl(10%)	466 ± 15	463	61 ± 6	57
H2O	0 ± 14	0	0 ± 7	0
Porcine rind				
Formalin background (I)	-9 ± 7	-	-37 ± 7	-
Muscle (II)	31 ± 7	-	12 ± 6	-
Subcutis (III)	-251 ± 11	-	-198 ± 7	-
Dermis/Epidermis (IV)	25 ± 9	-	57 ± 8	-

Table 4.6: Quantitative analysis of the performed CT scans of the fluid phantom (top) and porcine rind sample (bottom). Measured (m) and calculated (c) attenuation (HU-A) and phase (HU-P) Hounsfield units are quoted for different regions of interest (ROI). Fluid phantom (top): The HU data was extracted from a ROI analysis covering the central 80 % of the individual substance containers of 30 averaged adjacent transverse CT slices. The standard deviation is quoted as error. Porcine rind sample (bottom): The measured Hounsfield units of a ROI analysis (region marked with red circle in Fig. 4) of the different tissue composites and formalin background are quoted. The standard deviation is quoted as error.

11 HU for absorption. This means that the proposed ADPR method does allow for quantitatively accurate CT reconstruction of Hounsfield phase and attenuation units.

The potential of the phase-contrast scanner for biomedical imaging was examined by scanning a porcine rind sample as it contains different layers of soft tissue. For a quantitative comparison of both contrast modes, Hounsfield units for the different types of tissues were determined at the indicated positions in Fig. 4.13 (red colored circles, 20 pixel in diameter) and are also quoted in Tab. 4.6. In order to be able to compare both contrast modes visually in an objective manner, the gray value windowing was chosen such that the tissue with the highest (lowest) Hounsfield unit corresponds to 90 % (15 %) of the available gray value range. This results in an image windowing of [-307,69] for HU-A and [-249,91] for HU-P.

Whereas the subcutis (III) can be identified well in both the phase contrast image (F) and absorption contrast image (E), especially the muscle (II) and dermis / epidermis (IV) can be more clearly distinguished from the embedding medium formalin (I) and in particular from one another in phase contrast. This visual observation is also reflected in the quantitative HU data in Tab. 4.6. This means that, also for biological tissues, attenuation and phase contrast are complementary. When comparing attenuation and phase contrast, it should be noted that for conventional attenuation contrast no gratings and in particular no analyzer grating G2, which absorbs approximately half of the X-ray photons and hence decreases counting statistics, are needed. However, grating-based phase contrast on the other hand supplies two perfectly registered and complementary images from one CT scan.

4.5.4 CT scan of excised mouse liver

In section 3.6 of the previous chapter, it was observed that soft-tissue contrast was strongly increased for the liver in a synchrotron-radiation-based CT scan of a fixated mouse. In order to explore this observation with the rotating-gantry CT scanner, a CT scan of a mouse liver was performed. The liver was excised from a CT-26 colon carcinoma-bearing mouse that, according to experience, is likely to exhibit metastases in the liver. Tumor induction was performed as described in section 3.6. After resection, the liver was embedded in formalin and placed in a plastic cylinder. The size of the fixated liver was approximately 1.5 cm in diameter.

For the CT scan, 901 projections were acquired over 360 degree, with 6 phase-stepping images of 6 s exposure time each. Every 10 projections, 5 reference flat-field data acquisitions were performed. To reduce noise, the projections were binned 2×2 prior to reconstruction, resulting in a voxel

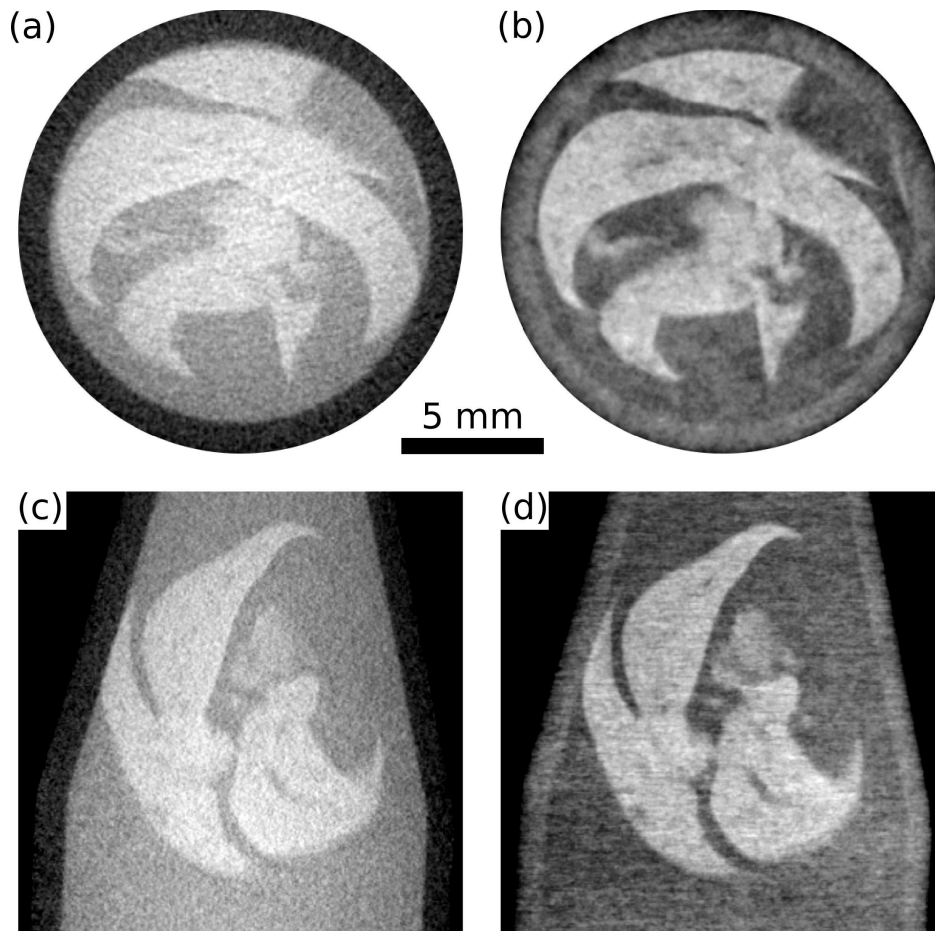


Figure 4.14: CT scan of a formalin-fixated excised mouse liver. The attenuation, [(a) and (c)], and phase images, [(b) and (d)], are shown in transverse, [(a) and (b)], and longitudinal, [(c) and (d)], slice orientation. To reduce noise, all images were averaged over three adjacent slices. The images are displayed on a linear gray scale and are windowed for best visual appearance.

size of $60 \times 60 \times 60 \mu\text{m}^3$ for the CT volume. Fig. 4.14 shows attenuation (left column) and phase (right column) CT slices in transverse (top row) and longitudinal (bottom row) orientation. All shown views represent the average of 3 adjacent slices to reduce noise further. Please note the difference in noise texture in the transverse and the longitudinal phase-contrast CT slice. The horizontally oriented fluctuations in the longitudinal slices are intrinsic to the imaging method, as shown by Li et al. (2012). Contrast in general is noticeably increased in the phase images and faint internal structure of the liver is visible in the phase images. Metastatic tissue can, however, not

be identified. This could be due to several reasons. First of all, it is not definite if metastases are present in general as histology was unfortunately not performed. Further reasons could be that the metastases, if present, are in early stage and are too small to be resolved. Moreover, contrast could be too low. The imaging results nevertheless show that contrast in liver tissue is strongly increased and that further investigations are worth pursuing.

4.5.5 Summary

In order to take the next step in the translation of X-ray phase contrast CT to clinical applications, a first preclinical CT scanner was developed. The main challenge in the transition from bench-top systems with rotating sample to a rotating-gantry CT scanner were phase artifacts that are caused by minute changes in grating alignment. For the correction of these artifacts an adaptive differential phase recovery method was proposed. With the quantitatively accurate reconstruction of attenuation and phase Hounsfield units of a phantom, it was demonstrated that this correction routine performs accurately and that reconstructed μ and δ values are reliable.

The shown imaging results of porcine rind and excised mouse liver, with complementary information in absorption and phase images, underline the potential of the scanner for preclinical imaging.

4.6 Further development and technical issues

As we have seen in the previous section, the developed rotating-gantry CT scanner is fully-functioning and quantitatively accurate CT scans can be performed. This section is concerned with improvements of the CT scanner, and technical issues that were identified in the course of the described measurements. The guiding aim for the further development is the reduction of radiation dose and the reduction of acquisition time in CT scans, both in the view of future in-vivo imaging experiments.

For repetitive small-animal studies, radiation doses of several hundreds of mGy are tolerable at maximum (Figuroa et al., 2008). For the previously presented proof-of-principle CT scans of the phantom and the porcine rind, dose was estimated to be several Gy. With respect to acquisition time, a fundamental limit for in-vivo imaging originates from the tolerable time of anesthesia for the animal. This time should ideally not exceed one hour. For the presented CT scans, acquisition time was more than 20 hours. It is hence necessary that both radiation dose and acquisition time are reduced for repetitive small-animal in-vivo studies.

In this context, the following technical aspects and associated improvements are considered: rotation stability, interferometer design energy, X-ray absorption in silicon wafers, data acquisition and CT reconstruction, and deterioration of the source grating.

4.6.1 Improvement of rotational stability

As we have seen in section 4.5.1, the force of gravity has a distinct impact on the rotational stability and affects differential phase images. The underlying misalignment in gratings is caused by bending of support structures and bearing play in the mounting of gratings. The holder of the source grating allows for a rotation around the optical axes and for phase stepping. The analyzer grating (G2) is mounted stationary and is not motorized. For this reason, the phase grating assembly, with motorized movements for rotation, tilt and especially shift along the optical axis, is most affected by the rotational movement.

To reduce the gravitationally-induced grating misalignment, the positioning drives and mounting of the phase grating assembly were improved: zero-backlash gears were installed and the entire phase grating assembly was additionally fixated by a mechanical spring. Primarily due to the strongly reduced backlash, and secondary due to the constant spring load, the effect of gravity was strongly reduced. Fig. 4.15 shows the installed spring that connects the phase grating assembly with the gantry itself, such that the spring force acts in the direction of the optical axis. With this reworked grating mounting, rotation stability was investigated again. The same procedure as introduced in section 4.5.1 was followed, resulting in a plot of the fringe phase value $\Delta\varphi_{rot}(\alpha)$ as a function of gantry rotation angle. Fig. 4.16 displays $\Delta\varphi_{rot}(\alpha)$ for both the previous grating mount and the reworked mount. As can be seen from this plot, rotational stability is greatly enhanced: the magnitude of the phase drift is approximately four times smaller and the curve is smoother. Additionally, the curve is more symmetric and there is nearly no offset between 0 degree and 360 degrees gantry rotation angle.

In practice this means that fewer reference flat-field acquisitions during gantry rotation are necessary. Due to the involved animal bed movement out of the FOV, these reference flat-field acquisitions are rather time-consuming. As a result of the improved grating mount, the acquisition time of CT scans could be reduced significantly.

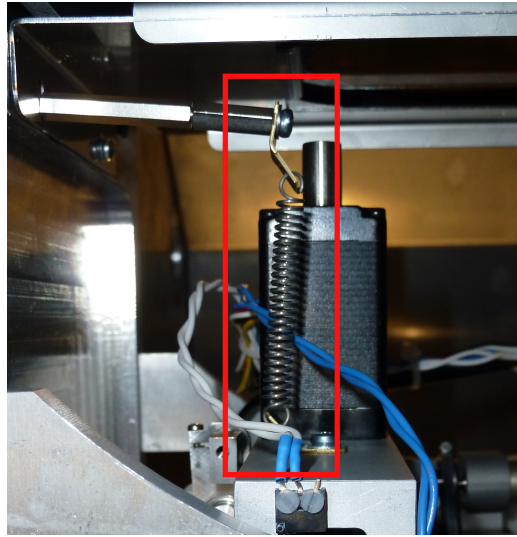


Figure 4.15: Photograph of the spring-enforced phase-grating mount. The spring connects the phase grating assembly (bottom part of the spring) with a metal rod, which in turn is connected with the gantry itself (upper part of the spring).

4.6.2 Adjustment of interferometer design energy

The imaging performance of a grating interferometer strongly depends on the energy of the incoming X-rays. This is why the interferometer is designed for one particular energy (design energy) at which it performs optimal. This means in practice that the effective energy spectrum—the spectrum that is emitted by the tube source and filtered by the grating wafers and the sample—should be centered around this particular design energy. For the CT scanner, the interferometer design energy is 23 keV. Based on the procedure that was explained in section 2.5, the de-facto effective energy was determined in the quantitative phantom study (see 4.5.3) with the following result: $E_{\mu} = 30$ keV, $E_{\delta} = 27$ keV (for an X-ray tube voltage of 40 kV). Considering that the design energy of the interferometer is 23 keV, one can conclude that the interferometer is currently not designed optimally.

On the basis of this finding, gratings for a higher design energy are currently conceived. Once installed, these gratings will increase the visibility of the interferometer and hence increase the signal-to-noise ratio. This in turn will allow for shorter exposure times, effectively reducing the dose and total data acquisition time in CT scans.

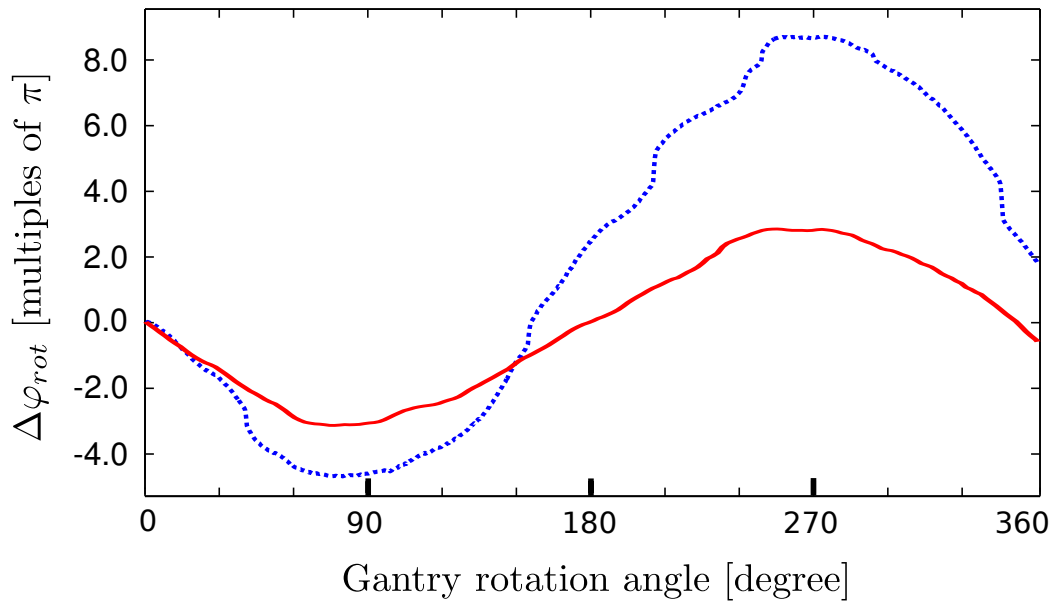


Figure 4.16: Rotational stability of the fringe phase value in differential phase-contrast images as a function of gantry rotation angle: previous phase grating mounting (dashed blue curve), and reworked mounting (solid red curve).

4.6.3 Reduction of silicon wafer thickness

An obvious approach to reduce acquisition time for a given X-ray source is to reduce the thickness of the silicon wafers on which the grating structures are grown. For the present wafer thickness of $550\ \mu\text{m}$, and the X-ray design energy of $23\ \text{keV}$, transmission through one wafer is approximately 70 %. For three wafers, this results in a loss of flux of approximately 66 %. Reducing the thickness of all three wafers to $100\ \mu\text{m}$ each, which is technologically feasible, would involve an increase of X-ray intensity by a factor of 2. As a consequence, the acquisition time would be reduced correspondingly.

Besides the reduced attenuation itself, also the energy spectrum would be affected—the effective energy would be reduced and the spectrum may be broadened slightly.

For the CT scanner, one grating wafer sample with $200\ \mu\text{m}$ thickness has already been manufactured. Handling and mounting in the scanner was carried out without any problems and a further reduction of wafer thickness to $100\ \mu\text{m}$ is ongoing.

4.6.4 Data acquisition and CT reconstruction

Further room for improvement lies in the way data is acquired and reconstructed.

- Currently, the gantry is operated in step-and-shoot mode meaning that phase stepping and gantry rotation are performed one after the other. Recently, Zanette et al. (2012) reported a data acquisition and processing method that combines sample rotation and phase stepping, which optimizes dose efficiency by a factor of 4, while maintaining image quality. An implementation of this optimized acquisition scheme is ongoing.
- Reference flat-field data is currently acquired at regular intervals during gantry rotation. As the sample needs to be moved out the FOV for that purpose, this procedure is quite time consuming. As an alternative, both parts may be separated, i.e. a ‘flat-field tomography’ scan could be performed before or after the ‘sample tomography’ scan. This approach would reduce scan time considerably, but a requirement is obviously that stability is sufficient and advanced software algorithms may be necessary to assign matching flat-field data for each gantry rotation angle.
- Moreover, due to the distinct beam divergence, it may be worth exploring spiral CT data acquisition, meaning that gantry rotation and bed movement are combined.
- On the side of reconstruction, the required number of projections and/or exposure time may be reduced with the use of advanced iterative reconstruction schemes.

4.6.5 Deterioration of source grating

In the compact gantry, the distance between the emission point of the X-ray source and the source grating G0 amounts to only 3 cm. Due to this proximity, damage of this grating was observed after approximately six months of usage. In particular after a CT scan investigating long-term stability, which was operated non-stop over several days with maximum tube power (50 kVp, 800 μ A), this damage became apparent. Fig. 4.17 shows unprocessed flat-field images of the rotating-gantry CT scanner with an intact (a) and damaged source grating (b). The practical consequences of the damage are vertically oriented stripes (highlighted), which translate into ring artifacts in CT scans. Up until now, it is not clear whether the observed damage is due to the thermal or radiation exposure of the grating. Most probably, the damage leads

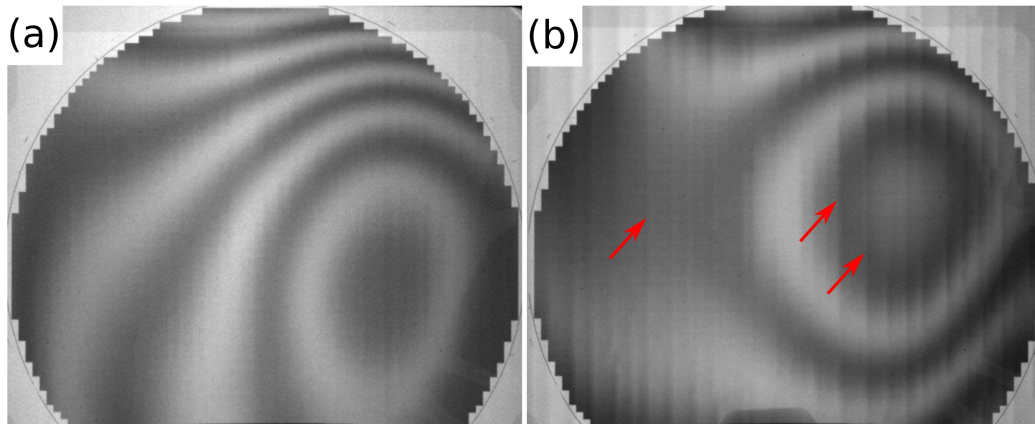


Figure 4.17: Deterioration of the source grating. Unprocessed flat-field image with an intact (a) and damaged (b) source grating. The results of the damage are vertically oriented stripes (highlighted) that translate into ring artifacts in CT scans.

to deformations of the photo-resist, which is neither temperature nor completely radiation hard.

In order to reduce the grating's exposure to low-energy X-rays, which naturally deposit most X-ray dose, currently a filter is designed, which is intended to be installed in front of the source grating. Please note that this filter has most probably no effect on X-ray dose and it is solely designed for practical reasons, i.e. to avoid damage of the source grating.

4.7 Summary and Outlook

In this chapter, the development of a first phase-contrast CT scanner was presented. First, a rotating-sample prototype was conceived and built. Based on a first commissioning experiment, the hardware was adapted with respect to the gratings and the imaging detector. In the next step, the redesigned gantry was implemented into a micro-CT housing. With this first rotating-gantry CT scanner, stability experiments and imaging of a fluid phantom and of biological tissue were conducted. It was found that, when adequate software correction algorithms are applied to correct for phase drifts, quantitatively accurate tomographic reconstruction of the linear attenuation coefficient μ and decrement of the refractive index δ can be performed. Moreover, increased soft-tissue contrast was observed visually and quantitatively with contrast-to-noise ratios in a fixated biological sample.

The intended use of the scanner is the repetitive in-vivo study of small-animal disease models. As illustrated in the last section, technological improvements have already been made and others are on their way to achieve this aim.

Already by now, projection-based in-vivo imaging is possible and has been performed. The main findings of a first in-vivo study and the results of a further study, which investigated lung emphysema in-vitro, are introduced briefly:

In-vivo radiography: A first radiography of a whole living mouse was recently conducted with the developed rotating-gantry CT scanner. This investigation demonstrated the feasibility of imaging a living mouse, with heart- and breathing movement: no artifacts, besides the common blur of strongly moving body parts, were seen and phase-stepping in particular does not induce additional aberrations. For further details, the reader is referred to the corresponding study by Bech et al. (2013).

Emphysema in mouse lungs: Towards mouse disease models, the diagnosis of lung emphysema was investigated in excised lungs. A first projection-based in-vitro study was performed with very promising results: with the combined information of attenuation and dark-field contrast, healthy and emphysematous lungs could be clearly distinguished. For further details, the reader is referred to the study by Yaroshenko et al. (2013).

In summary, it can be said that—with our efforts—phase-contrast imaging advanced considerably in the translation of the technique from bench to bedside. The feasibility of implementing a grating interferometer into a micro-CT scanner was demonstrated and, using this scanner, enhanced soft-tissue contrast was shown in biological tissues.

Chapter 5

Summary, conclusions and outlook

In this chapter, the main scientific results of this PhD thesis are summarized, corresponding conclusions are drawn, and a brief outlook is presented. Following the division of the thesis into two main parts, this chapter is structured accordingly.

Investigation of mouse disease models: Generally, this field can be divided into two distinct types of applications: high-performance benchmarking imaging on the one hand, and dose-compatible imaging on the other hand. With respect to the high-performance, synchrotron-radiation-based investigations, the following was found:

- The signal-to-noise ratio analysis of several organs in a healthy mouse specimen showed that soft-tissue contrast is approximately seven times larger in phase images than in attenuation images (at an X-ray energy of 35 keV). This renders the imaging technique, in general, attractive for a broad range of applications.
- In two pancreas tumor model mice, tissue heterogeneity was assessed. For a cystic lesion, it was found that the difference of fibrotic and cellular tissue composition was only visible in the phase image. Such a discrimination is, for example, of interest in the field of therapy response monitoring as differences in tissue composition result in regional differences of therapy response. In the other mouse specimen, heterogeneity of the solid tumor tissue was solely accessible on the basis of the phase image. Tumor heterogeneity is of great interest for a detailed characterization and staging of the tumor.

- For the colon carcinoma model mouse, it was observed that contrast in liver tissue was particularly increased (which was, however, not directly related to the tumor cells). This increased contrast in phase images allowed for the identification of a pathologic change of the aorta, i.e. an enormous accumulation of blood in the liver.
- In the same mouse specimen, a phase-contrast CT slice revealed—through the intact skull—different composites of gray and white matter of the cerebellum, even though image quality was strongly compromised by streak artifacts originating from the surrounding cranial bone.

With respect to potential in-vivo imaging, one pancreas tumor model mouse was imaged in a dose-compatible scenario using a conventional X-ray tube source. Here, the following striking observation was made:

- Detection of the solid tumor was solely feasible on the basis of the phase image and failed for the attenuation image.

From these observations, it can be concluded that phase-contrast CT is, indeed, a very powerful tool in small animal research. In the following, a few potential applications are discussed.

One particularly interesting potential application, for which increased soft-tissue contrast is indispensable, is the detection and characterization of soft-tissue tumors. Improved visibility of such tumor tissue would, most probably, be given for various organs as the SNR is generally significantly elevated in phase images. This superiority may prove helpful for both in-vivo and high-performance imaging.

Fibrosis in general is a disease that affects many organs (for example lung, liver, heart) and its detection is very challenging. Here, the combination of high-resolution and high soft-tissue contrast might be especially helpful.

With improved reconstruction schemes, for example iterative reconstruction algorithms that feature the option to weight the contribution of specific areas to the reconstruction, bone artifacts might be reduced. This may allow for high-resolution brain imaging, which is currently only feasible with reduced spatial resolution using MRI.

Development of a first phase-contrast small-animal CT scanner:

With this development, we have taken the major step from bench-top-based imaging setups with rotating sample, to a fully-functioning rotating-gantry CT scanner. In particular, the following aspects have been addressed successfully:

- A first small-animal phase-contrast CT scanner was built.
- When rotating the gantry, the greatest challenge arises from artifacts, which are induced by slight changes in grating alignment. Using the introduced adaptive differential phase recovery procedure, these artifacts can be corrected.
- With a phantom study it was moreover demonstrated that the correction routine performs quantitatively accurate.
- Using the developed scanner, improved soft-tissue contrast was demonstrated for biological tissue, i.e. porcine rind and mouse liver.

In view of future in-vivo imaging experiments, the following points that require further improvement, were identified:

- The total scan time for high-performance CT scans is long, up to 28 hours for the presented CT scans.
- Radiation dose for such CT scans is correspondingly elevated, on the order of several Gy for the shown data.
- The design energy of the interferometer was not chosen ideally: the effective energy is approximately 4 keV higher than the design energy ($E_{\delta} = 27$ keV vs. $E_{design} = 23$ keV).

These aspects can be improved by mainly adapting the interferometer design energy (redesign of gratings), reducing the silicon wafer thickness, and optimizing the way data is acquired and reconstructed.

With the availability of the small-animal phase-contrast CT scanner, numerous preclinical investigations can be undertaken, which might benefit from increased soft-tissue contrast. In particular longitudinal studies—investigating for example the progression of a disease with time or the response of a certain medication—would benefit greatly from the option to do in-vivo imaging. Currently, such in-vivo studies are limited to planar radiography or limited-angle CT. Once the described optimizations are implemented, both X-ray dose and acquisition time will be reduced greatly. This will then, most probably, allow for full tomographic imaging of mouse disease models in the near future.

Overall, we believe that the research, which was presented in this PhD thesis, represents a considerable advancement in the translation of grating-based phase-contrast imaging from bench to bedside.

Bibliography

- A. Ale, V. Ermolayev, E. Herzog, C. Cohrs, M. H. de Angelis, and V. Ntziachristos. FMT-XCT: in vivo animal studies with hybrid fluorescence molecular tomography-X-ray computed tomography. *Nat. Methods*, 9(6): 615–20, 2012.
- J. Als-Nielsen and D. McMorrow. *Elements of Modern X-Ray Physics*. John Wiley & Sons, 2nd edition, 2011.
- M. Bech. *X-ray imaging with a grating interferometer*. PhD thesis, University of Copenhagen, 2009.
- M. Bech, T. Jensen, R. Feidenhans'l, O. Bunk, C. David, and F. Pfeiffer. Soft-tissue phase-contrast tomography with an x-ray tube source. *Phys. Med. Biol.*, 54(9):2747, 2009.
- M. Bech, O. Bunk, T. Donath, R. Feidenhans'l, C. David, and F. Pfeiffer. Quantitative x-ray dark-field computed tomography. *Phys. Med. Biol.*, 55(18):5529, 2010.
- M. Bech, A. Tapfer, A. Velroyen, A. Yaroshenko, B. Pauwels, J. Hostens, P. Bruyndonckx, A. Sasov, and F. Pfeiffer. In-vivo phase-contrast x-ray imaging with compact scanner. *Submitted*, 2013.
- M. Born and E. Wolf. *Principles of optics*. Cambridge University Press, 1998.
- P. Callaghan. *Principles of Nuclear Magnetic Resonance Microscopy*. Clarendon Press, 1993.
- E. Castelli, M. Tonutti, F. Arfelli, R. Longo, E. Quaia, L. Rigon, D. Sanabor, F. Zanconati, D. Dreossi, A. Abrami, E. Quai, P. Bregant, K. Casarin, V. Chenda, R. H. Menk, T. Rokvic, A. Vascotto, G. Tromba, and M. A. Cova. Mammography with synchrotron radiation: first clinical experience with phase-detection technique. *Radiology*, 259(3):684–94, 2011.

- C. T. Chantler. Theoretical Form Factor, Attenuation, and Scattering Tabulation for $Z=1-92$ from $E=1-10$ eV to $E=0.4-1.0$ MeV. *J. Phys. Chem. Ref. Data*, 24(1):71, 1995.
- G. Chen, J. Zambelli, K. Li, N. Bevins, and Z. Qi. Scaling law for noise variance and spatial resolution in differential phase contrast computed tomography. *Med. Phys.*, 38(2):584–588, 2011.
- V. Cnudde, B. Masschaele, H. E. V. De Cock, K. Olstad, L. Vlaminck, J. Vlassenbroeck, M. Dierick, Y. D. Witte, L. Van Hoorebeke, and P. Jacobs. Virtual histology by means of high-resolution X-ray CT. *J. Microsc.*, 232(3):476–85, 2008.
- P. Coan, A. Peterzol, S. Fiedler, C. Ponchut, J. C. Labiche, and A. Bravin. Evaluation of imaging performance of a taper optics CCD ‘FReLoN’ camera designed for medical imaging. *J. Synchrotron Radiat.*, 13(3):260–70, 2006.
- C. David, B. Nöhammer, H. H. Solak, and E. Ziegler. Differential x-ray phase contrast imaging using a shearing interferometer. *Appl. Phys. Lett.*, 81(17):3287, 2002.
- T. Donath, M. Chabior, F. Pfeiffer, O. Bunk, E. Reznikova, J. Mohr, E. Hempel, S. Popescu, M. Hoheisel, M. Schuster, J. Baumann, and C. David. Inverse geometry for grating-based x-ray phase-contrast imaging. *J. Appl. Phys.*, 106(5):054703, 2009.
- T. Donath, F. Pfeiffer, O. Bunk, C. Grünzweig, E. Hempel, S. Popescu, P. Vock, and C. David. Toward clinical X-ray phase-contrast CT: demonstration of enhanced soft-tissue contrast in human specimen. *Invest. Radiol.*, 45(7):445–52, 2010.
- K. J. Engel, D. Geller, T. Köhler, G. Martens, S. Schusser, G. Vogtmeier, and E. Rössl. Contrast-to-noise in X-ray differential phase contrast imaging. *Nucl. Instrum. Meth. A*, 648, Supplement 1:S202–S207, 2011.
- M. Engelhardt, J. Baumann, M. Schuster, C. Kottler, F. Pfeiffer, O. Bunk, and C. David. High-resolution differential phase contrast imaging using a magnifying projection geometry with a microfocus x-ray source. *Appl. Phys. Lett.*, 90(22):224101, 2007.
- M. Engelhardt, C. Kottler, O. Bunk, C. David, C. Schroer, J. Baumann, M. Schuster, and F. Pfeiffer. The fractional Talbot effect in differential x-ray phase-contrast imaging for extended and polychromatic x-ray sources. *J. Microsc.*, 232(1):145–157, 2008.

- L. Feldkamp, L. Davis, and J. Kress. Practical conebeam algorithm. *J. Opt. Soc. Am. A.*, 1(6):612–619, 1984.
- S. D. Figueroa, C. T. Winkelmann, W. H. Miller, W. A. Volkert, and T. J. Hoffman. TLD assessment of mouse dosimetry during microCT imaging. *Med. Phys.*, 35(9):3866–3874, 2008.
- M. Germann, A. Morel, F. Beckmann, A. Andronache, D. Jeanmonod, and B. Müller. Strain fields in histological slices of brain tissue determined by synchrotron radiation-based micro computed tomography. *J. Neurosci. Methods*, 170(1):149–55, 2008.
- L. Grodzins. Optimum energies for x-ray transmission tomography of small samples: Applications of synchrotron radiation to computerized tomography I. *Nucl. Instrum. Methods Phys.*, 206(3):541–545, 1983a.
- L. Grodzins. Critical absorption tomography of small samples: Proposed applications of synchrotron radiation to computerized tomography II. *Nucl. Instrum. Methods Phys.*, 206(3):547–552, 1983b.
- J. Herzen, T. Donath, F. Pfeiffer, O. Bunk, C. Padeste, F. Beckmann, A. Schreyer, and C. David. Quantitative phase-contrast tomography of a liquid phantom using a conventional x-ray tube source. *Opt. Express*, 17(12):622–628, 2009.
- J. Herzen, T. Donath, F. Beckmann, M. Ogurreck, C. David, J. Mohr, F. Pfeiffer, and A. Schreyer. X-ray grating interferometer for materials-science imaging at a low-coherent wiggler source. *Rev. Sci. Instrum.*, 82(11):113711, 2011.
- E. Herzog, A. Taruttis, N. Beziere, A. A. Lutich, D. Razansky, and V. Ntzichristos. Optical imaging of cancer heterogeneity with multispectral optoacoustic tomography. *Radiology*, 263(2):461–8, 2012.
- S. R. Hingorani, E. F. Petricoin, A. Maitra, V. Rajapakse, C. King, M. A. Jacobetz, S. Ross, T. P. Conrads, T. D. Veenstra, B. A. Hitt, Y. Kawaguchi, D. Johann, L. A. Liotta, H. C. Crawford, M. E. Putt, T. Jacks, C. V. Wright, R. H. Hruban, A. M. Lowy, and D. A. Tuveson. Preinvasive and invasive ductal pancreatic cancer and its early detection in the mouse. *Cancer Cell*, 4(6):437–450, 2003.
- D. W. Holdsworth and M. M. Thornton. Micro-CT in small animal and specimen imaging. *Trends Biotechnol.*, 20(8):S34–S39, 2002.

- M. Hoshino, K. Uesugi, and N. Yagi. Phase-contrast X-ray microtomography of mouse fetus. *Biol. Open*, 1:269–74, 2012.
- R. James. *The Optical Principles of the Diffraction of X-rays*. Ox Bow Press, Woodbridge, 1962.
- A. Kak and M. Slaney. *Principles of Computerized Tomography*. IEEE Press, New York, 1987.
- J. Kenntner, T. Grund, B. Matthis, M. Boerner, J. Mohr, T. Scherer, M. Walter, M. Willner, A. Tapfer, M. Bech, F. Pfeiffer, I. Zanette, and T. Weitkamp. Front and Backside Structuring of Gratings for Phase Contrast Imaging With X-ray Tubes. *Proc. SPIE 7804*, 780408, 2010.
- J. Kenntner, V. Altapova, T. Grund, F. J. Pantenburg, J. Meiser, T. Baumbach, and J. Mohr. Fabrication and characterization of analyzer gratings with high aspect ratios for phase contrast imaging using a Talbot interferometer. *AIP Conf. Proc. 1437*, pages 89–93, 2012.
- T. Köhler, K. J. Engel, and E. Rössl. Noise properties of grating-based x-ray phase contrast computed tomography. *Med. Phys.*, 38(S1):S106–S116, 2011.
- A. C. Konstantinidis, M. B. Szafraniec, R. D. Speller, and A. Olivo. The Dexela 2923 CMOS X-ray detector: A flat panel detector based on CMOS active pixel sensors for medical imaging applications. *Nucl. Instrum. Meth. A*, 689:12–21, 2012.
- K. Li, N. Bevins, J. Zambelli, Z. Qi, and G.-H. Chen. Detection performance study for cone-beam differential phase contrast CT. *Proc. SPIE 8313*, 83131L, 2012.
- A. W. Lohmann, H. Knuppertz, and J. Jahns. Fractional Montgomery effect: a self-imaging phenomenon. *J. Opt. Soc. Am.*, 22(8):1500–1508, 2005.
- J. Mohr, T. Grund, D. Kunka, J. Kenntner, J. Leuthold, J. Meiser, J. Schulz, and M. Walter. High aspect ratio gratings for X-ray phase contrast imaging. *AIP Conf. Proc. 1466*, pages 41–50, 2012.
- A. Momose. Recent Advances in X-ray Phase Imaging. *Jpn. J. Appl. Phys.*, 44:6355–6367, 2005.
- A. Momose, S. Kawamoto, I. Koyama, Y. Hamaishi, K. Takai, and Y. Suzuki. Demonstration of X-Ray Talbot Interferometry. *Jpn. J. Appl. Phys.*, 42:L866–L868, 2003.

- A. Momose, W. Yashiro, Y. Takeda, Y. Suzuki, and T. Hattori. Phase Tomography by X-ray Talbot Interferometry for Biological Imaging. *Jpn. J. Appl. Phys.*, 45(6A):5254, 2006.
- W. Montgomery. Self-imaging objects of infinite aperture. *J. Opt. Soc. Am.*, 57:772–778, 1967.
- B. Müller, H. Deyhle, S. Lang, G. Schulz, T. Bormann, F. C. Fierz, and S. E. Hieber. Three-dimensional registration of tomography data for quantification in biomaterials science. *Int. J. of Mater. Res.*, 103(2):242–249, 2012.
- V. Ntziachristos. Going deeper than microscopy: the optical imaging frontier in biology. *Nat. Methods*, 7(8):603–14, 2010.
- D. Paganin. *Coherent X-Ray Optics*. Oxford University Press, 2006.
- F. Pfeiffer, T. Weitkamp, O. Bunk, and C. David. Phase retrieval and differential phase-contrast imaging with low-brilliance X-ray sources. *Nat. Phys.*, 2(4):258–261, 2006.
- F. Pfeiffer, O. Bunk, C. David, M. Bech, G. Le Duc, A. Bravin, and P. Cloetens. High-resolution brain tumor visualization using three-dimensional x-ray phase contrast tomography. *Phys. Med. Biol.*, 52(23):6923–30, 2007a.
- F. Pfeiffer, C. Kottler, O. Bunk, and C. David. Hard X-Ray Phase Tomography with Low-Brilliance Sources. *Phys. Rev. Lett.*, 98:108105, 2007b.
- F. Pfeiffer, M. Bech, O. Bunk, P. Kraft, E. Eikenberry, C. Brönnimann, C. Grünzweig, and C. David. Hard-X-ray dark-field imaging using a grating interferometer. *Nat. Mater.*, 7(2):134–7, 2008.
- W. H. Press, S. A. Teukolsky, W. T. Vetterling, and B. P. Flannery. *Numerical Recipes: The Art of Scientific Computing*. Cambridge University Press, 3rd edition, 2007.
- E. Reznikova, J. Mohr, M. Boerner, V. Nazmov, and P.-J. Jakobs. Soft X-ray lithography of high aspect ratio SU8 submicron structures. *Microsyst. Technol.*, 14:1683–1688, 2008.
- A. Sarantopoulos, G. Themelis, and V. Ntziachristos. Imaging the bio-distribution of fluorescent probes using multispectral epi-illumination cryoslicing imaging. *Mol. Imaging Biol.*, 13(5):874–85, 2011.

- S. Schleede, F. G. Meinel, M. Bech, J. Herzen, K. Achterhold, G. Potdevin, A. Malecki, S. Adam-Neumair, S. F. Thieme, F. Bamberg, K. Nikolaou, A. Bohla, A. Ö. Yildirim, R. Loewen, M. Gifford, R. Ruth, O. Eickelberg, M. Reiser, and F. Pfeiffer. Emphysema diagnosis using X-ray dark-field imaging at a laser-driven compact synchrotron light source. *PNAS*, 109(44):17880–5, 2012.
- G. Schulz, T. Weitkamp, I. Zanette, F. Pfeiffer, F. Beckmann, C. David, S. Rutishauser, E. Reznikova, and B. Müller. High-resolution tomographic imaging of a human cerebellum: comparison of absorption and grating-based phase contrast. *J. R. Soc. Interface*, 7(53):1665–76, 2010.
- G. Schulz, C. Waschkies, F. Pfeiffer, I. Zanette, T. Weitkamp, C. David, and B. Müller. Multimodal imaging of human cerebellum - merging X-ray phase microtomography, magnetic resonance microscopy and histology. *Sci. Rep.*, 2:826, 2012.
- J. T. Siveke, H. Einwächter, B. Sipos, C. Lubeseder-Martellato, G. Klöppel, and R. M. Schmid. Concomitant pancreatic activation of Kras(G12D) and Tgfa results in cystic papillary neoplasms reminiscent of human IPMN. *Cancer cell*, 12(3):266–79, 2007.
- M. Stampanoni, Z. Wang, T. Thüring, C. David, E. Roessl, M. Trippel, R. a. Kubik-Huch, G. Singer, M. K. Hohl, and N. Hauser. The First Analysis and Clinical Evaluation of Native Breast Tissue Using Differential Phase-Contrast Mammography. *Invest. Radiol.*, 46(12):801–806, 2011.
- G. J. Steyer, D. Roy, O. Salvado, M. E. Stone, and D. L. Wilson. Cryo-Imaging of Fluorescently-Labeled Single Cells in a Mouse. *Proc. SPIE* 7262, 72620W, 2009.
- D. Stutman, T. J. Beck, J. A. Carrino, and C. O. Bingham. Talbot phase-contrast x-ray imaging for the small joints of the hand. *Phys. Med. Biol.*, 56(17):5697–720, 2011.
- A. Sztrókay, J. Herzen, S. D. Auweter, S. Liebhardt, D. Mayr, M. Willner, D. Hahn, I. Zanette, T. Weitkamp, K. Hellerhoff, F. Pfeiffer, M. F. Reiser, and F. Bamberg. Assessment of grating-based X-ray phase-contrast CT for differentiation of invasive ductal carcinoma and ductal carcinoma in situ in an experimental ex vivo set-up. *Eur. Radiol.*, 23(2):381–7, 2012.
- H. Talbot. Facts related to optical science. *Phil. Mag.*, 9:401–407, 1836.

- A. Tapfer, M. Bech, B. Pauwels, X. Liu, P. Bruyndonckx, A. Sasov, J. Kenntner, J. Mohr, M. Walter, J. Schulz, and F. Pfeiffer. Development of a prototype gantry system for preclinical x-ray phase-contrast computed tomography. *Med. Phys.*, 38(11):5910–5, 2011.
- A. Tapfer, M. Bech, A. Velroyen, J. Meiser, J. Mohr, M. Walter, J. Schulz, B. Pauwels, P. Bruyndonckx, X. Liu, A. Sasov, and F. Pfeiffer. Experimental results from a preclinical X-ray phase-contrast CT scanner. *PNAS*, 109(39):15691–6, 2012.
- A. Tapfer, R. Braren, M. Bech, M. Willner, I. Zanette, T. Weitkamp, M. Trajkovic-Arsic, J. T. Siveke, M. Settles, M. Aichler, A. Walch, and F. Pfeiffer. X-Ray Phase-Contrast CT of a Pancreatic Ductal Adenocarcinoma Mouse Model. *PLoS One*, 8(3):e58439, 2013.
- A. Taruttis, M. Wildgruber, K. Kosanke, N. Beziere, K. Licha, R. Haag, M. Aichler, A. Walch, E. Rummeny, and V. Ntziachristos. Multispectral optoacoustic tomography of myocardial infarction. *Photoacoustics*, 1(1):e3–e8, 2013.
- T. Thuring, P. Modregger, T. Grund, J. Kenntner, C. David, and M. Stampanoni. High resolution, large field of view x-ray differential phase contrast imaging on a compact setup. *Appl. Phys. Lett.*, 99(4):041111, 2011.
- J. M. Tyszka, S. E. Fraser, and R. E. Jacobs. Magnetic resonance microscopy: recent advances and applications. *Curr. Opin. Biotechnol.*, 16(1):93–9, 2005.
- M. Wang, V. Bronte, P. W. Chen, L. Gritz, D. Panicali, S. A. Rosenberg, and N. P. Restifo. Active immunotherapy of cancer with a nonreplicating recombinant fowlpox virus encoding a model tumor-associated antigen. *J. Immunol.*, 154(9):4685–92, 1995.
- T. Weitkamp, A. Diaz, B. Nohammer, F. Pfeiffer, M. Stampanoni, E. Ziegler, and C. David. Moire interferometry formulas for hard x-ray wavefront sensing. *Proc. SPIE 5533*, pages 140–144, 2004.
- T. Weitkamp, A. Diaz, C. David, F. Pfeiffer, M. Stampanoni, P. Cloetens, and E. Ziegler. X-ray phase imaging with a grating interferometer. *Opt. Express*, 13(16):6296–6304, 2005.
- T. Weitkamp, C. David, C. Kottler, O. Bunk, and F. Pfeiffer. Tomography with grating interferometers at low-brilliance sources. *Proc. SPIE 6318*, 63180S, 2006.

- T. Weitkamp, C. David, O. Bunk, J. Bruder, P. Cloetens, and F. Pfeiffer. X-ray phase radiography and tomography of soft tissue using grating interferometry. *Eur. J. Radiol.*, 68:S13–7, 2008.
- T. Weitkamp, I. Zanette, C. David, J. Baruchel, M. Bech, P. Bernard, H. Deyhle, T. Donath, J. Kenntner, S. Lang, J. Mohr, B. Müller, F. Pfeiffer, E. Reznikova, S. Rutishauser, G. Schulz, A. Tapfer, and J.-P. Valade. Recent developments in x-ray Talbot interferometry at ESRF-ID19. *Proc. SPIE 7804*, 780406, 2010.
- W. J. Weninger, S. Meng, J. Streicher, and G. B. Müller. A new episcopic method for rapid 3-D reconstruction: applications in anatomy and embryology. *Anat. Embryol.*, 197(5):341–8, 1998.
- D. Wilson, D. Roy, G. Steyer, M. Gargsha, M. Stone, and E. McKinley. Whole Mouse Cryo-Imaging. *Proc. SPIE 6916*, 69161I, 2008.
- A. Yaroshenko, F. G. Meinel, M. Bech, A. Tapfer, A. Velroyen, S. Schleede, S. Auweter, A. Bohla, A. Ö. Yildirim, K. Nikolaou, F. Bamberg, O. Eickelberg, M. Reiser, and F. Pfeiffer. Pulmonary emphysema diagnosis using a preclinical small-animal x-ray dark-field scatter-contrast scanner. *Radiology*, in press, 2013.
- I. Zanette. *Interférométrie X à réseaux pour l'imagerie et l'analyse de front d'ondes au synchrotron*. PhD thesis, University of Grenoble, 2011.
- I. Zanette, M. Bech, A. Rack, G. Le Duc, P. Tafforeau, C. David, J. Mohr, F. Pfeiffer, and T. Weitkamp. Trimodal low-dose X-ray tomography. *PNAS*, 109(26):10199–204, 2012.

Publications and scientific presentations

Here, all publications and scientific presentations (oral and poster), which are related to the work of this thesis are listed in chronological order. The list of publications is categorized into first-authored and co-authored publications and subdivided into peer-reviewed publications and conference proceedings.

First-authored publications (peer-reviewed)

A. Tapfer, M. Bech, B. Pauwels, X. Liu, P. Bruyndonckx, A. Sasov, J. Kentner, J. Mohr, M. Walter, J. Schulz, and F. Pfeiffer. Development of a prototype gantry system for preclinical x-ray phase-contrast computed tomography. *Med. Phys.*, 38(11):5910–5, 2011.

A. Tapfer, M. Bech, A. Velroyen, J. Meiser, J. Mohr, M. Walter, J. Schulz, B. Pauwels, P. Bruyndonckx, X. Liu, A. Sasov, and F. Pfeiffer. Experimental results from a preclinical X-ray phase-contrast CT scanner. *PNAS*, 109(39):15691–6, 2012.

A. Tapfer, R. Braren, M. Bech, M. Willner, I. Zanette, T. Weitkamp, M. Trajkovic-Arsic, J. T. Siveke, M. Settles, M. Aichler, A. Walch, and F. Pfeiffer. X-Ray Phase-Contrast CT of a Pancreatic Ductal Adenocarcinoma Mouse Model. *PLoS One*, 8(3):e58439, 2013.

A. Tapfer, M. Bech, I. Zanette, P. Symvoulidis, S. Stangl, G. Multhoff, M. Molls, V. Ntziachristos, and F. Pfeiffer. 3D imaging of whole mouse models: comparing non-destructive X-ray phase-contrast microCT with cryotome-based planar epi-illumination imaging, submitted, 2013.

Co-authored publications (peer-reviewed)

J. Fu, P. Li, Q. L. Wang, S. Y. Wang, M. Bech, A. Tapfer, D. Hahn, and F. Pfeiffer. A reconstruction method for equidistant fan beam differential phase contrast computed tomography. *Phys. Med. Biol.*, 56(14):4529–38, 2011.

J. Fu, A. Velroyen, R. Tan, J. Zhang, L. Chen, A. Tapfer, M. Bech, and F. Pfeiffer. A reconstruction method for cone-beam differential x-ray phase-contrast computed tomography. *Opt. Express*, 20(19):21512–19, 2012.

M. Bech, A. Tapfer, A. Velroyen, A. Yaroshenko, B. Pauwels, J. Hostens, P. Bruyndonckx, A. Sasov, and F. Pfeiffer. In-vivo phase-contrast x-ray imaging with compact scanner, submitted, 2013.

T. Gaass, G. Potdevin, M. Bech, P. B. Noël, M. Willner, A. Tapfer, F. Pfeiffer, and A. Haase. Iterative reconstruction for few-view grating-based phase-contrast CT - An in vitro mouse model. *EPL*, in press, 2013.

A. Velroyen, M. Bech, A. Malecki, A. Tapfer, A. Yaroshenko, M. Ingrisch, C. C. Cyran, S. D. Auweter, K. Nikolaou, M. Reiser, and F. Pfeiffer. Microbubbles as a scattering contrast agent for grating-based x-ray dark-field imaging. *Phys. Med. Biol.*, 58(4):N37, 2013.

A. Yaroshenko, F. G. Meinel, M. Bech, A. Tapfer, A. Velroyen, S. Schleede, S. Auweter, A. Bohla, A. Ö. Yildirim, K. Nikolaou, F. Bamberg, O. Eickelberg, M. Reiser, and F. Pfeiffer. Pulmonary emphysema diagnosis using a preclinical small-animal x-ray dark-field scatter-contrast scanner. *Radiology*, in press, 2013.

Co-authored publications (conference proceedings)

J. Kenntner, T. Grund, B. Matthis, M. Boerner, J. Mohr, T. Scherer, M. Walter, M. Willner, A. Tapfer, M. Bech, F. Pfeiffer, I. Zanette, and T. Weitkamp. Front- and backside structuring of gratings for phase contrast imaging with x-ray tubes. *Proc. SPIE 7804*, 780408, 2010.

T. Weitkamp, I. Zanette, C. David, J. Baruchel, M. Bech, P. Bernard, H. Deyhle, T. Donath, J. Kenntner, S. Lang, J. Mohr, B. Müller, F. Pfeiffer, E. Reznikova, S. Rutishauser, G. Schulz, A. Tapfer, and J.-P. Valade. Recent developments in x-ray Talbot interferometry at ESRF-ID19. *Proc. SPIE 7804*, 780406, 2010.

T. Weitkamp, I. Zanette, G. Schulz, M. Bech, S. Rutishauser, S. Lang, T. Donath, A. Tapfer, H. Deyhle, P. Bernard, J.-P. Valade, E. Reznikova, J. Kenntner, J. Mohr, B. Müller, F. Pfeiffer, C. David, J. Baruchel, I. McNulty, C. Eyberger, and B. Lai. X-ray Grating Interferometry at ESRF: Applications and Recent Technical Developments. *AIP Conf. Proc.* 1365, pages 28–31, 2011.

M. Bech, A. Tapfer, A. Velroyen, A. Yaroshenko, B. Pauwels, P. Bruyndonckx, X. Liu, A. Sasov, J. Mohr, M. Walter, and F. Pfeiffer. Results from the first preclinical CT scanner with grating based phase contrast and a rotating gantry. *AIP Conf. Proc.* 1466, pages 130–136, 2012.

T. Gaass, G. Potdevin, M. Bech, J. Herzen, M. Willner, P. B. Noël, A. Tapfer, F. Pfeiffer, and A. Haase. Compressed sensing for phase-contrast computed tomography. *Proc. SPIE 8314*, 83144N, 2012.

T. Gaass, G. Potdevin, P. B. Noël, A. Tapfer, M. Willner, J. Herzen, M. Bech, F. Pfeiffer, and A. Haase. Compressed sensing for phase contrast CT. *AIP Conf. Proc.* 1466, pages 150–154, 2012.

B. Pauwels, P. Bruyndonckx, X. Liu, A. Tapfer, A. Velroyen, A. Yaroshenko, M. Bech, F. Pfeiffer, and A. Sasov. First small-animal in-vivo phase-contrast micro-CT scanner. *Proc. SPIE 8506*, 85060J, 2012.

A. Yaroshenko, F. G. Meinel, M. Bech, A. Tapfer, A. Velroyen, S. Schleede, S. Auweter, F. Bamberg, K. Nikolaou, A. Bohla, A. Ö. Yildirim, O. Eickelberg, M. Reiser, and F. Pfeiffer. Mapping the distribution of pulmonary emphysema using the results from a single projection obtained with the help of a preclinical small animal x-ray dark-field scatter-contrast scanner. *Proc. IEEE Int. Symp. Biom. Imag. (ISBI)*, pages 370–373, 2013.

Oral presentations

Title: Development of a compact gantry for quantitative phase-contrast CT applications, *Frühjahrstagung der Deutschen Physikalischen Gesellschaft*, Dresden, Germany, March 2011.

Title: First Results From a Preclinical X-Ray Phase-Contrast CT Scanner, *Annual Meeting of the American Association of Physicists in Medicine*

(AAPM), Vancouver, Canada, July 2011.

Title: Commissioning Results From a First Preclinical X-Ray Phase-Contrast CT Scanner, *SPIE Optics and Photonics*, San Diego, USA, August 2012.

Title: X-ray Phase-Contrast CT of a Pancreatic Ductal Adenocarcinoma Mouse Model, *International Symposium on BioMedical Applications of X-Ray Phase-Contrast Imaging (IMXP)*, Garmisch, Germany, January 2013.

Poster presentations

Title: Phase-Contrast micro-CT for Studying Small-Animal Tumor Models, *International Conference on X-ray Microscopy (XRM)*, Chicago, USA, August 2010.

Title: Grating-based Phase-Contrast Imaging for Studying Small-Animal Tumor Models, *ANKA User Meeting*, Karlsruhe, Germany, October 2010.

Title: First Results From a Preclinical X-Ray Phase-Contrast CT Scanner, *Annual Meeting of the American Association of Physicists in Medicine (AAPM)*, Vancouver, Canada, July 2011.

Title: Phase-contrast micro-CT for small animal models, *CIMST Summer School on Biomedical Imaging*, ETH Zurich, Switzerland, September 2011.

Title: Preliminary Results From a First Preclinical X-Ray Phase-Contrast micro-CT Scanner, *International Symposium on BioMedical Applications of X-Ray Phase-Contrast Imaging (IMXP)*, Garmisch, Germany, January 2012.

Title: Commissioning Results From a First Preclinical X-Ray Phase-Contrast CT Scanner, *International Workshop on X-ray and Neutron Phase Imaging with Gratings (XNPIG)*, Tokyo, Japan, March 2012.

Acknowledgments

First and foremost, I would like to thank my academic supervisors, Prof. Franz Pfeiffer and Martin Bech. Thank you Franz for giving me the opportunity to work on this very exciting project, for sharing your vast experience in the field of x-ray imaging, your helpful guidance, and for creating a very inspiring working atmosphere. Martin, thank you for your tireless and patient commitment, your encouragement and your very valuable advice in numerous discussions.

A major part of my work, the development of a phase-contrast CT scanner, was done in a very close collaboration with Bruker microCT (formerly Skyscan). Alexander Sasov, thank you for your strong commitment to build such a scanner, and for giving me the opportunity to be part of this very exciting development. Bart Pauwels, thank you for your extraordinary dedication to the project, and the throughout very pleasant collaboration. Peter Bruyndonckx and Xuan Liu, thank you for your permanent support and help throughout our joint project.

I acknowledge and thank the members of the examination committee of this thesis, Prof. Axel Haase as second referee and Prof. Martin Zacharias as chairman.

This thesis work has been performed within collaborations with the Radiotherapy and Radiology Department of the Klinikum rechts der Isar, the European Synchrotron Radiation Facility (ESRF), the Institute of Microstructure Technology (IMT) of the Karlsruhe Institute of Technology, the company microworks, and the Helmholtz Zentrum München.

My gratitude goes to Prof. Gabriele Multhoff (Radiotherapy Department) for mentoring me in the framework of the TUM Graduate School, and for providing many interesting samples. Rickmer Braren (Radiology Department), thank you for your commitment to study tumor mice using X-ray phase-contrast imaging, for sharing your diagnostic skills and for providing

very interesting samples.

Thank you Timm Weitkamp and Irene Zanette for your huge efforts in developing an excellent imaging setup, and your professional support that made the acquisition of outstanding imaging data at ESRF possible.

Many thanks to Jürgen Mohr, Johannes Kenntner, Jan Meiser, Danays Kunka, and Max Amberger from IMT, and to Joachim Schulz and Marco Walter from microworks for their endless efforts in process development resulting in superb gratings with huge area.

I thank the group of Prof. Axel Walch for performing elaborate and time-consuming histology on several of our samples and for sharing their expert knowledge on mouse models.

Many thanks to all my colleagues at TUM—without you, my PhD would have been less than half the fun and you certainly contributed to the success of my PhD project. Special thanks go to my direct and virtual office mates: Alexander Hipp, Astrid Velroyen, Björn Enders, Dieter Hahn, Julia Herzen, Marco Stockmar, Marian Willner, Michael Epple, and Simone Schleede: thanks for the good company, all the refreshing coffee breaks, the great discussions on X-rays and beyond, and for reading drafts of this thesis. Furthermore, I would like to thank Andre Yaroshenko, Klaus Achterhold, Nelly de Leiris, Pierre Thibault, Martin Dierolf, Michael Chabior, Andreas Malecki, Hans Märzc, Guillaume Potdevin, Mark Müller, and Dieter Renker.

Finally, I would like to thank my family, especially my sister, all my friends, and in particular Kerstin for always being there for me.